Mohamed Khider Biskra University

Faculty of Exact and Life Sciences

Department of Material Science

Sector: Physics

Option: Renewable energy physics

Thesis presented with a view to obtaining the diplomat of

DOCTORATE

Improvement of a Solar Cell Performance by Introducing Defects

(Amélioration des performances d'une cellule solaire en introduisant des défauts

Presented by:

Attafi Djemaa

In front of the board of examiners composed by:

Tibermacine Toufik	Professor, Biskra University	President
Meftah Amjad	Professor, Biskra University	Supervisor
Sengouga Nouredine	Professor, Biskra University	Co- Supervisor
Dehemi Lakhdar	Professor, Batna University	Examiner
Lakhdar Nacereddine	Professor, Batna University	Examiner

2021/2022

ACKNOWLEDGEMENT

Dedication

To my dear family

Abstract

In this work, we investigated the tunnel oxide passivated contact (TOPCon) solar cell based on n-type Si (p-n-n$^+$ structure), and p-type Si (n-p-p$^+$ structure), respectively. We started by the study of a p-n single junction device. Then, we investigated the p-n-n$^+$ configuration in which an n$^+$ polysilicon layer is added as back-surface field (BSF) layer. Thereafter, the tunnel oxide passivated contact (TOPCon) cell was studied. This latter includes a wide bandgap (nitride or oxide) passivation layer (PL) between the absorber and BSF layers. The carrier transport and tunneling process, in such structure, are mainly ensured by electrons. Under the AM1.5G solar spectrum at ambient temperature, we investigated the BSF and the tunneling layer's effects on the solar cell output parameters. An additional study by changing the tunnel dielectric materials from the conventional SiO_2 to Si_3N_4, Al_2O_3, TiO_2 and the prospective HfO_2 was realized. After that, we explored the effect of the SiO_2 PL deep level defect which includes: the energy level position, the defects density, the defective tunneling layer thickness and the capture cross-section. Then, a similar study was carried out on the p-type Si-based TOPCon solar cell, in which the carrier transport and tunneling process are mainly achieved by holes. The simulation was accomplished using the two-dimensional (2D) SILVACO- ATLAS module.

We demonstrated that the passivation layer is required to achieve excellent interface passivation. Moreover, it shows an optimum thickness, below this thickness the solar cell performance is enhanced by a tunneling effect, while above it; the performance is deteriorated by the fill factor reduction.

The well-defined and selected deep level defects with a high density enough in the SiO_2 passivation layer with the optimum thickness provides better efficiency for the Si-based solar cells. Indeed, the selected defects assist the majority carrier's transport through their energy levels that are echoing with the band edge state, and repulse the minority carrier, therefore reducing recombination. Furthermore, the direct tunneling current is found to be dominant for thinner passivation layers, while, for relatively thicker layers, the indirect tunneling current through traps becomes the most influential as the defect density increases.

ملخص

في هذا العمل ، قمنا بدراسة خلية شمسية ذات تماس تم تخميله بأكسيد النفق (TOPCon: tunnel oxide passivated contact) حيث المنطقة الفعالة فيها (القاعدة) هي في الحالة الأولى من سيليكون نوع n – (n-type Si) أي بنية $p-n-n^+$ ، و في الحالة الثانية القاعدة هي من سيليكون نوع p (p-type Si) أي بنية -n $p-p^+$ ، على التوالي. بدأنا اولا بدراسة جهاز أحادي الوصلة p-n. بعد ذلك ، درسنا الخلية ذات البنية $p-n-n^+$ و التي تمت فيها إضافة طبقة سيليكون متعدد البلورات مطعم بشدة + n (n^+polysilicon) كطبقة حقل السطح الخلفي (Back Surface Field BSF). بعد ذلك ، تمت دراسة الخلية ذات التماس المخمل بأكسيد النفق (TOPCon) . هذه الأخيرة تتضمن طبقة تخميل (passivation layer (PL)) ذات فاصل طاقي عريض (نيتريد أو أكسيد) بين الطبقة الماصة وطبقة BSF. في هذه البنية، عملية نقل حاملات الشحنة و آلية النفق مضمونتان بشكل أساسي بواسطة الالكترونات.

تحت شروط الطيف الشمسي المعياري AM1.5G و درجة الحرارة المحيطة، درسنا تأثيرات كل من طبقة BSF و طبقة النفق على وسائط الخروج للخلية الشمسية. تم تحقيق دراسة إضافية عن طريق تغيير المواد العازلة للنفق من SiO_2 الاصطلاحي إلى Si_3N_4 Al_2O_3 TiO_2 و HfO_2 المرتقب. بعد ذلك ، فحصنا تأثير عيوب المستويات العميقة في طبقة SiO_2 و الذي يشمل: موضع مستوى الطاقة ، كثافة العيوب، سمك طبقة النفق التي تحتوي على العيوب ، والمقطع العرضي للقنص. تم إجراء دراسة مماثلة على الخلية الشمسية TOPCon ذات قاعدة من سيليكون نوع p ، و التي فيها يتم تحقيق كل من نقل الحاملات و آلية النفق بشكل أساسي عن طريق النقوب. تم إجراء المحاكاة باستخدام الوحدة الرقمية SILVACO- ATLAS ثنائية الأبعاد (2D).

في هذه الدراسة ، أثبتنا أن طبقة التخميل مطلوبة لتحقيق تخميل ممتاز للسطح الخلفي للخلية. علاوة على ذلك ، فإن لطبقة التخميل سمك مثالي ؛ تحت هذا السمك يتم تحسين أداء الخلية الشمسية من خلال تأثير النفق ، بينما يتدهور الأداء فوق هذا السمك من خلال تخفيض معامل التعبئة.

يوفر كل من مستوى وكثافة العيوب العميقة و المُحددة جيدًا في طبقة التخميل SiO_2 ذات السمك الأمثل, مردود أفضل للخلايا الشمسية القائمة على Si. بالفعل ، تساعد العيوب المختارة في نقل الحاملات الأغلبية من خلال مستويات طاقتها التي يتردد صداها مع حالة حافة العصابة ، وتصد الحاملات الأقلية ، وبالتالي تقليل الالتحام. علاوة على ذلك ، وجدنا أن تيار النفق المباشر هو المسيطر في حالة طبقات التخميل الرقيقة ، بينما ، بالنسبة للطبقات الأكثر سمكًا نسبيًا ، يصبح تيار النفق غير المباشر عبر المصائد هو الأكثر تأثيرًا مع زيادة كثافة العيوب.

Table of Contents

List of Figures :

List of Tables:

1. <u>Chapter 1: Introduction</u>

1.1 Background

The relentless rise of the use of renewable and sustainable energy resources and the challenge of reducing environmental pollution from fossil-fuel energy systems mainly emanate from the steady increase in power needs. In the thick of the technologies aimed at producing electrical energy from \zero-carbon" energy sources, the photovoltaic technology represents a heavy pedestal. Such technology feets the basic process called the photovoltaic effect, which converts the sunlight into electricity [1].

Photovoltaics is among the meaningful technologies intended at producing electricity from renewable and sustainable energy sources. That is because the universal photovoltaic market requires more and more productive and cost-effective technologies. The photovoltaic research is directed by the requirement of investigating solar cell architectures in order to raise the conversion efficiency to ensure, at the same time, inexpensive manufacturing. As a matter of fact, always a trade-off between production costs and conversion efficiency exists and the considerable technical progress achieved so far, along with the scaling effects of mass production, have led to a reduction in the levelized cost of electricity from PV, resulting in the global growth of this market. Today PV solar panels are widely used to power satellites, and villages in third-world countries to produce power for buildings, and for utility-scale power generation. They are produced in quantities of several hundred megawatts (MW) per year [2].

The history of the solar cell began in the late of 19th century with the principles of photography. It was detected that silver chloride (and other silver halides) respond to the light. Around 1839, Becquerel, and others measured the first photovoltaic cells. The process was done by immersing Copper-oxide- or silver-halide- metal electrodes in an electrolyte solution creating a so-called "wet photo electrochemical" effect. To explain this effect, one can immerse two copper sheets vertically in a glass of water containing copper sulfate or magnesium sulfate, which are electrolytes. After a few days, an oxide will be formed, and the illumination of one sheet in the solution will produce a small voltage that can be measured using a sensitive voltage meter connected to each sheet with alligator clips [2]. Then the concept of solar cells was developed.

Silicon is, by far, the most typical semiconductor material employed in solar cells, depicting approximately 95% of the modules sold today [3]. In addition, it is the second most abundant

material on Earth (after oxygen) and the most common semiconductor used in computer chips. It remains the preferred material for photovoltaics because of its stable and high cell efficiencies, non-toxicity, the maturity of production infrastructure, and the deep and prevalent level of skill obtainable in connection to silicon devices. Silicon solar panels are often referred to as '1st generation' panels, as silicon solar cell technology attains to the ground already in the 1950s. Presently, over 90% of the current solar cell market is based on silicon [4]. Currently, solar cells discovered of silicon contribute a combination of high efficiency, low cost, and long lifetime. Modules are expected to last for 25 years or more, still producing more than 80% of their original power after this time [5].

Large numbers of different types of photovoltaic solar cells have been advanced over time, but these based on crystalline silicon (c-Si) have supplanted all the others, symbolizing more than 93 % of the market at the end of 2016 [6]. Inside this market, there is still a wide variety of technologies taking over different architectures. In recent years, there have been large enhancements in mass production of high-quality wafers, maintenance of high minority carrier lifetimes, surface passivation, minimization of optical losses, device characterization, and other areas. Most of these enhancements are applicable in mass production. The supreme limit of silicon solar cell efficiency is 29%, which is substantially higher than the best laboratory (25%) and large-area commercial (24%) cells. Solar cell efficiencies above 25% appear to be feasible in both a laboratory and commercial environment. Such type of cells has lower bulk recombination, because of the combination between a thin substrate and a high minority carrier lifetime. Excellent surface passivation, small-area electrical contacts coordinated with low contact recombination; free carrier absorption and contact resistance; excellent optical control through the use of texturing, antireflection coatings and rear surface reflectors; low edge recombination assisted by the use of thinner wafers, larger cells, edge passivation; and sufficient metal coverage to minimize resistive losses [7].

Crystalline silicon (c-Si) based technologies with heavily doped, directly metalized contacts dominate the global photovoltaic market [1]. Recombination of photo-generated electrons and holes at the contact regions is rising to constrain the power conversion efficiencies of these devices as other performance-limiting energy losses are overcome. To move forward, c-Si PV technologies must perform alternative contacting approaches. Passivating contacts, which incorporate thin films within the contact structure that simultaneously suppress recombination and promote charge-carrier selectivity, are a promising next step for the mainstream c-Si PV industry. Recombination of photo-generated carriers at the contact regions of solar cells is increasingly limiting the power

conversion efficiencies of these devices. To make progress, in c-Si PV technologies must suppress recombination and promote charge-carrier selectivity simultaneously. Passivating contacts, which incorporate thin films within the contact is a key step added in the manufacturing of photovoltaic cells to reduce their surface recombination and increasing the collection of photogenerated carriers [8].

Deep-level defects are commonly harmful to the efficiency of solar cells, but, in accordance with the principal scientist and a project leader of the silicon photovoltaics group at NREL, who found results ran counter to the traditional wisdom. NREL theoretical research group proposes that defects with properly engineered energy levels can ameliorate carrier collection out of the cell, or improve surface passivation of the absorber layer. Researchers at NREL demonstrated a Si-based solar cell, including a (SiO_2) passivation layer. Especially, they inserted specific defects among a thin tunneling silicon dioxide layer that forms part of "passivated contact" for carrier collection, and within the aluminum oxide (Al_2O_3) surface passivation layer next to the silicon (Si) cell wafer, to be beneficial. However, the key to that process is how to find the right defect?

The idea puts forward by Hu et al [9] is, to enhance carrier collection through the tunneling SiO_2 layer, the defects need to have energy levels outside the Si bandgap but on condition to be close to one of the band edges, in order to selectively collect one type of photocarrier and block the other. In contrast, for surface passivation of Si by Al_2O_3, without carrier collection, a beneficial defect is profound below the silicon valence band and has a permanent negative charge.

1.2 Challenges of the work

Defects play an important role in the performance of semiconductor devices. Although shallow-level defects are often used to introduce charge carriers into semiconductors by doping, deep level defects are often considered degrading in optoelectronic devices, such as solar cells, mainly because they can recombine charge carriers, thereby reducing the quantum efficiency of the device. Therefore, significant efforts have been made to minimize the number of unwanted deep level defects. We show by numerical simulation using SILVACO ATLAS software , contrary to popular belief, the addition of well-chosen deep level defects in the collector region of a solar cell, carriers can actually improve efficiency [9]. The key is to find the appropriate defects, which can facilitate the transport of the majority carriers and / or reduce the concentration of minority carriers in the carrier collection region. This idea is demonstrated using the most common photovoltaic device, the silicon solar cell.

1.3 Objectives

In this work, a silicon solar cell is investigated by numerical simulation, using commercial software; the necessary semiconductor drift-diffusion equations are solved and calculate the current-voltage characteristics. The solar cell performance is extracted from these characteristics. To improve the solar cell efficiency an insulator (wide bandgap semiconductor) will be added to the collecting region for two main reasons. One is to passivate the solar cell. Secondly, defects will be added to this region. In solving the basic semiconductor equation, necessary models for the conduction mechanism have to be taken into account especially tunneling. The effect on the conduction contribution of the defects from the insulator has to be taken into account through tunneling.

These results lead to the hypothesis that the presence of a selected type of defect is the main reason for improving the solar cell performance. This cannot be proved experimentally, so the simulation is the best solution in this.

1.4 Scheme of the thesis

This thesis is organized as follows:

Chapter 1: is an introduction about photovoltaic energy and the importance of using silicon in solar cells, then an overview is presented about the importance of passivation of solar cell and the challenge of adding defects in it to improve its performance. It contains also a background of the thesis and research objectives.

Chapter 2: is devoted to the description of the fundamental concepts of solar cells, and the main factors limiting their efficiency.

Chapter 3: presents the basic passivation concepts, the means of fabrication of passivation contacts, and main technologies of silicon solar cells dominating the actual market.

Chapter 4: provides information on defects in semiconductors, from structural and electrical point of view, where different types of defect classification are presented.

Chapter 5: gives an overview of tunneling models used in semiconductor device simulation, and describes the numerical software SILVACO TCAD used in this work.

Chapter 6: presents the main results of the study of the tunnel oxide passivated contact (TOPCon) solar cell based on n-type Si (p-n-n$^+$ structure), and p-type Si (n-p-p$^+$ structure), respectively. Starting from a p-n single junction device, an n$^+$ polysilicon layer is added as back-surface field

(BSF) layer to investigate the p-n-n$^+$ configuration. Then, the SiO_2 tunnel oxide layer is included to study the n-type TOPCon solar cell. In the last section, we studied the influence of deep level defects SiO_2 tunneling layer, on the performance of both n and p types of TOPCon solar cell.

2. *Chapter 2: Basics of solar cells*

2.1 Introduction

Semiconductors are the dominant materials for new electronic and optical devices, which play a basic role in current technologies including light emitting diodes, lasers, detectors, solar cells, optical amplifiers ...etc.

In this chapter, we introduce the field of photovoltaic solar cells. We first address the photovoltaic cell's working principle. Secondly, we give an overview on the operating principles of solar cells, and discuss their figures of merit. Thirdly, we examine the main factors limiting their efficiency; we address charge generation, recombination and optical losses.

2.2 Photovoltaic cells working principle

It is well known that any semiconductor absorbing light generates pair of electron-hole in excess compared to thermal equilibrium. However, there is no current nor potential difference that is generated simply by illuminating such a material, as there is no driving force allowing the extraction of power. Generated carriers therefore randomly diffuse and recombine through the semiconductor.

The notion of a solar cell is to generate charge carriers inside a semiconductor material under illumination and to use an induced driving force to separate electrons and holes assemble them at the two cell terminals, therefore generating power through a load. When a p and n-type semiconductors are brought into contact, the electrons diffuse from the n side to the p side and, the holes flow by diffusion from the p-type to the n-type side, similarly. This movement leaves uncompensated ionized donor (N_{D+}) in the n-type and acceptor ions (N_{A-}) in the p-type, which are fixed to the lattice atoms on both sides and are unable to move. The fixed charges create an electric field (or electrostatic potential difference) across the junction in an opposite direction to carriers diffusion. Figure 2.1 shows that the energy of the free carriers will decrease quickly (electrons tend to lose their energy and holes tend to gain energy, inversely) in the neighborhood of the p-n junction. This formed region called the "depletion" region or the "Space Charge Region" (SCR)

.Since it is depleted both of electrons and holes and remains only the ionized fixed atoms [10], [11]. The electric field is responsible for the movement of electrons from the p-type to n-type and inversely for holes, i.e. from n-type to p-type. This carrier flow process is called by "drift". When diffusion starts, the diffusion current is high and the drift current is low. As diffusion continues, the space charge region extends. This intensifies the electric field and hence the drift current. The process continues until equilibrium is reached between both currents. This is how the p-n junction is created [12].

For the Si material, the p-n junction is generally formed by taking a p-type (respectively n-type) wafer and by introducing (e.g. by diffusion or implantation), close to its surface, n-type (respectively p-type) dopants. This process is usually implemented at high temperature, with an additional annealing step for dopant atoms activation. The junction is often formed very close to the front surface from where the light enters the cell [10], [13]. Two regions are distinguishable; the emitter which represents the layer on the top usually very thin (~ 0.5 μm in case of Si) and the base region, called also bulk, where almost all photons are absorbed.
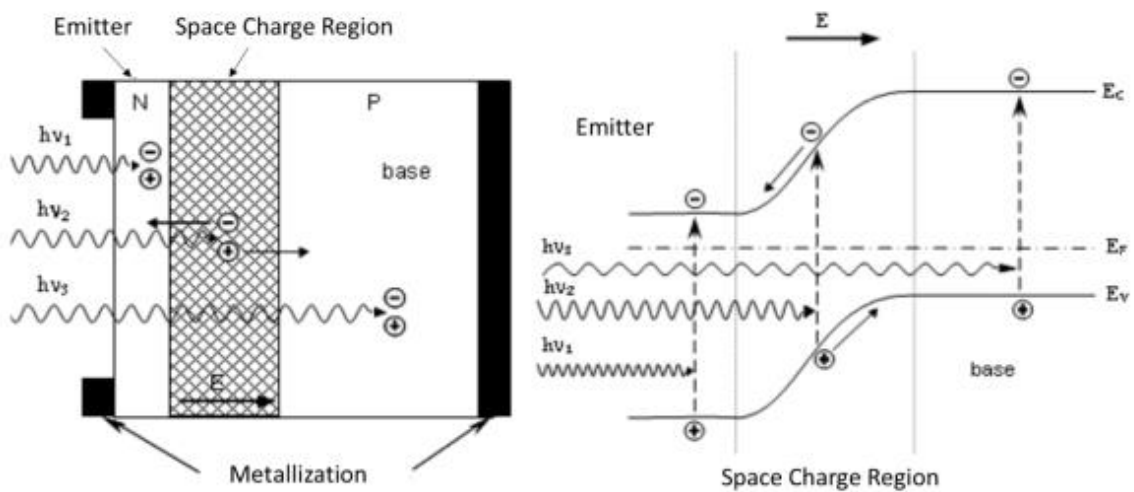
Figure 2.1 : Schematic representation (not at scale) left: structure of solar cell p-n junction, right: corresponding band diagram.

2.3 PV solar cells Basics

2.3.1   Current-voltage characteristics

The current/voltage curve $(I - V)$ (or current density/voltage curve $(J - V)$) is the main characteristic of a solar cell when a current normalizes over the surface area of the solar cell (Figure 2.2). The $J - V$ characteristic of the solar cell under dark conditions is very similar to that of a

diode. The current is very close to zero up to a "threshold voltage" where the current increases exponentially. A simple diode characteristic is modeled using the following equation:

$$J_D = J_0 \times \left(exp \left(\frac{qV}{nk_BT} \right) - 1 \right)$$

(2.1)

J_0 is the saturation current of the diode [mA/cm^2] and n is the ideality factor.

In contrast, under illumination, a photogeneration term is added to the previous equation, and the current is shifted downwards:

$$J = J_0 \times \left(exp \left(\frac{qV}{nk_BT} \right) - 1 \right) - J_L$$

(2.2)

Where, J_L is the photogenerated current [mA/cm^2].
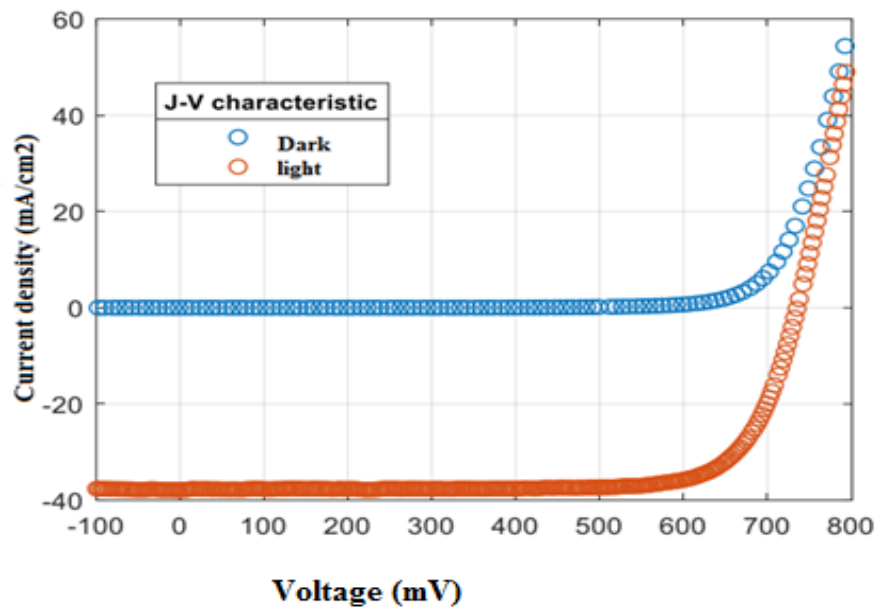
Figure 2.2 : $J - V$ characteristic of a solar cell in the dark and under illumination intensity.

2.3.2 Figures of merit

The $J - V$ curves of solar cells are usually represented upside-down, for better readability, with a positive current. Figure 2.3 represents a typical cells $J - V$ curve, as well as its power/voltage curve. This curve introduces various Figures of merit:

- The short-circuit current density,J_{SC}, represents the maximum current that the cell can generate, occurring when the cell's voltage is zero (load in short-circuit).

- The open-circuit voltage, V_{OC}, represents the maximum voltage that can be drawn, occurring when current is zero (load in open circuit).

- The maximum power point is where the power is maximum in the curve. We can define the power, current density and voltage at maximum power point, respectively P_{MPP}, J_{MPP} and V_{MPP}.

- The Fill Factor, FF, is the ratio defined such as:

$$FF = \frac{P_{MPP}}{V_{OC} \times J_{SC}} = \frac{V_{MPP} \times J_{MPP}}{V_{OC} \times J_{SC}} \qquad (2.3)$$

- A key Figure of merit for a solar cell is its power conversion efficiency, $\eta(\%)$, which is defined as the ratio of P_{max} (W) and the incident power, P_{in} that is related to the spectrum distribution and its intensity. The solar cell efficiency, η, can be defined as:

$$\eta = \frac{P_{MPP}}{P_{in}} = \frac{FF \times J_{SC} \times V_{OC}}{P_{in}} \qquad (2.3)$$

Where P_{in} is the incident irradiation power on the cell, and: $P_{in} = E \times S$. Where E is the irradiation power-density expressed in $[W/cm^2]$, and S $[cm^2]$ is the area of the cell.
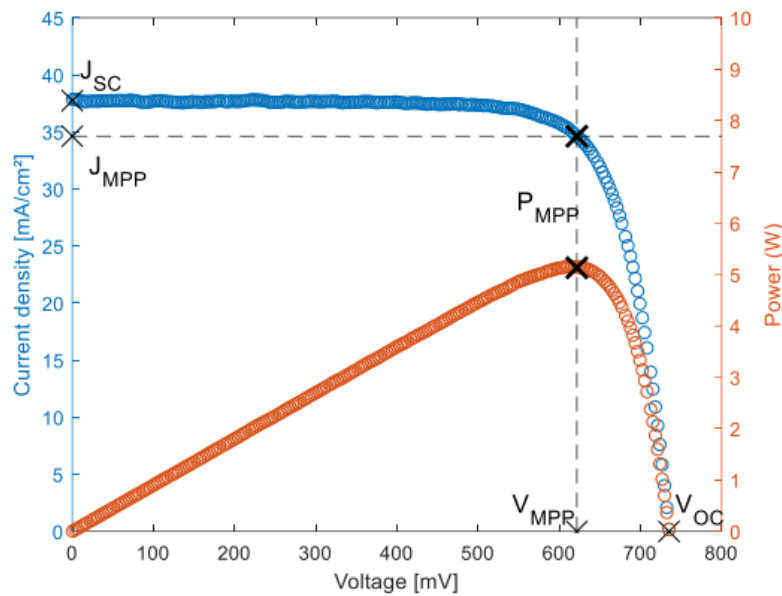
Figure 2.3 : Current density/voltage and power/voltage characteristics of a silicon solar cell under illumination.

2.3.3   Efficiency limiting factor

The main purpose of a solar cell is to absorb as many photons from the incident solar power as possible and then to collect the maximum amount of photo-generated electron-hole pairs at each of its terminals. The maximum theoretical efficiency for a single-junction solar cell based on a

semiconductor absorber material of bandgap energy E_g is mainly limited by photons of too low energy to be absorbed ($h\nu < E_g$) and thermalization of photons with too high energy ($h\nu > E_g$). Advanced notions are needed to tackle those limitations and the maximum theoretical efficiency has been estimated to be 29.43% for conventional silicon solar cells [14].

The efficiency of a solar cell is ruled by the electrical losses (recombination, shunt and series resistance), and optical losses (parasitic absorption or unabsorbed photons due to transmission or reflection).

• In short circuit conditions, the current is not affected by resistive effects nor recombination, for high to moderate cell efficiencies where $J_{SC} = J_L$. Then, only optical effects limit J_{SC}.

• While, at maximum power point, both effective lifetime and charge collection are of importance, so resistive effects will intervene. Series resistance, shunt resistance, and recombination losses affect FF here.

R_S and R_{SH} effects on the $I - V$ curve are illustrated in Figure 2.4. Series resistances (R_S) are the sum of the contribution from the various photovoltaic cell layers and interfaces: emitter, base, and metallization (especially metal-semiconductor interfaces) additionally to lateral resistances in each layer.

According to the first law of Joule; the power losses because of the R_S are more significant for high photogenerated current J_{Ph}, actually, the ohmic losses are proportional to the square of current. Conversely, the effect of R_{SH} is more pronounced at low photo-generated current. Point defects in p-n junction, presence of impurities during the diffusion metallization process, or solar cell edges imperfections can be the origin of the R_{SH}. Both resistances have a direct impact on the fill factor of the solar cell, hence on the output maximum power. In some cases, very large R_S (resp. low R_{SH}) can affect the short circuit current (resp. the open-circuit voltage) [15].
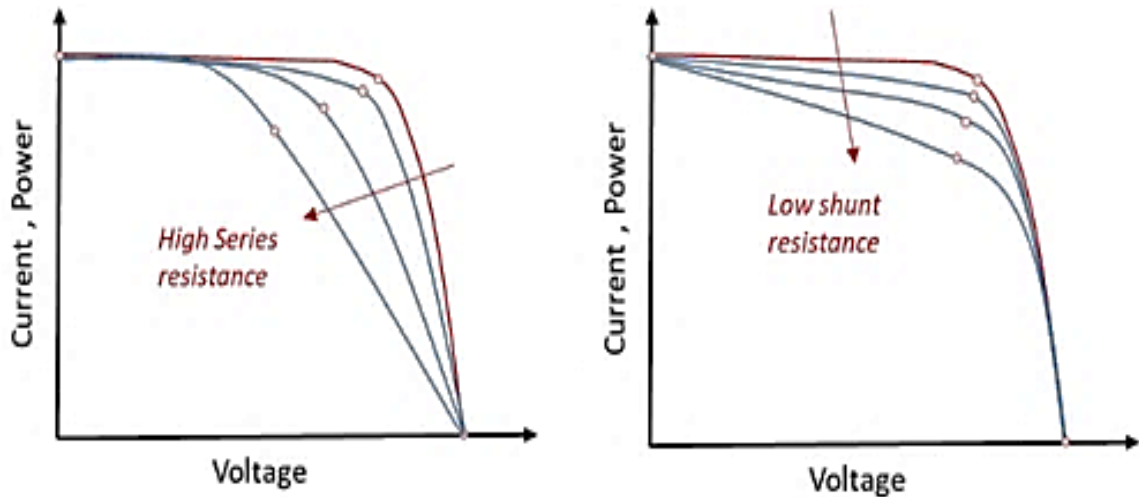
Figure 2.4 : Bottom-left: effect of series resistance on $I - V$ curve, bottom-right: effect of shunt resistance on $I - V$ curve.

2.4 Limits of single junction

From the equation of cell efficiency, it is clear that a high short circuit current J_{SC}, a high open-circuit voltage V_{OC}, and a fill factor FF as close as possible to one are needed for an efficient solar cell. The fundamental losses of the efficiency in a p-n junction are the transmission losses and hot carrier thermal losses. Therefore, the efficiency is actually limited by the material's bandgap. Materials with a wide bandgap can absorb only high-energy photons, generating low short-circuit current but a high carrier potential after thermalization. On the contrary, small bandgap materials will absorb more photons, generating a high short-circuit current, but low potential energy by charge carrier. These two losses are responsible for more than 40% of the efficiency losses for silicon single-junction solar cells. In the ideal case, radiative recombination losses are the only recombination losses in the material [16].

The maximum theoretical efficiency is known as the Shockley and Queisser (SQ) limit. It can be calculated using detailed balance theory, formulas, and theory is easily be found in the literature [12], [17]. In this theory, all photons that have energy higher than the bandgap ($E > E_g$) are assumed to be totally absorbed by the material, meaning that, the material is considered as optically thick enough to absorb all the photons as explained above in (Photon-semiconductor interactions). This limit corresponds to an ideal case where only radiative recombination of electron-hole pairs is counted. While, the non-radiative recombination is not considered: surface recombination depends mainly on the structure of the solar cell and surface conditions, while volume recombination depends mainly on the quality of the material (impurities, deep levels, dislocations). In this case, the lifetime (equivalent to diffusion length) of the minority carrier is the main

parameter and it is assumed to be infinite. Electrical losses (resistive) as well as optical (surface reflection) are also not considered and are primarily dependent on the technological manufacturing processes and architecture of the cell. For the AM1.5G solar spectrum, the theoretical maximum limit of SQ is ~33.7% for an ideal material of 1.34 eV bandgap as existed in Figure 2.5 [18].
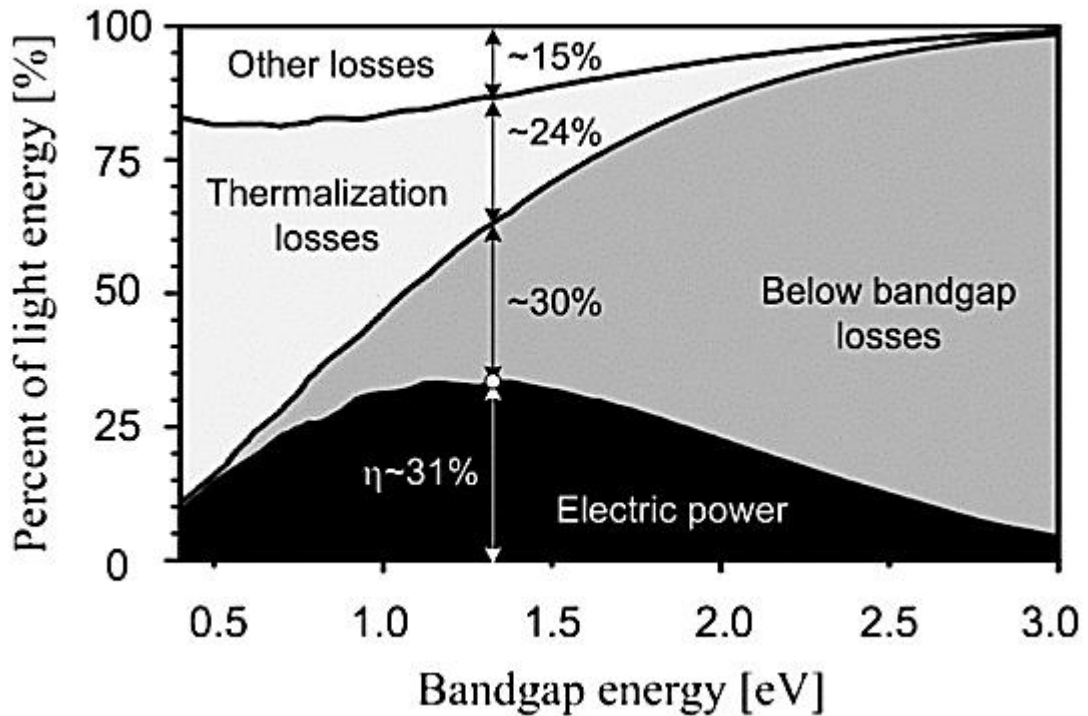
Figure 2.5: Ideal solar cell efficiency as a function of semiconductor bandgaps with the corresponding thermalization and optical losses taken from [17].

2.5 Charges generation and recombination mechanisms

The photovoltaic effect can be recapitulated as follows: when the light enters a p-n junction, the semiconductor material absorbs photons with energy above its bandgap. The majority of the absorption takes place in the bulk since the emitter thickness is the smallest compared to the bulk.

The photo-generated electron-hole pairs that diffuse long enough in the material to reach the junction will be separated by the electric field. Electrons in n-type become majority carries while holes minority carries, similarly, the p-type (holes become majority carries while electrons minority carries) after being separated by the electric field. The diffusing of electrons to the n-type, makes him negatively charged while the sweeping of holes to the p-type, makes him positively charged, creating a voltage. By connecting the front and rear contact with an external circuit, electrons (majority carrier) have a high probability to be collected by the metallization, so they flow by creating an electric current that provides power to the connected load. Finally, they

are returning to the solar cell through the other contact where they recombine with holes, returning to the valence band with the same energy as at the first.

The average distance traveled by electrons (in the p-type bulk region in the crystal before they recombine with holes in the valence band) is named minority carrier diffusion length, L (μm; it is expressed as a function of a lifetime, τ (μs), through diffusion coefficient, D ($cm^2.s^{-1}$), according to Eq.(2.4). It depends on the material purity, the doping level, and the intrinsic property of the material.

$$L = \sqrt{D \cdot \tau}$$ (2.4)

At thermal equilibrium the generation and recombination rates are equal ($G_0 = R_0$), resulting in a constant charge density of holes and electrons.

Once excited, an electron is in an unstable state, where it will quickly transfer back its energy through the emission of other particles. This happens through two channels:

1- Thermalization: multiple emissions of low-energy phonons. It is the fastest process, occurring in time scales of the order of 10^{-12} seconds [19].

2- Recombination: This can be a much slower process, occurring in time scales of the order of several milliseconds in high-quality crystalline silicon.

When the thermal equilibrium of a semiconductor is temporarily disturbed, the photo-generated excess carrier density (electrons and holes) tends to decrease toward their equilibrium values through recombination. The minority carrier lifetime (τ) is the usual metric chosen to quantify the recombination, instead of recombination rates assuming $\Delta n = \Delta p$ [20], it can be simplified to:

$$\tau = \frac{\Delta n_{av}}{G_{ph,av} - \frac{\partial \Delta n_{av}}{\partial t}}$$ (2.5)

Where Δn_{av} is the average minority carrier density in the bulk of the sample and $G_{ph,av}$ is the average photogeneration rate.

Two mechanisms lead to the charge carriers recombination in which, we can distinguish between the intrinsic and extrinsic recombination. Intrinsic recombination (subdivided into Radiative and Auger recombination) is related to inherent bulk material properties, meaning, it cannot be averted whatever the optimization, while extrinsic recombination is associated with the impact of defects. The effective lifetime of several recombination processes is the reciprocal sum of all given phenomena limited lifetimes:

$$\frac{1}{\tau} = \Sigma \frac{1}{\tau_i} \tag{2.6}$$

In principle, any extrinsic recombination is avoidable and can be tackled either by removing defects or by passivizing them. This is what we will discuss in detail later.

2.5.1 Radiative recombination

Radiative recombination, often called band-to-band recombination, is the direct recombination process of an electron-hole pair through photon emission. In indirect semiconductors like silicon, radiative recombination is mediated by phonons, making the process far less likely to happen. The electron conduction band transits to the valence band by emitting a photon of energy very close to Eg.

The radiative-limited lifetime (τ_{rad}) varies as a function of carrier density and can be expressed such as:

$$\tau_{rad} = \frac{1}{B(n_0 + p_0) + B\Delta n} \tag{2.7}$$

Where B is a constant dependant on the band structure of the material. For silicon $B = 4.73 \times 10^{-15} cm^3/s$ at room temperature [16], [21]. The radiative recombination mechanism is dominant in direct bandgap materials [10].

2.5.2 Auger recombination

The Auger recombination process cannot be measured directly in contrast to the radiative recombination. It is based on three-particle interaction (Figure 2.6): the energy from an electron-hole pair recombining is transferred to another free charge carrier through collision or through the Coulomb interaction of free charge carriers in said Coulomb-enhanced Auger recombination. The process either includes two electrons and a hole (eeh process) or two holes and an electron (ehh process). Since the process occurs with three particles interaction, it is most pronounced at high doping or high injection level. The net recombination rate for two electrons in non-equilibrium condition is expressed as Eq. (2.8):

$$U_{\text{Auger}} = B_{\text{Auger,p}} \left(n^2 p - n_0^2 p_0\right) \tag{2.8}$$
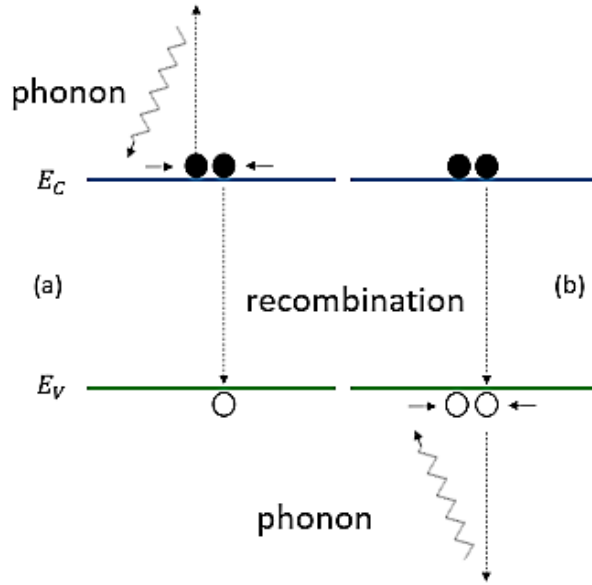
Figure 2.6 : (a) eeh and (b) ehh Auger processes.

$B_{\text{Auger,p}}$ values in the case of GaAs and Si are in the order of $10^{-30} cm^6 s^{-1}$ [22], [23],[24].

In direct bandgap where the radiative recombination is most dominant, Auger recombination is negligible. However, in indirect bandgap semiconductor such as Si or Ge, Auger is the dominant recombination process. Also, at highly injection levels (Δn or $\Delta p \gg N_{D,A}$), Auger recombination becomes crucial, and it is one of the major effects limiting the maximum theoretical efficiency of solar cells [25].

2.5.3 SRH recombination

Defects such as metallic impurities or crystallographic defects, introduced in a semi-conductor lattice, stimulate parasitic energy states in the band structure. These energy levels allow electrons and holes to transmit into them, and recombine or be generated in them. The formalism proposed by Shockley, Read and Hall [26]to describe this phenomenon is indicated as SRH recombination. In usual cases of no trapping ($\Delta n = \Delta p$) and single defect level, the SRH-limited lifetime is defined as:

$$\tau_{SRH} = \tau_{n_0} \times \left(\frac{p_0 + p_1 + \Delta n}{n_0 + p_0 + \Delta n}\right) + \tau_{p_0} \times \left(\frac{n_0 + n_1 + \Delta n}{n_0 + p_0 + \Delta n}\right) \tag{2.9}$$

$$n_1 = N_C \times exp\left(-\frac{E_C - E_t}{k_B T}\right), p_1 = N_V \times exp\left(-\frac{E_t - E_V}{k_B T}\right) \tag{2.10}$$

15

Where: n_1, p_1 are the SRH densities, with E_t the energy level of the defect in the bandgap of the material.

τ_{n_0}, τ_{p_0} are the capture time constants of electrons and holes such as:

$$\tau_{n_0} = (N_t \sigma_n v_{th})^{-1}, \tau_{p_0} = \left(N_t \sigma_p v_{th}\right)^{-1} \tag{2.11}$$

With: N_t the defect density at energy level E_t $[cm^{-3}]$, σ_n and σ_p the capture cross sections of electrons and holes of the defect $[cm^2]$, v_{th} the thermal velocity of the material – defined as the average velocity of minority carrier by Brownian motion – approximately equal to 10^7 cm/s for Silicon at 300K [27].

2.6 Surface recombination

In practice, most semiconductors have crystallographic defects, impurities or vacancies incorporated in their crystal structure during growth. It is plausible that these atomic impurities produce deep level defect states in the bandgap, which have the ability to capture a free carrier through non-radiative recombination. In the surface recombination process, an electron from the conduction band (E_c) recombine with a hole in the valence band (E_v) through a defect level "surface state" within the bandgap (E_g). The process is described mathematically by the Shockley-Read-Hall theory. The recombination rate U_{surf} via a single level surface state located at an energy (E_t) is given by the term [28]:

$$U_{surf} = \frac{(n_0 + \Delta n_S)(p_0 + \Delta p_S)}{\dfrac{p_0 + p_1 + \Delta n_S}{S_{n0}} + \dfrac{n_0 + n_1 + \Delta n_S}{S_{p0}}} \tag{2.12}$$

Where, Δn_S and Δp_S are the excess carrier electron and hole densities near the surface, n_1 and p_1 are the SRH densities of the surface defect, S_{n0} and S_{p0} are the surface recombination velocities of electron and holes defined such as:

$$S_{n0} = N_{t,surf} \sigma_n v_{th}, S_{p0} = N_{t,surf} \sigma_p v_{th} \tag{2.13}$$

Where, $N_{t,surf}$ [cm^{-2}] is the density of traps at the surface, σ_n and σ_p are the capture cross sections of electrons and holes $[cm^2]$ of this surface defect.

3. <u>*Chapter 3: Passivation of silicon solar cells*</u>

3.1 Introduction

The last issue that we touched on in the previous chapter is the problem of recombination mechanism and its damage on the semiconductor devices. The cure for that problem is the passivation. For that purpose, we will present in this chapter the passivation concepts, beginning from passivating contact concepts, how should be fabricated a passivating contacts, and the poly silicon passivating contact. We move after that to the mainstream silicon PV cells and review the main technologies of silicon solar cells dominating the market today.

3.2 Passivation concepts

3.2.1 Passivating Contacts

To increase the conversion efficiency of crystalline silicon solar cells, it is crucial to reduce the recombination losses between the photoactive part of the solar cell and the metal contacts. This is perfectly realized by fabricating contacts, which passivate the silicon surface defects while being simultaneously selective for only one type of charge carrier, i.e. either electrons or holes. Meaning that the conductivity (σ) should be high for one carrier type and low for the other type of carrier [29]. In other terms, the different contacts of a solar cell not only serve to collect the different types of charge carriers but should also act as a semipermeable membrane such that one contact transmits electrons and blocks holes, while the other contact do exactly the opposite [14]. Note that we specifically choose to refer to these contacts as passivating contacts and not passivated contacts, since it is intended that the contacts are passivating the Si surface and not the other way around.

The close metal-silicon contact in most silicon solar cells leads to recombination losses of the photo excited electrons and holes, because of the high density of electronically active states at the silicon-metal interface that lies in the silicon bandgap. To mitigate these deleterious effects, the so-called 'passivating contacts' are being developed in which the surface recombination can be suppressed by lowering the density of surface defect via chemical passivation, or by reducing

surface electron/hole concentration with an induced electric field, which is called the electric field passivation.

By growing ultrathin layers like SiO_2 or *a-Si:H* films, dangling bonds at c-Si surface will be saturated by forming *Si-O* or *Si-H* bonds. Typically, these layers are deposited by Chemical Vapor Deposition (CVD) process using precursor gases reacting with substrate and growing high-quality thin layers to passivate dangling bonds. Nitric acid or hydrofluoric acid also forms Si-O or Si-H bonds to terminate defects on the surface. When electron and hole concentrations are equal at the surface, recombination rate reaches its highest point; thus by reducing one of those values, U_{surf} (U_{surf} *chapter* 2 Eq. (2.12)) can be significantly inhibited. Such a performance is normally induced by creating a highly doped n$^+$/p$^+$ region via thermal diffusion, ion implantation, or CVD. p$^+$-p or n$^+$-n junction and various doped p-n junction show good field-effect passivation. Beyond this, by applying a dielectric layer with high charges also induce an internal electric field inside this insulator, preventing the accumulation of one specific carrier. This carrier selectivity is also one form of electric field passivation.

Although passivation materials can provide excellent passivation of the silicon surface that renders a low value of the saturation current density J_0, they do not exhibit a high conductivity σ for either electrons or holes(σ_e, σ_h). Due to misalignment of either the conduction band and the valence band of the two materials Al_2O_3 (and silicon); which is shown in Figure 3.1.(a).

Metals typically have a high density of states in the forbidden c-Si bandgap, it is inevitable for these states to start acting as very efficient recombination sites when brought into contact with silicon. The states in the metal line up with the silicon bandgap, which gives rise to a high J_0. At the same time, the work function matching of the silicon with the metal results in a high value of the conductivities (σ_e and σ_h), although there is no selectivity for one type of charge carrier (Figure 3.1.(b)).

Figure 3.1.(c) illustrates the need for a passivating contact, as shown in the given example, the conduction bands of the two materials are aligned while the valence bands are not aligned, meaning that this is an electron-selective contact. Note here that the selectivity for electrons is caused by a valence band offset which induces a reduction of the hole concentration at the interface of the two materials due to a larger distance between the quasi-Fermi level for holes and the valence band.
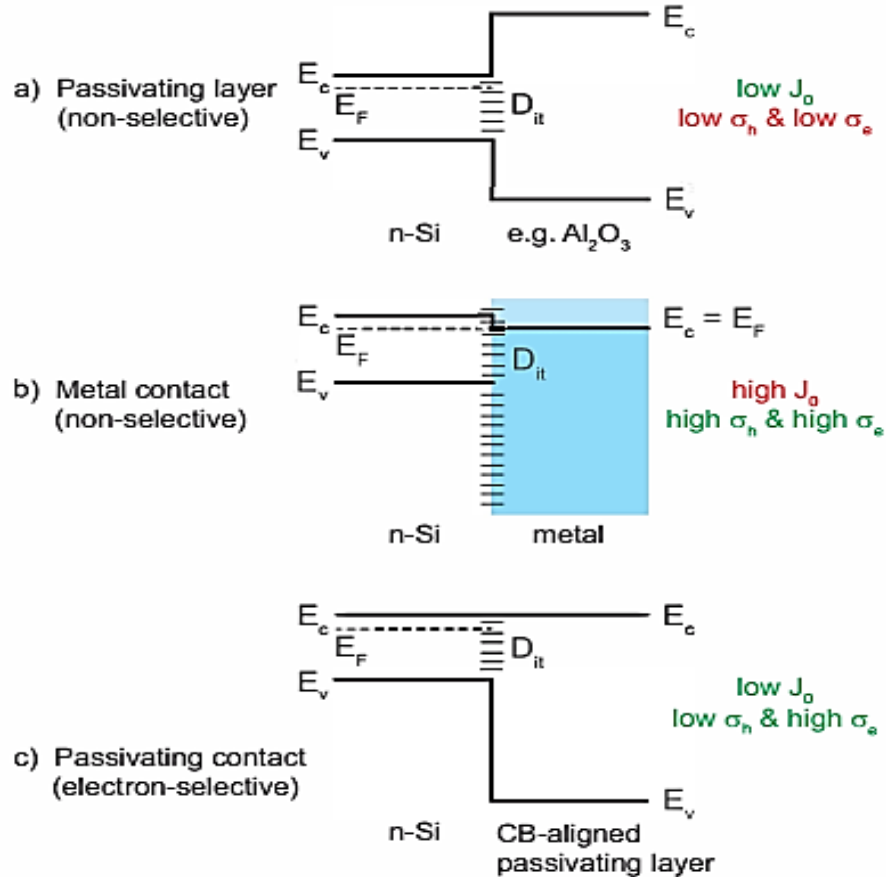
Figure 3.1 : Schematic idealized equilibrium band diagrams for (a) n-type silicon with a wide bandgap passivating layer like Al_2O_3, (b) n-Si with a metal contact (occupied/ unoccupied states indicated in dark/light blue), and (c) n-Si with a conduction band aligned passivating layer, i.e. an electron-selective passivating contact. The interface defect density at the silicon surface (D_{it}) is indicated together with the saturation current density J_0 , the electron and hole conductivities (σ_e and σ_h respectively).

3.2.2   Fundamental Concepts for Passivating Contacts

3.2.2.1   Passivating contact concepts

To passivate the defects existent at the silicon surface, the common application is to deposit or grow a dielectric material or other wide bandgap semiconductor material on top of the wafer. Prominent examples of such passivating layers include silicon oxide (SiO_2), hydrogenated amorphous silicon nitride (a-SiNx:H)], hydrogenated amorphous silicon (a-Si:H), aluminum oxide (Al_2O_3) [30], and, more recently TiO_2 and HfO_2 [31].

Even though these materials can supply excellent passivation of the silicon surface, thus making a low value of the saturation current density J_0, they do not show a high conductivity (σ) for either

electrons or holes. This is due to that neither the conduction band nor the valence band of the two materials is well aligned, as is shown in Figure 3.2.(a). As a result, a metal contact is usually fired locally through such a passivating layer to still make a functioning c-Si solar cell, even if the recombination at the metal interface is not specifically addressed in that case. This kind of recombination is explained in Figure 3.1.(b).
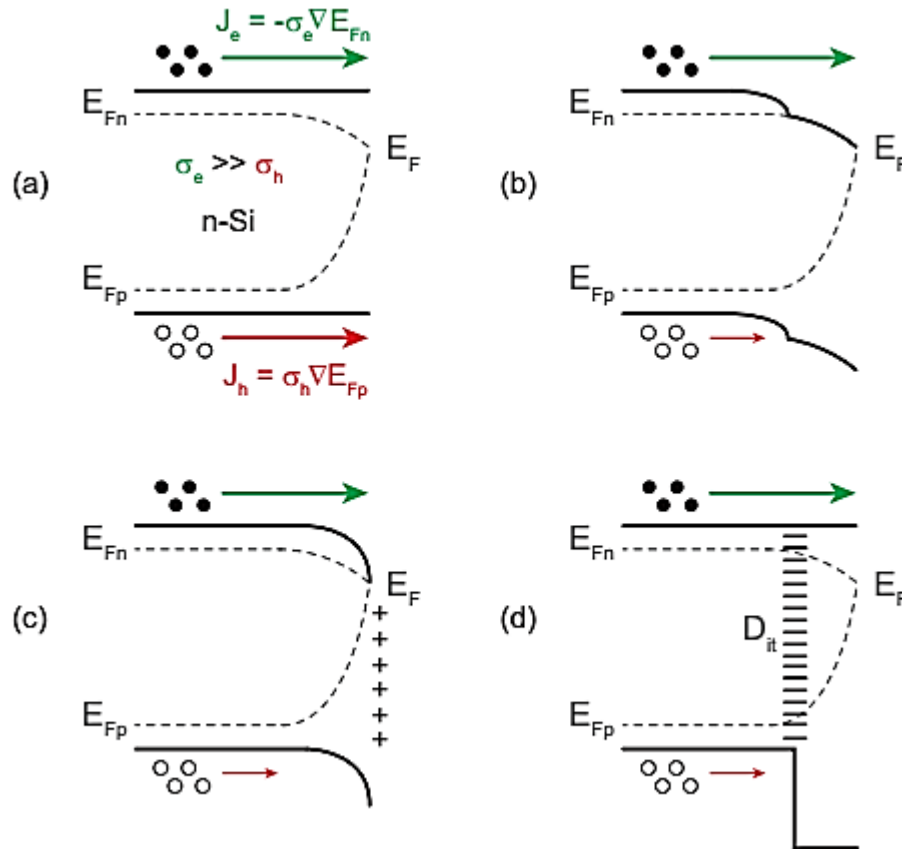
Figure 3.2 : Band diagram illustration for (a) n-Si wafer with a metal (not showed but positioned at right side of the n wafer) showing equal electron and hole currents in open circuit condition. (b) electron selective and passivation induced by an n$^+$ doped c-Si layer as metal/ bulk interface; (c) an external introduced band bending; (d) introduction of a band offset through a high bandgap material. The interface defect density at the Si surface (D_{it}) is indicated [32].

Since metals typically have an elevated density of states in the c-Si bandgap, it is necessary to start these states acting as very efficient recombination sites when brought into contact with silicon. The states in the metal line up with the silicon bandgap, which gives rise to a high J_0. At the same time, the work function matching of the silicon with the metal results in a high value of σ, although there is no selectivity for one type of charge carrier [32].

The prevalent way to make a metal contact selective for one type of carrier, is by inserting a thin, heavily doped layer between the Si base and the contact; which is traditionally called emitter or back surface field, such that σ is reduced for only one type of charge carrier. As heavy doping raises selectivity, it is a typical method to protect the metal contacts. In this approach, doping often requires thermal diffusion, which is an expensive processing step because of the high temperatures that are needed to drive in the dopants and activate them. This problem clarifies the necessity for a passivating contact, as shown in Figure 3.1 (c). In the presented example   (Figure 3.2), the conduction band of the two materials are aligned while the valence bands are not, this means an electron-selective contact. Noting here that the selectivity for electrons is caused by a valence band offset which is induced by a reduction of the hole concentration at the interface of the two materials due to a larger distance between the quasi Fermi level for holes and the valence band. It is necessary to remind that this is in contrast with the mentioned energy barrier in this context, which in some way would reflect away the holes from the interface. When the surface of Si is simultaneously passivated by the conduction-band aligned layer then we can define this as a passivating contact.

3.2.2.2   How should be fabricated a passivating contact?

To be able to answer this question, one considers first the existing solutions to make a selective contact. Figure 3.2, as an example, shows how an electron-selective contact can be made on n-type Si. As there can be no Fermi level splitting in the metal, the quasi-Fermi level that exists in the Si wafer coincide with the metal/Si interface [29].

In open circuit conditions, there are equal hole and electron current densities, even though the electron conductivity σ_e is much higher than the hole conductivityσ_h, as is shown in Figure3.2 (a). By placing the metal directly on the n-type Si, there are only a few amounts of selectivity for electrons due to the low base doping, however, this doping amount is not enough to avoid the high J_0 value. The introduction of a heavy n^+ doping in the silicon before the metal contact is brought into place, it is the most common path to make this contact selective for electrons as represented in Figure 3.2.(b). Even so, the introduced selectivity introduces an unwanted raised level of Auger recombination. A substitute approach to make the contact selective for electrons is the introduction of a band bending from an external source, i.e. through a high work function metal or a tunnel oxide with fixed charges. From both Figures3.2.(b) and 3.2.(c), it can be noted the reduction of hole current, but there is a limit to the amount of selectivity that can be achieved from band bending alone which is the purpose why solar cells based on Schottky junctions have the propensity to have

limited efficiencies. Another track to attain electron selectivity is by inserting a wide bandgap material between the n-Si and the metal with ensuring that the conduction band offset is as small as possible. Figure. 3.2(d) (or Figure. 3.1(c)) shows the ideal case of such a silicon heterojunction. When paying attention to the interface passivation as well, this approach has been shown to result in the most efficient c-Si solar cells reported so far [32].

3.2.3   Poly-Si Passivating Contacts

Polysilicon passivating contacts, consisting of a stack of tunnel-oxide and a doped polysilicon layers provide simultaneously excellent surface passivation and low contact resistivity for silicon solar cells [33]. The combination of the two materials provides both chemical passivation from dielectric oxide for its internal fixed charge and field-effect passivation induced by the highly doped poly-Si layer (Figure 3.3).
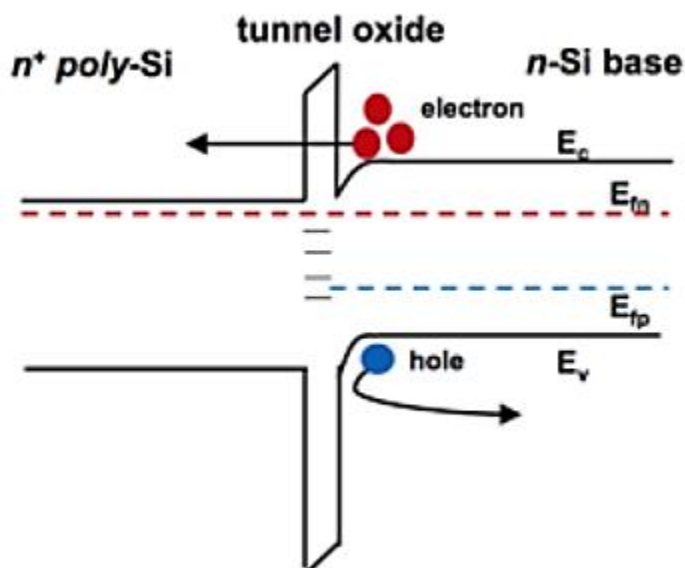
Figure 3.3 : Schematic band diagram of n$^+$ poly-Si passivating contact.

Nowadays, there is enormous interest within the crystalline silicon (c-Si) solar cell community in passivating contacts that are based on stacks of ultrathin SiO_2 and doped polycrystalline silicon. This technology of solar cells is called the tunnel oxide passivated contacts (TOPCon) [34] (Figure 3.4), also known by the abbreviations of POLO (Polycrystalline silicon (poly-Si) on Oxide) [35] and is considered as a very promising technology for the next generation of silicon solar cells. Applying the poly-Si/SiOx contact scheme on the cell's rear side, a power conversion efficiency of 25.7% [34]and 26.1% [35]on laboratory scale has been achieved. For that purpose, poly-Si passivating contacts are currently being introduced in large-scale mass production [36].
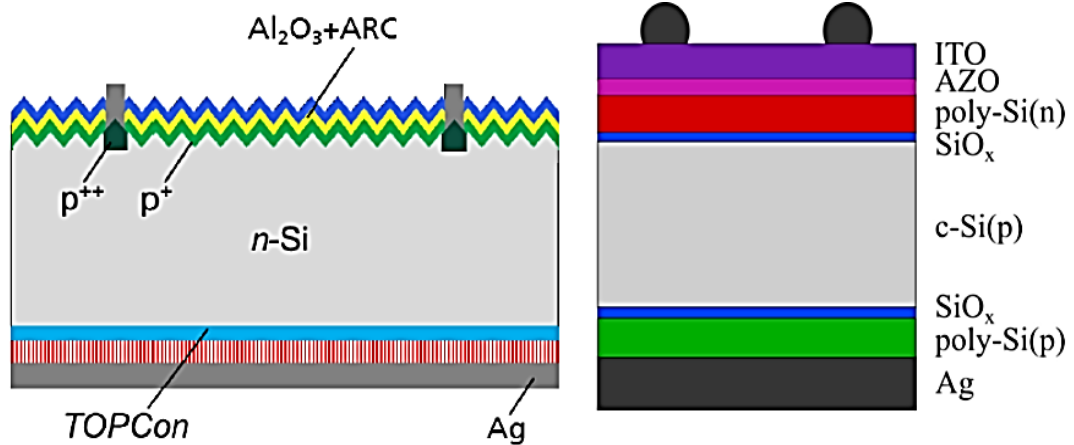
Figure 3.4 *:* TOPCon application in n-type silicon-based solar cell with boron diffused front and rear passivated contact (left), in p-type silicon-based solar cell with front/rear passivated contacts (right).

The prosperity of poly-Si passivating contacts can be comprehended from the extremely low contact resistivity ρ_c and the saturation current density J_0 values that can be achieved, which are together the two main Figures of merit for passivating contacts [37, 38]. Reported values of J_0 and ρ_c are well below $10\ fA/cm^2$ and $1\ m\Omega.cm^2$, respectively [34] [39].

Typically, poly-Si contacts are realized by a high-temperature anneal having plateau times of several tens of minutes, during which dopants can diffuse from the poly-Si through the oxide layer into the c-Si and thereby form a shallow doped region. On the other hand, poly-Si contacts can also be activated by a single firing step which typically lasts a few seconds [40]. Hereby, dopant diffusion is strongly suppressed and a hole-accumulation layer underneath the interfacial oxide is induced by the large work function of the highly doped poly-Si(p) layer [33].

For polysilicon-based passivating contacts, the passivating layer is a thin interfacial oxide ranging in thickness between 1 and 2 nm and the separation layer is a heavily doped polysilicon (poly-Si) layer. In order to minimize parasitic absorption due to the poly-Si layer[41], these layers are most commonly integrated on the rear side of solar cells. The efficiency of such cells is heavily dependent on a number of important aspects related to the passivating contact such as the thickness of the tunneling oxide layer [42], type and composition of tunneling oxide layer [43], doping level of poly-Si [44], annealing/diffusion temperature [45], and the parasitic absorption in the poly-Si layer [46] to name a few.

For this contact technology, hydrogen plays a substantial role in the saturation of electronically active defect states that would stimulate the charge carrier recombination near the interface of the Si absorber layer. In the case of the poly-Si passivating contact, usually, a high-temperature anneal at T in the range of $700 - 1050\ °C$ is used for crystallization and dopant activation. During this treatment, most of the hydrogen is flowing from the contact structure. Subsequently, to improve the chemical interface passivation, hydrogen must be incorporated again afterward [47]. Here, atomic hydrogen, being more effective for this intent as bound within an H_2 [48] molecule can be donated by hydrogen plasma, i.e., by remote plasma hydrogen passivation (RPHP) [49]. Substituted, it can be provided by H-rich dielectrics like SiN_x [34], [50] or AlO_x and SiO_x[51], [52]. Subsequent thermal treatment is required to enable the hydrogen diffusion to the critical poly-Si/SiO_x/c-Si interface, unless the process temperature present during the deposition of these films is already sufficient to attain this [47].

3.2.4   Carrier selective contacts

Another promising technique that has been used to diminish surface recombination in c-Si solar cells is the utilization of Carrier selective contacts (CSCs). Carrier selective contacts are not only to passivate the silicon surface, but also are carrier-selective in nature, i.e. they only allow either electrons or holes to pass through. The incorporation of CSCs into silicon solar cells improve cell efficiency by providing excellent surface passivation at contacted regions leading to a high open-circuit voltage V_{oc}, and a simplified current flow pattern leading to a high fill factor FF.

Usually, a CSC can be realized by the deposition of a conducting layer on an ultrathin passivation layer. As an example, the deposition of ultra-thin SiO_2 and doped hydrogenated amorphous silicon (a-Si:H) stack can act as an electron-selective or a hole-blocking layer. In spite of the higher efficiencies have been achieved for solar cells with CSCs based on a-Si:H and SiO_2, but they suffer from certain drawbacks that include thermal instability and parasitic photon absorption of a-Si:H films, complicated deposition process, and high fabrication cost. For that reason, it is required to develop high quality CSCs that can be deposited easily, economically, and safely with minimal serious risks.

Transition metal oxides have emerged as promising candidates for using as CSCs in c-Si solar cells. Typically, these CSC contain an ultra-thin layer of metal oxide, which has the role of electron-blocking or hole-blocking layer. For instance, sub-stoichiometric metal oxides i.e. tungsten oxide (WO_X), vanadium oxide(VO_X) and molybdenum oxide (M_OO_X) can act as electron-blocking layer to the n-type silicon absorber because of their wide band gap and high work function

resulting in a large conduction band offset(example of electron-blocking is illustrated in Figure 3.5) . As well, TiO_2 (Figure 3.6.b) can act as a hole-blocking layer due to the small conduction band offset (ΔEc ≈ 0.05 eV), which allows electrons to pass through the TiO_2 layer and the large valence-band offset (ΔEv ≈ 2.0 eV), which results in holes being blocked [53], [54].
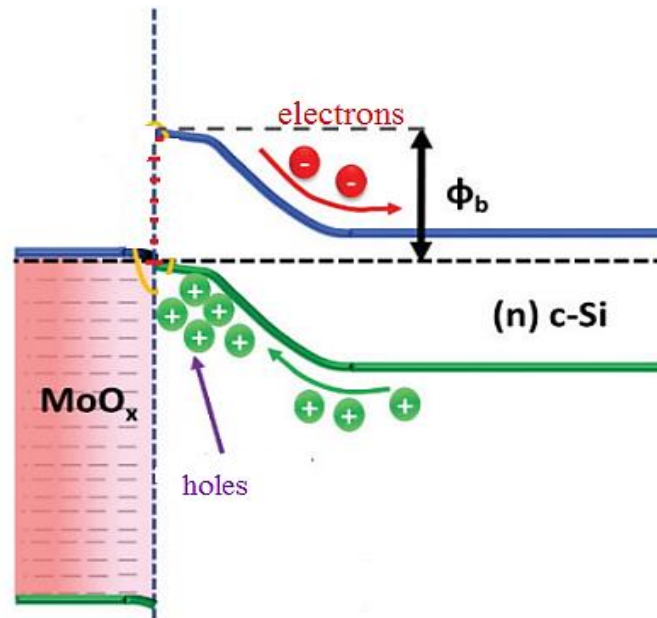
Figure 3.5: Energy band diagram of $M_O O_X$/n-Si heterojunction.
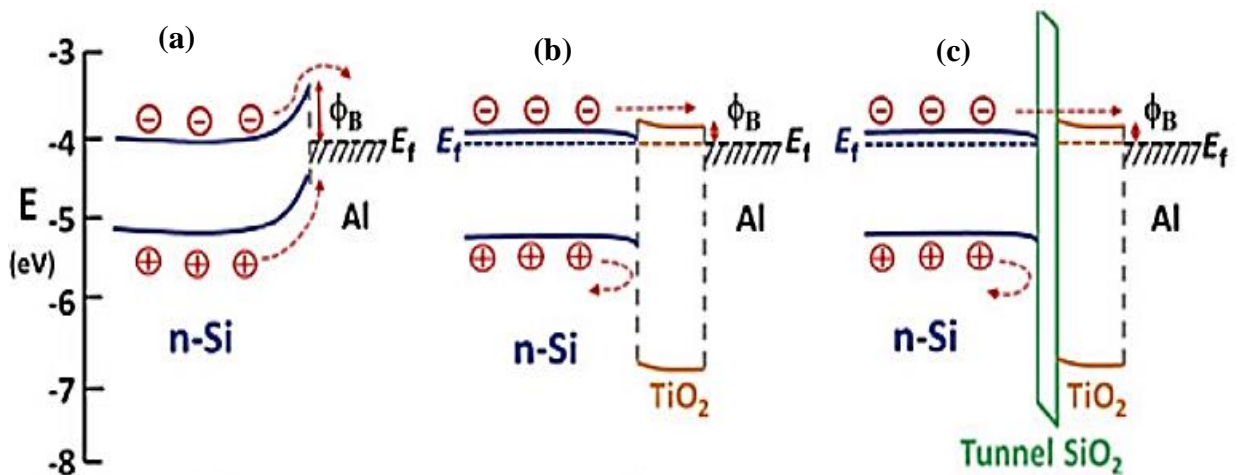
Figure 3.6: Bandgap alignments of the n-type silicon-based solar cells with different rear contacts: (a) n-Si/Al, (b) n-Si/TiO_2/Al, (c) n-Si/SiO_2/TiO_2/Al [53].

It is well known that a relatively large series resistance (ρ_c) is obtained for the n-Si/Al contact, which can be attributed to a relatively large Schottky barrier height between n-Si and Al. For that, the electrons have to pass through this large barrier before being collected by Al, as shown in Figure 3.6.(a).

The insertion of a thin interfacial dielectric layer between the semiconductor and metal can increase the carrier extraction for optoelectronic devices through the reduction of the Schottky barrier at the interface which might be caused by a reduced metal-induced gap states occupation in the semiconductor bandgap and hence Fermi level deepening.

Due to a very small conduction band offset ($\approx$0.05 eV) between Si and TiO_2 interlayer, the insertion of an ultrathin TiO_2 film (< 4.5 nm) between n-Si and Al reduces the Schottky barrier to 0–0.2 eV (Figure 3.6.(b)). By assuming a conduction band edge of TiO_2 at $\approx$0.4 eV and a work function of Al at 4.0–4.2 eV, hence the ρ_c values decrease to lower than 0.3 Ω cm^2. In the meanwhile, due to a large valence band offset ($> 2.0\ eV$) at the n-Si/TiO_2 interface, which would block the holes from silicon to TiO_2 layer, the carrier recombination at the interface is also suppressed. Although a tunnel SiO_2 insertion between n-Si and TiO_2 interface may not change the energy barrier height (Figure 3.6.(c)), ρ_c increases slightly due to the presence of tunnel resistance. The relatively large ρ_c at the n-Si/TiO_2 and n-Si/SiO_2/TiO_2 heterojunction might be attributed to the amorphous TiO_2 interlayer with a low conductivity [53].

3.3   Mainstream silicon PV cells

The huge majority of the solar cells produced up to 2020 are supported on silicon material [55]. Among all the silicon solar cells, two technologies form the mainstream with over than 95% combined market share as of 2018, the Aluminum-Back Surface Field (Al-BSF) and Passivated Emitter Rear Contact (PERC) cells [56].

The Al-BSF structure (see Figure 3.7) is the simplest one, based on a p-type absorber. The front surface consists of a highly n-type doped emitter, formed using phosphorous diffusion on the front side with an upper layer of anti-reflection coating, and fire-through metallization. The rear side features a full area of aluminum contact, which upon annealing at high temperatures, enables the formation of an Al-Si alloy which acts as a back surface field (BSF). It allows efficiencies of 19-20 % in production as of 2018 [56]. The most limiting factor of that structure is its back contact, which is the major source of losses due to recombination, despite the presence of BSF.
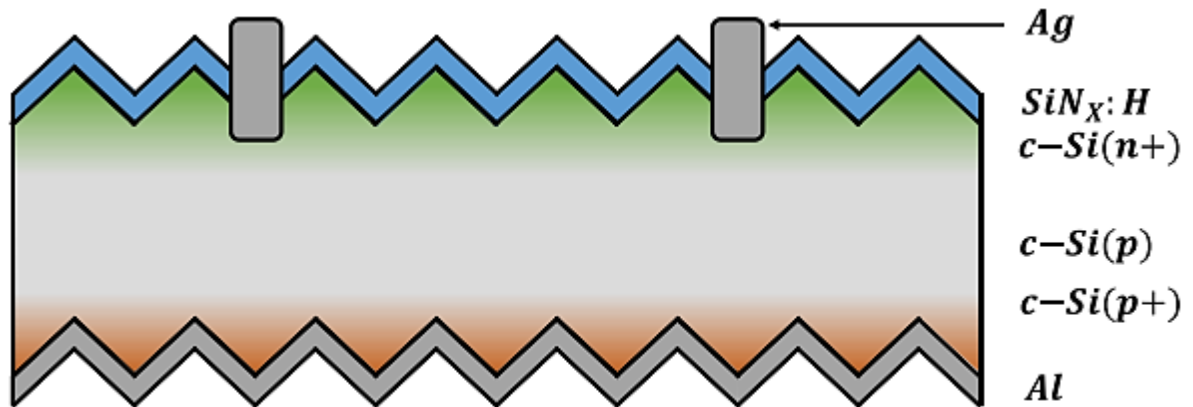
Figure 3.7: Schematic view of the Al-BSF structure.

The PERC structure (see Figure 3.8) proposed in 1989 is a development of the Al-BSF[57], which has an identical front side, but a more complex rear side. To decrease recombination at the rear side, a passivation layer is deposited on the c-Si at the rear contact, typically aluminum oxide (Al_2O_3), and hydrogenated silicon nitride (SiN$_x$:H). However, these stacks cannot be directly used as contacts as they are insulating materials, so the contact is made through the passivation oxides, and there is still a direct c-Si (p$^+$)/Al direct local contact. This structure enables higher efficiencies than the Al-BSF, at 20-22% in production lines [56].
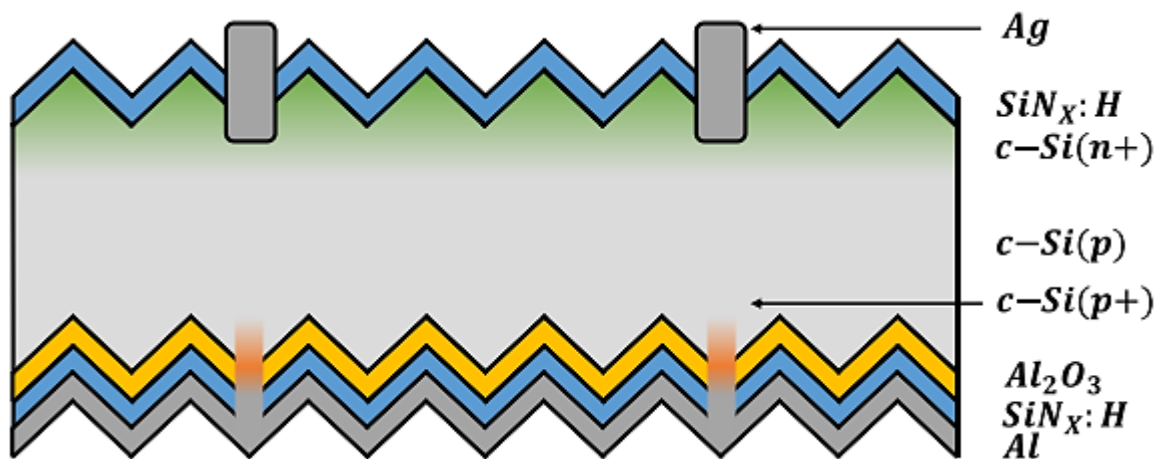
Figure 3.8: Schematic view of the PERC structure.

Prediction prophesies that the less efficient solar cells concept like the Al-BSF technology may soon disappear for the gain of PERC types and more developed efficient architectures (Figure 3.9).
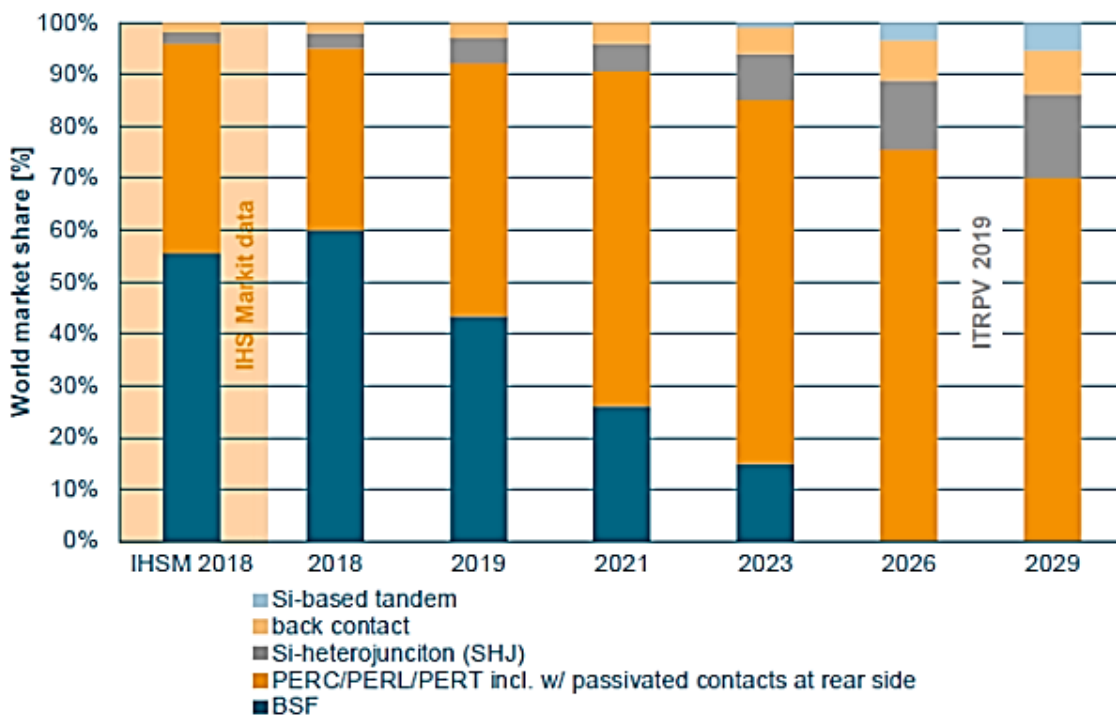
Figure 3.9: World market share of different silicon solar cell technologies, confirmed data and projected evolution until 2029 [58].

The manufacturing costs reduction [59], and monocrystalline wafer price drop [60] led to a decrease in the total cost of PV systems over the last decade (~-66% in 6 years [56]). This makes high-efficiency devices more and more cost-efficient. More details about these types and others will be considered later.

3.4 Advanced silicon solar cells state-of-the-art overview

The essential problem with the standard PV solar cells technology is their strongly recombinative metal contact [37], consequently, new approaches came to increase the single junction silicon cell efficiency; these approaches rely on so called "passivating contacts".

3.4.1 Types of crystalline silicon solar cells

Starting from the c-Si wafer as a base wafer, numerous solar cells designs have been studied, which use different passivating layers as well as have different geometrical structures. The most common cell designs will be shown later. Generally, one can classify solar cells into two categories: homojunction and heterojunction solar cells. This terminology has based on the types of materials used to create the p-n junction. In homojunction c-Si solar cells, the active material is only c-Si, while in heterojunction ones, it is c-Si along with a-Si:H, and specific metal oxides as transparent conductors or tunneling transport layers.

3.4.1.1   Al Back surface field (Al-BSF)

Back Surface Field (BSF) has been utilized for the first time as means to improve the solar cell performance by diminution the surface recombination velocity (SRV). From many methods to produce the BSF, the introduction of a highly doped layer on the wafer rear surface is the most popular method.

Depending on the dopant type in the wafer, the BSF layer could be either n^+ or p^+ type. This layer works as an internal electric field generator that will repel the photogenerated minority carrier near the rear surface, and therefore reduce the back surface recombination velocity (SRV). The aluminum layer effectiveness as a back surface field generator relies on the concentration of Al, this concentration is limited to its upper solid solubility in Si, which is about 10^{18} cm^{-3} at 750 C^o standard firing temperature [61]. The formation of Back Surface Field on the rear surface of the cell in the form of p^+ layer upon p-type wafer has shown the ability to increase cell's efficiency by 2.5% from its original value when p^+ layer thickness is around 2µm and the doping concentration is 10^{19} cm^{-3} [62]. Paul Procel et al. found that by forming 2µm n^+ BSF layer with a doping level around 4.16×10^{19} cm^{-3} upon n-type wafer the maximum efficiency that can be reached is around 19.98% [62].

Experimentally, Vichai Meemongkolkiat et al. provide an explanation of the process. They utilized the screen-printed Al–back-surface field BSF to passivate the Si back-surface solar cells due to its simplicity and cost effectiveness. That is done at the end of the solar cell process by screen printing the Al paste on the rear Si surface, followed by a high-temperature anneal to get an Al-doped p^+ Si layer. The Al-doped Si layer, referred to as "Al-BSF," introduces an electric field in the p-p^+ depletion region to repel minority carrier electrons and prevent them from recombining at the back-surface. It is well known that a thicker BSF and a higher p^+ doping level generally provide better passivation quality or lower back-surface recombination velocity (BSRV), which in turn leads to higher open circuit voltage V_{oc} and improved the solar cell performance [63]. Theoretically, thicker Al-BSF can be obtained by raising either the thickness of the Al printed or the peak alloying temperature, and the doping level can be increased primarily by raising the peak alloying temperature [63].

3.4.1.2   The passivated emitter rear contact (PERC) solar cell

The passivated emitter rear contact (PERC) solar cell was developed for the first time in the 1980s at the New South Wales University by Green et al [57]. Nevertheless, it has taken approximately

30 years to make it a commercial technology. In 2019, according to the international technology roadmap for photovoltaic (ITRPV), PERC solar cells overtook the place of the full-area aluminum back-surface field (Al-BSF) cell as the mainstream technology with a market share of over 60%. The Al-BSF lower efficiency is caused by some drawbacks i.e. higher rear surface recombination and weaker electric field at the rear surface. This forced to merge of the Field-effect passivation layer to mitigate those technical shortcomings.

Employment of a thin suitable dielectric layer [64], [65] at the rear surface is considered the key additions to standard Al-BSF solar cell leading to the fabrication of PERC solar cell. The use of an immobile charge rich dielectric thin layer at the rear side of the wafer acts as a field-effect layer and can also passivate the silicon surface leading to higher open-circuit voltage (V_{OC}). Many groups have been achieved high V_{OC} and enhanced solar performances thereof by carrying out studies on the application of suitable dielectric layers e.g. Al_2O_3 [66], [67], M_OO_X [68], $S_iN_X-S_iO_2$ and their bilayer combination [69].

The fast growth from the conventional Al-BSF cell structure to PERC solar cells has dramatically improved the efficiency of commercial-grade solar cells. Furthermore, the selection of a suitable dielectric layer with appropriate thickness depends upon the substrate type, and the additional coating by a suitable capping layer with optimized thickness is considered crucial to the PERC solar cell structures fabrication. Further structural modification has been incorporated by polishing the rear side of the wafer to reduce defects.

Ran Chen et al. proved that the efficiency of p-type monocrystalline Si PERC solar cells has been continuously increasing by a rate of $\sim$0.5% abs per year and has already reached 22.5%–23.83% in mass production environments[70]. Such a rapid increase in efficiencies is attributed to many improvements in the device aspect. Starting with bulk materials, thinner and high-quality of silicon wafers with low impurity concentrations and crystallographic defects have considerably suppressed bulk recombination losses, providing a prerequisite for fabricating a high-efficiency solar cell.

The introduction of a selective emitter (SE) structure can effectively decouple the requirements of forming high-quality ohmic contacts from the design of diffused emitters in passivated regions [71]. Afterwards, much more lightly doped emitters and screen-printing pastes designed to form effective contacts with such emitters, can be now used in PERC solar cells, leading to improvements in front surface passivation and spectral response without compromising contact resistance, and many other technical improvements, resulting in a significant increase in PERC

solar cells efficiencies. Efficiencies of ~24% have been declared for such a cell, and these have an efficiency potential of ~24% on an industrial scale as well [72],[71].
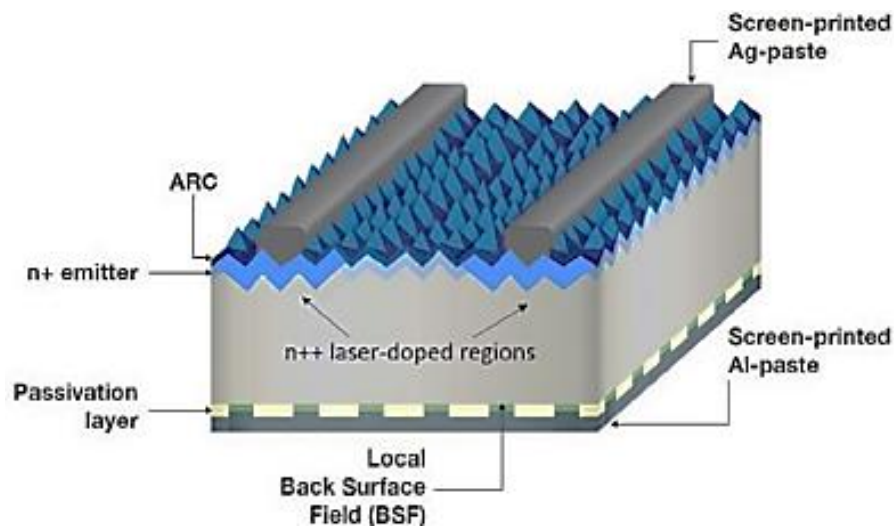
Figure 3.10: Schematic diagram of a screen-printed PERC solar cell.

3.4.1.3   Heterojunction solar cells

Another promising way to reduce recombination losses at the contacts is the adoption of carrier-selective contacts. The most attractive solar cell featuring carrier-selective contacts is the Silicon Heterojunction solar cell (SHJ) [73]. Herein, a stack composed of a metal/doped amorphous-silicon (a-Si)/intrinsic amorphous-silicon (i:a-Si)/c-Si substrate, guarantees the selectivity of carriers and permits only the majority carriers to reach the metal electrode while the minority carriers are rejected by the energy barrier. This drives to an absence of minority carriers at the contacts, so, no recombination can happen.

As stated by De Wolf et al.[74], the first hydrogenated a-Si/c-Si heterostructures were studied in 1974 by Fuhs and coworkers [75]. They attempted to combine the c-Si with a-Si:H technology to produce HJ solar cells. In spite of, they could not earn sufficient cell efficiencies. The solar cell and its band structure are shown in Figure 3.11.

Achievement of high-efficiency SHJ solar cell requires a high V_{OC}, which relies on excellent surface passivation of the c-Si. That process is dominated, at most, by the hydrogenation of silicon dangling bonds and the reduction of interfacial defect density with intrinsic amorphous silicon (i-a-Si:H) layers [76, 77].
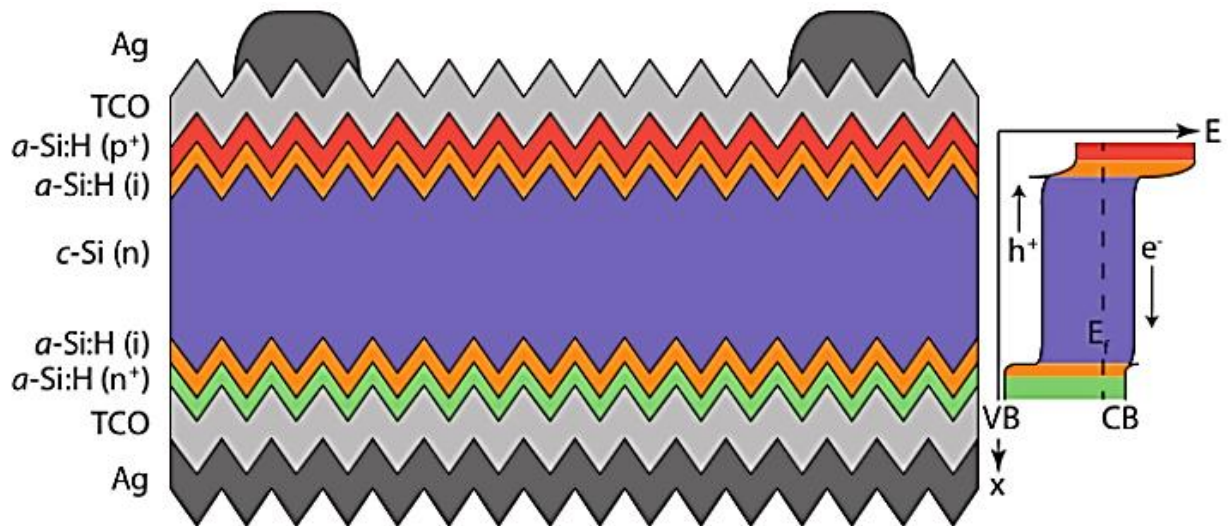
Figure 3.11*: Sketch of diffused-junction solar cell as first developed by Sanyo, Japan, including its band diagram. The wafer is n-type. Structure is not drawn to scale [74].

It has been widely recognized by the PV community that n-type silicon heterojunction (SHJ) solar cells have a promising route towards the next generation passivating contact technologies. The typical SHJ solar cell consists of an undiffused and n-type monocrystalline silicon (c-Si) wafer that, on both sides, is passivated by full area intrinsic/doped amorphous silicon (a-Si:H) film stacks, transparent conductive oxide (TCO) electrode, and silver grid fingers [78] (Figure 3.12). Outstanding surface passivation and elimination of metal/c-Si contact enable a high V_{OC} [79, 80]. Also, the series resistance (R_s) of SHJ solar cell is commonly considered as a gating factor for achieving higher efficiencies due to transporting through the resistive intrinsic amorphous silicon [a-Si:H(i)] films, thermionic/field emission over the valence band potential barrier at the c-Si/a-Si:H (i) -contact interface[81], and the Schottky barriers at quasi-metal-semiconductor a-Si:H/TCO interfaces [81].
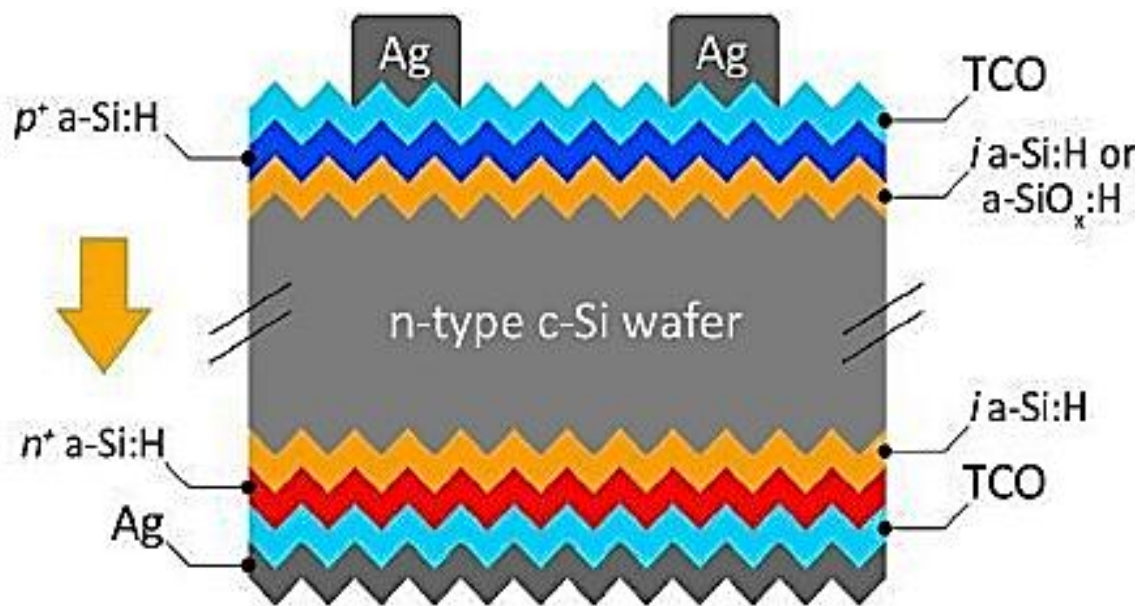
Figure 3.12*: n-type silicon heterojunction (SHJ) solar cell structure containing (TCO) electrode, and silver grid fingers [82].

The i-a-Si:H layers properties could be largely affected by numerous factors, typically including deposition power, pressure, temperature [83], hydrogen dilution [84], in-situ hydrogen plasma treatment (HPT) [85], thermal annealing [86], bi-layers [87], etc. Moreover, intrinsic silicon-based alloy alternatives such as amorphous silicon-oxide (a-SiO_x:H) [88] and amorphous silicon-carbide (a-SiC_x:H) [89] are applicable for improving c-Si surface passivation too. Zhang et al. showed that i-a-Si:H bi-layer with a porous interfacial layer improved the minority carrier lifetime [90]. Similarly, Sai's group also demonstrated that i-a-Si:H bilayer with a porous interfacial layer with high hydrogen content could substantially improve the implied V_{OC} and pseudo fill factor (pFF) of SHJ solar cells [87].

In 2019, a conversion efficiency of 25.11 % was achieved on a front-rear structured SHJ solar cell, fabricated by Hanergy and certified by the Institute for Solar Energy Research in Hamelin (ISFH) [80], with a fill-factor of 84.98 % which was the highest ever reported for all SHJ solar cells. Previously Kaneka demonstrated *FF* of 83.5 % for front-rear [91] and 84.65 % for silicon heterojunction interdigitated back-contacted (SHJ-IBC) structures [92]. The incremental of *FF* was mainly driven by the reduced R$_s$.

3.4.1.4   Tunneling-oxide passivating contact (TOPCon)

PV research community has proposed a new structure of solar cells featuring passivated carrier-selective contacts in order to overcome the problems mentioned previously for the presented high-efficiency solar cell concepts (e.g. the considerable fabrication costs). One model of that is solar cells featuring tunnel-oxide passivated contact (TOPCon). That type of solar cell was first suggested by the Fraunhofer Institute in Germany [93, 94], with a substrate structure of ultra-thin silicon oxide (SiO_x) and a heavily doped polycrystalline silicon (poly-Si) layer. The most interesting feature in the TOPCon structure regards the rear surface, where a silicon oxide layer (SiO_2) with a thickness of $\cong$1.5 nm is placed between the c-Si substrate and the doped poly crystalline Si layer [30]. A schematic view of the mentioned solar cell is depicted in Figure 3.13.
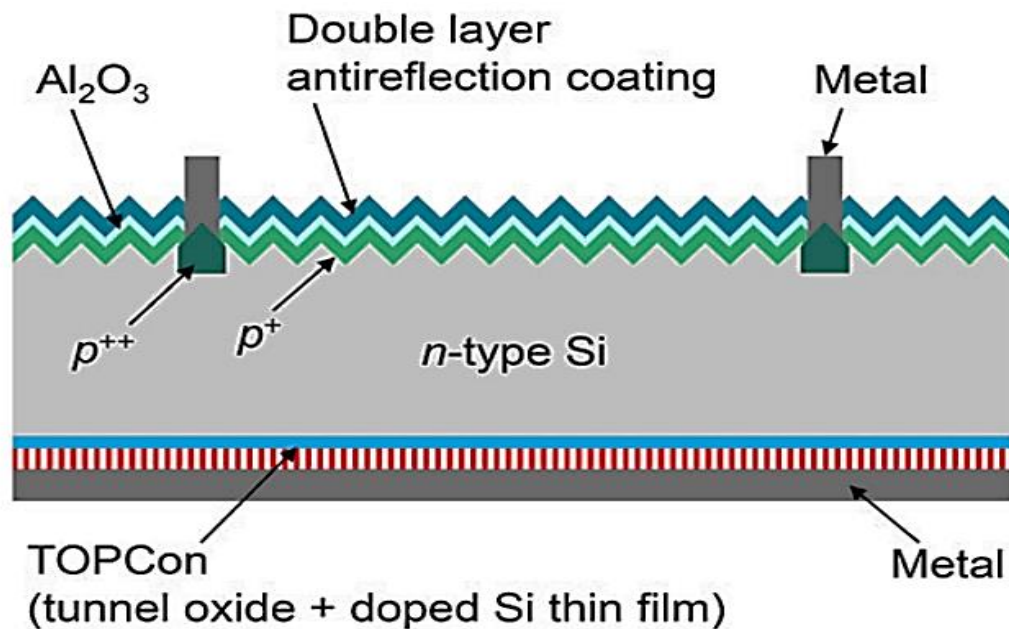
Figure 3.13: TOPCon solar cell structure.

The Tunnel Oxide Passivating Contact (TOPCon) has so far attracted the interest of industry the most due to its special structure. In the TOPCon structure, the wafer is not contacted by metal directly. Rather, a thin tunnel oxide and then a heavily n- or p-type doped poly-Si layer is deposited which, finally, is contacted by metal. Hence such structures are generally called passivating contacts [30]. The presence of tunnel oxide reduces minority carriers' recombination and simultaneously does not hamper majority carriers' flow. The process occurs since a potential barrier is formed in the valence and conduction bands of the Si semiconductor. This barrier blocks the passage of minority carriers while majority carriers pass through the tunneling effect. Thus, it increases the majority carrier concentration near the contact, and decreases minority concentration,

therefore decreases the recombination rate, and therefore, provides high open-circuit voltage (V_{OC}) and high fill factor FF [30].

TOPCon cells use a tunnel oxide with a thickness of approximately less than 2 nm ($\cong$1.5 nm) at the rear contact region, which is fully passivated. The tunnel layer should therefore be designed considering the thickness of the tunneling oxide in order to suppress and maintain the minority-carrier current; this reveals that a lower oxide thickness degrades V_{OC} (so increasing the minority-carrier current) while the higher one, degrades FF (thus decreasing the majority carrier tunnel current). It is sensitive to adjust the oxide thickness in the order of angstroms; therefore, determination of the optimal oxide thickness is critical [31, 95]. The dielectric constant, tunnel masses and barrier heights of the TOPCon structure are important in terms of both electrons and holes; since these parameters determine both majority- and minority-carrier tunnel currents at the rear region. Therefore, the bulk doping type that determines the majority carrier will affect the TOPCon solar cell performance. Steinkemper et.al.[96] reported the numerical simulation of n-type TOPCon solar cells regarding rear passivation contact from V_{OC} and FF aspects. Their studies focused on electrical properties like the tunneling mass or surface recombination velocity (SRV) at an approximately 1.5 nm thick tunneling oxide. Other studies also reported the effect of tunneling oxide thickness by taking some values like 0.4, 0.8, 1.2, and 1.6 nm for n-type Si bulk [95, 97], and this literature suggests the importance of the tunneling oxide thickness for designing TOPCon solar cell.

The most common dielectrics used as tunneling layers are: SiO_2 [98], Si_3N_4 [31], Al_2O_3 [99], and the prospective TiO_2 and HfO_2 [31].
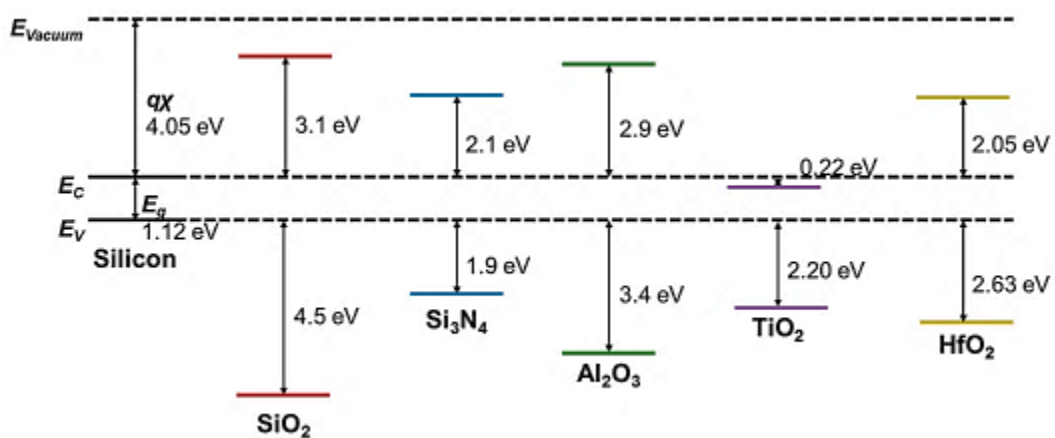
Figure 3.14: Energy band diagram of Si and some of tunneling dielectrics [31].

TOPCon Solar cells demonstrated conversion efficiency even above 25% [34, 96]. At the laboratory level, ISFH/Hannover has increased the maximum efficiency of polysilicon passivated contact solar cell efficiency up to 26.1% [100]. Daming Chen et al. developed large area industrial silicon solar cells with the tunnel oxide passivated contacts (i-TOPCon) design and confirmed champion efficiency of 24.58% [101]. Ying-Yuan Huang et al. reported an efficiency of 22.6% for a fully screen-printed bifacial large area n-type Si solar cell with lightly doped ion-implanted boron emitter and tunnel oxide passivated rear contact [102].

4. *Chapter 4: General properties of defects in semiconductors*

4.1 Introduction

All semiconductor materials found in nature are insulators when pure or when at a temperature of 0 K. The resistivity of a semiconductor is strongly influenced by the presence of impurities called dopants. In addition, it is agreed that the majority of semiconductors used today have values of resistivity concerning 10^{-4} -10^4 Ω cm at room temperature [103].

The crystal structure (perfect structure) is defined as a strictly periodic repetition of a motif of atoms in the three directions of space. There are intermediate situations between that ideal state and the amorphous ones that include most real solid crystals, in which the arrangement of the atoms in most of these solids always differs from the perfect structure; this difference is called defects.

Anything that alters the ideal crystal structure of a semiconductor will, in fact, affect its optical and/or electronic properties. Defects can have a very large influence on the material properties; as an example, the materials resistivity, carrier mobility, lifetime and optical properties, are all dependent on the precise defects present and their concentrations. Many electronic devices are essentially based on the controlled introduction of defects in the crystal. The perfect single crystal semiconductor has a band diagram that consists of a valence band (with top edge E_v), and a conduction band (with bottom edge E_c), separated by the bandgap E_g ($E_g = E_c - E_v$). When, the periodicity of the single crystals is perturbed by foreign atoms or crystal defects, the resulting lattice imperfections distort the electronic potential and may result in the introduction of discrete energy levels into the bandgap.

Defects are often classified in several ways. By taking into consideration their location in the crystal, they can be classified into bulk and interface defects. Furthermore, they can be classified by their creation method (structural viewpoint: vacancies, interstitial, substitution … etc.), by their energy state (shallow and deep defects), or by their mechanical, electrical, or optical effects …etc.

In this chapter, we will present the different type of structural defects. Then, we will focus on their electrical classification.

4.2 Types of defects

4.2.1 Point defects

The point defects are those resulting from the deviations of the perfect crystalline periodicity of the solid and not extended in space in any dimension. These can be missing atoms (vacancies), atoms at the wrong lattice site (antisite/ substitutional defects) [104], atoms between the ordinary lattice sites (interstitial defects), or complexes that form between different kinds of point defects. There are two kinds of point defects of great attention in semiconductor crystals, intrinsic (e.g. vacancies or self-interstitial) and extrinsic point defects (e.g. impurity atoms occupying substitutional or interstitial lattice sites). Small agglomerations of several point defects like divacancies, vacancy-impurity complexes, vacancy-donor... etc. are generally considered as point defects.

The point defects have a local effect, which usually affects only a few interatomic distances. They may be built-in with the original crystal growth, or activated by heat. Moreover, they may be the result of radiation, or electric current …etc.

4.2.1.1 Vacancy

The vacancy is defined as a missing atom from its original position from a node of the crystal lattice, which is meant to be filled (if an atom is removed from its regular lattice site, the empty lattice site is named a vacancy defect (V)), as shown in Figure 4.1. Vacancies are one of the most common intrinsic point defects absolutely. The vacancy is formed by removing an atom from its lattice site, by breaking its four bonds from the diamond crystal structure [105]. The broken bonds can form new bonds depending on the charge state of the vacancy, which is just the amount of electrons occupying the dangling bonds. This bonding causes small inward or outward displacements of neighboring atoms. This either preserves the local symmetry (relaxation) or alters it (distortion) and affects the crystal properties.

In defect modeling studies, there is general agreement in defect modeling studies that the energy of vacancy formation in germanium (1.7 eV – 2.5 eV) is significantly smaller than in silicon (~4.0 eV), for all charge states [106]. A divacancy can be formed when two neighboring atoms are removed or when two migrating vacancies meet and combine. It can also exist in four different charge states in Si [107].

The number of vacancies increases exponentially with the absolute temperature, and can be predestined using the following expression (Eq. 4.1) [108].

$$n_V = N \cdot exp\left(-\frac{E_{Va}}{K.T}\right) \qquad (4.1)$$

Where, n_V is the number of vacancies, N is the total number of lattice sites and E_{Va} the energy necessary to form a vacancy.
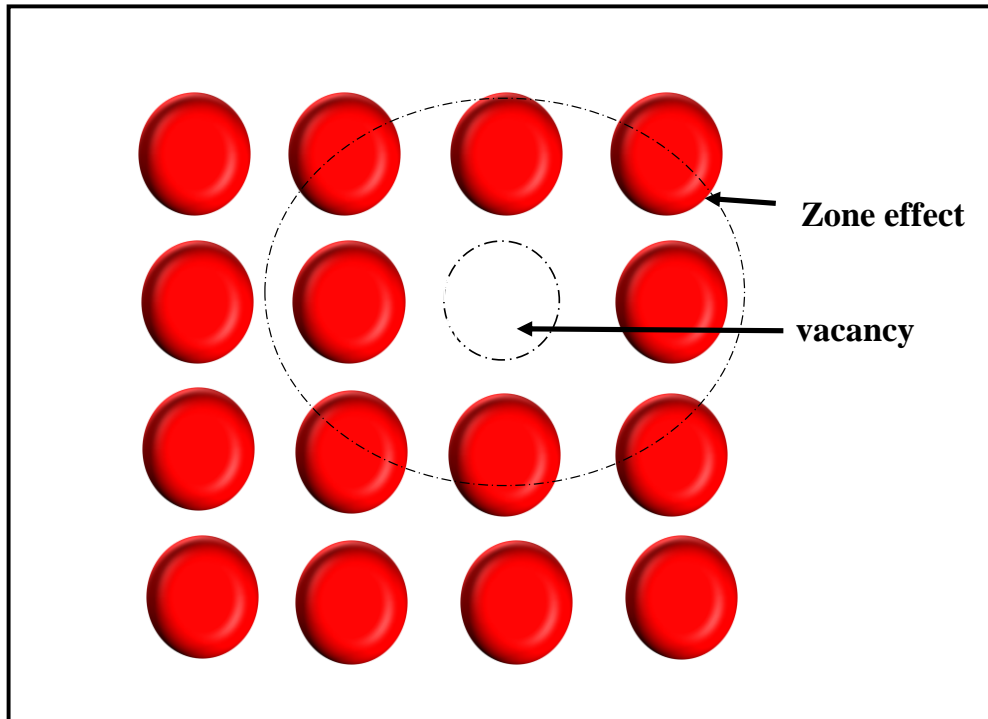
Figure 4.1: Schematic representation of vacancy defect at the atomic scale.

4.2.1.2 Interstitial

Interstitials are atoms that can occupy a site in the crystal structure, which is not a regular lattice site. An interstitial defect with the same species as the atoms of the lattice is called self-interstitial (or intrinsic interstitial). An interstitial impurity (or extrinsic interstitial) has different nature from the lattice atoms. Interstitials require generally high energy to be formed. The introduction of an interstitial induces relaxation and distortion of the lattice, which surrounds it. The kind of configuration that the interstitial assumes depends on its ability to create bonds with its neighbors and thus can change with its charge state [109]. A close-by interstitial defect and vacancy defect is termed a Frenkel pair.
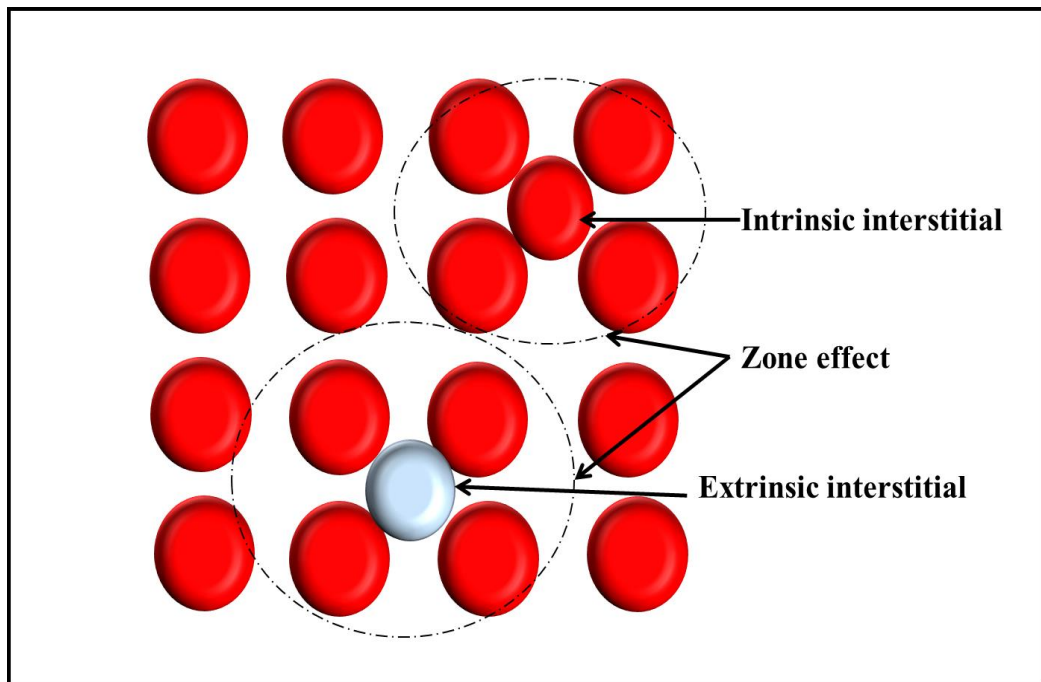
Figure 4.2: Schematic representation of interstitial defect.

4.2.1.3 Substitution

The substitution is defined as a presence of an atom with a different type than the bulk atoms. It is a foreign atom on a site that belongs, in the ideal case, to an atom of the crystal. Generally, substitutional impurity atoms are close to the bulk atoms in size (approaching 15%) [103].
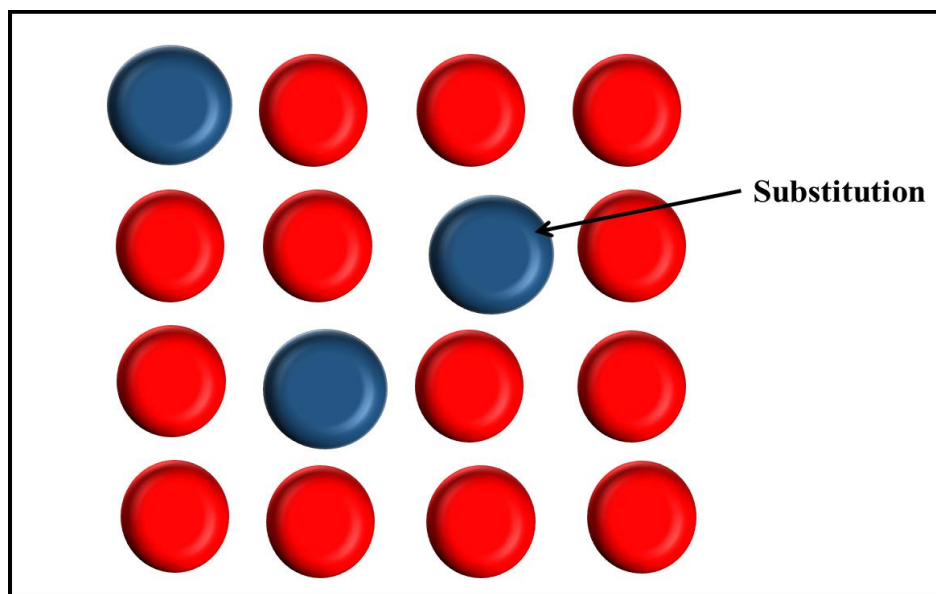
Figure 4.3: Schematic representation of substitution defect.

4.2.1.4 Anti-site

The most common defects in compound semiconductors are vacancies and anti-site defects. Anti-site is neither a vacancy nor an interstitial, nor a substitution. It occurs when an anion (cation) replaces a cation (anion) on a regular cation (anion) site. The energies of formation (and therefore the electronic states) related to these defects rely on the position of the Fermi energy (the doping level) and strain. The anti-site defects are the foremost important defects in the majority of compound semiconductors.
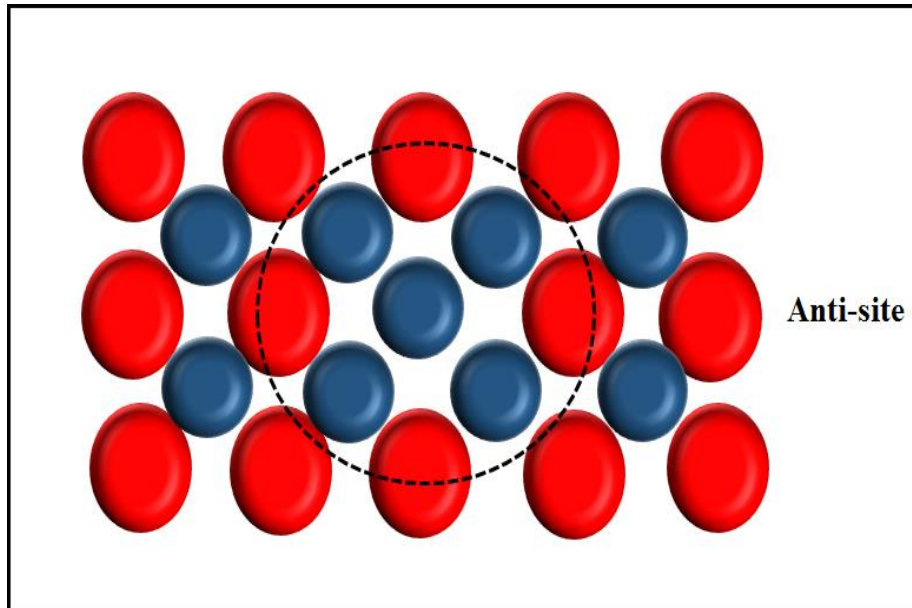
Figure 4.4: Schematic representation of Anti-site defect in compound materials.

4.2.1.5 Frenkel defect

It is a defect formed when an ion is displaced from a regular lattice site to an interstitial one. Thus, a Frenkel defect is in reality a pair of defects, which consist of an empty lattice site (vacancy) and an extra interstitially positioned atom. Cations that have small sizes are generally displaced to an interstitial site, as the interstitial space is small. The presence of a Frenkel imperfection in the crystal does not change its general electrical neutrality of it.
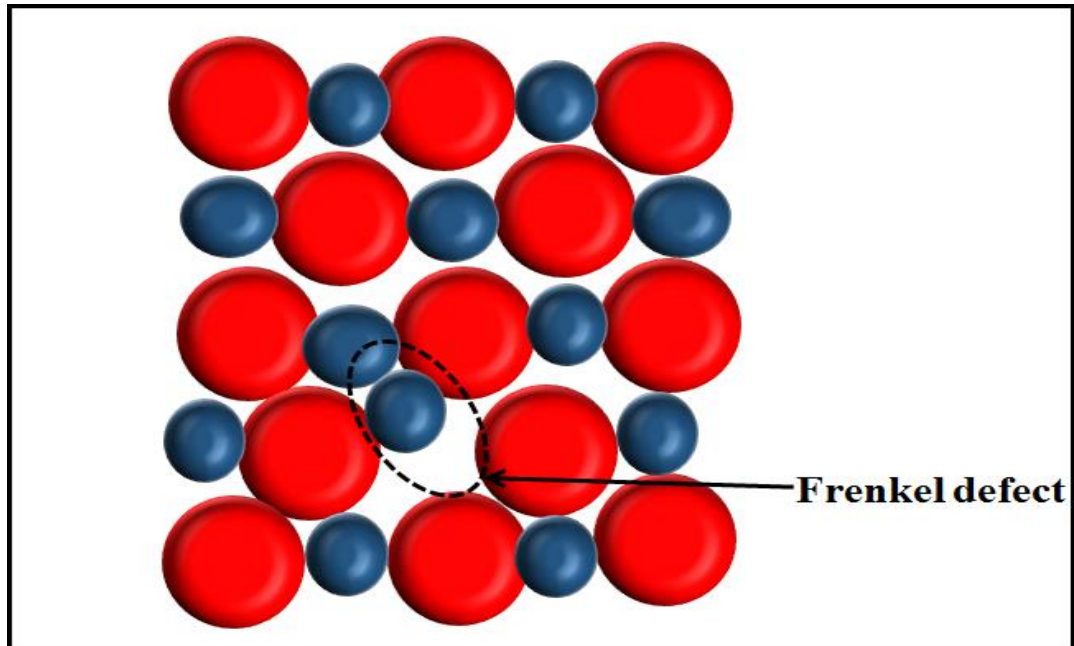
Figure 4.5: Schematic representation of Frenkel defect at the atomic scale.

4.2.1.6 Schottky defect

A Schottky defect is a missing pair of cation and anion from the original lattice site on the surface of the crystal. Therefore, the Schottky defect maintains the charge neutrality of the crystal.
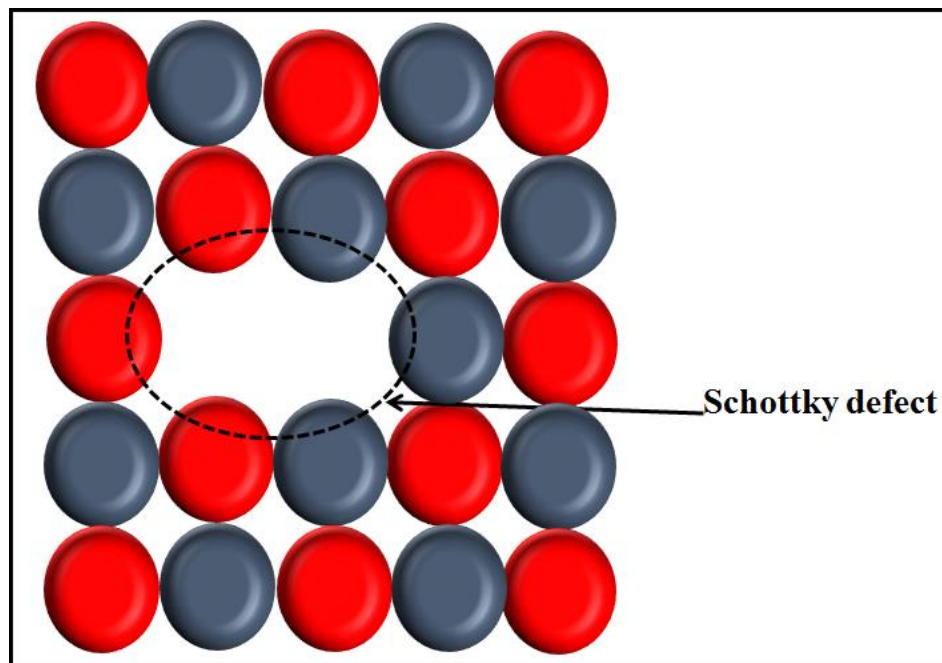
Figure 4.6: Schematic representation of Schottky defect at the atomic scale.

4.2.2 Line defects

Line defects or dislocations are formed when a number of atoms of the crystal lattice are misaligned. The termination of a plane of atoms within the center of a crystal causes edge dislocations; adjacent planes bend around the edge of the terminating plane. Dislocations may move if the atoms from one of the surrounding planes break their bonds and re-bond with the atoms at the terminating edge. Line defects can be either "screw" dislocations, in which a helical path is traced around the dislocation line, or "mixed", which is neither a pure edge nor a pure screw. In real crystals, most dislocations are probably a hybrid of the edge and screw forms and often form complete loops.

4.2.2.1 Edge Dislocations

It is well known that the general shape of an ideal crystal consists of several parallel vertical planes. Such planes are extended from top to bottom completely and parallel to side faces, in which the atoms are in equilibrium positions and the bond lengths are in equilibrium value. Herein, we can define the edge dislocation by being the end of one of the vertical planes midway within the crystal and does not extend from top to bottom face.
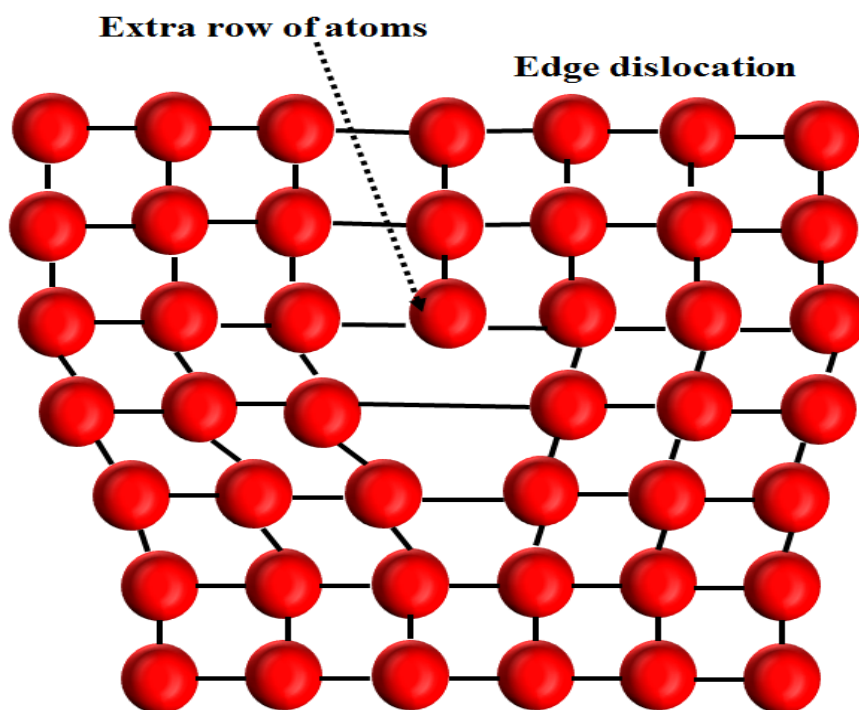
Figure 4.7: Schematic representation of Edge dislocation in a cubic crystal.

4.2.2.2 Screw Dislocations

A screw dislocation marks the boundary between skidded and the non-skidding parts of the crystal, which can be created by cutting the crystal partially and then lowering one part relative to the other, by horizontal atomic spacing. This is shown in Figure 4.8.
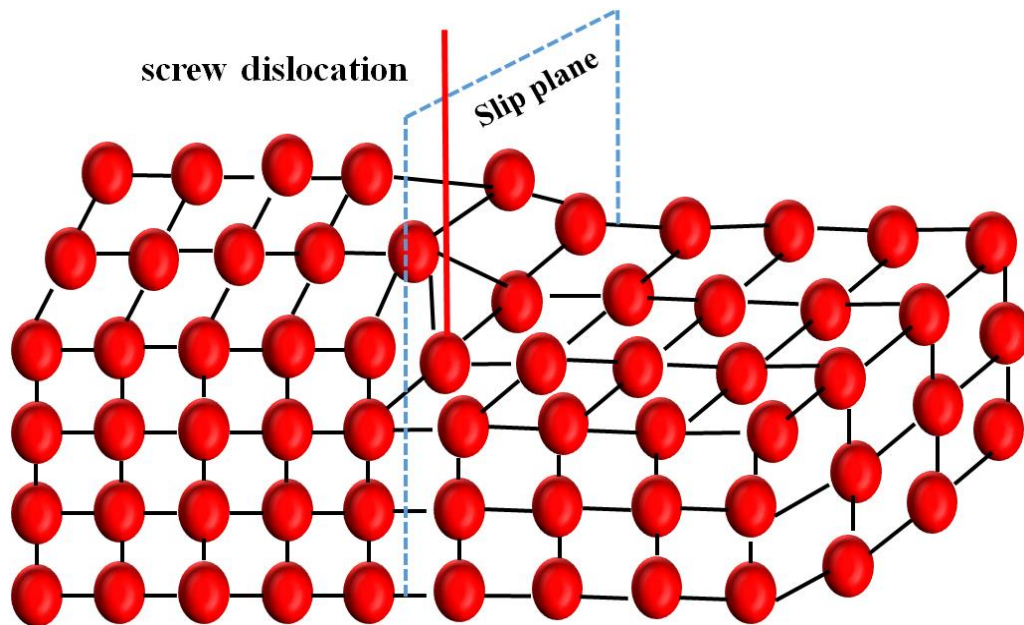
Figure 4.8: Schematic representation of screw dislocation in a cubic crystal.

4.3 Electronic Defect States

The presence of defects in the crystal structure always modifies or ruptures atoms bonds. Then it forces neighboring atoms to readjust their positions by relaxations of various kinds, and sometimes form new bonds with other neighbors. The relaxations and rebounding processes lead to the shape of recent orbitals localized within the vicinity of the defect and usually have the power to capture Surplus charge from the valence or conduction bands. The capture process represents the defect ionization that depends on the charge availability within the solid as quantified by the Fermi level.

Electrically active defects in semiconductor crystals have different characteristics. They may be classified as shallow and deep level defects, depending on their energy state location relatively to the conduction or valence band edge.

4.3.1 Classification

Defect charge can affect numerous sides of defect properties, including physical structure, diffusion rate, chemical reactivity, and interactions with the electrons that give the semiconductor its overall characteristics.

4.3.1.1 Shallow Defects

Shallow levels are defects located near their related band edges i.e. ~0.1 eV from the band edge (E_v valence band edge for acceptors and E_c conduction band edge for donors); thus these levels are thermally ionized at room temperature. A modified hydrogenic model [110] qualifies, approximately, the ionization energy of a shallow level. For example, a shallow donor resembles a hydrogen atom with a positive nucleus binding an electron. Impurity elements, which are normally used as dopants in semiconductors normally, create these shallow levels, which are ionized at room temperature and provide free carriers to create p-type or n-type semiconductors. The ionization energy for the hydrogen atom in a vacuum is

$$E_H = \frac{m_0 q^4}{32\pi^2 \varepsilon_0^2 \hbar^2} = 13.6 eV \tag{4.2}$$

where $\hbar$ is the reduced Planck constant. The ionization energy (E_D) is calculated by replacing the electron rest mass (m_0) by the conductivity effective mass of electrons (m_{ce}), and the vacuum permittivity (ε_0) by the permittivity of the semiconductor (ε_S) [110]:

$$E_D = E_C - E_d = \left(\frac{\varepsilon_0}{\varepsilon_S}\right)^2 \left(\frac{m_{ce}}{m_0}\right) E_H \tag{4.3}$$

The ionization energy for donors as calculated from (eq 4.3) is 25 meV for Si [111].

These energy levels are efficient at calculating the dopants fraction being ionized, or electrically active. In addition, since these small ionization energies are comparable to the thermal energy ($k_B T$), ionization is usually perfect at room temperature.

4.3.1.2 Deep defects

Deep levels are those defects positioned deeper in the bandgap (E_g) than the dopant levels, and are found to bind the carriers much more strongly into highly compact, localized states. They introduce energy levels deeper within the bandgap at a position denoted (E_t). The deep levels have higher ionization energies; therefore contribute little to the free charge carriers.

Typically, the deep levels lie between 0.1 eV and mid-band gap. Usually, the deep levels that locate above mid bandgap are acceptor-like (-/0), i.e., they are negatively charged when occupied and neutral when empty. These are referred to as deep acceptor-levels or electron traps. Those below the mid bandgap are normally donor-like (+/0), i.e., positively charged when empty and neutral when full of electrons. Another view is that they are positively charged when hole-filled and neutral when holes are emitted. These are referred to as deep donor-levels or hole traps [103].

A deep-level may act as a minority carrier trap, majority carrier trap or recombination center depending on its position in the bandgap, and on relative capture cross-section of minority and majority carriers. A majority carrier trap is an electron trap in an n-type semiconductor or a hole trap in a p-type semiconductor. Conversely, a minority carrier trap is a hole trap in an n-type semiconductor or an electron trap in a p-type semiconductor. If a majority- or minority- carrier lives a mean lifetime in the captured state, and is then thermally ejected to the band from which it came, the center may be regarded as a majority carrier trap or minority carrier trap respectively.

Deep levels are important in semiconductors whether they are traps or recombination centers. As traps, they can capture free carriers supplied by shallow levels, therefore compensating them and reducing the effective doping density, which leads to a reduction of conductivity.

Deep levels are desirable in some applications, e.g. in fast switching devices, where they can be exploited as recombination centers that quickly remove minority carriers, enhancing the device's switching speed thereby increasing efficiency.

Deep levels may also be a nuisance if present in semiconductors that are used for photovoltaic applications since they reduce the cells efficiency by allowing created electron-hole to recombine. Thus, the deep level study is of paramount importance in the semiconductor device industry so that those deep levels, which are useful, can be deliberately added and those that are deleterious can be reduced or eliminated.

From defect spectroscopy measurements such as deep level transient spectroscopy (DLTS), it is possible to extract the defect properties such as the concentration, energy level, and capture cross-section of defect level. The capture cross-sections σ of the majority or minority carriers can be used to deduce whether the defect will act as a majority carrier trap, a minority carrier trap, or a recombination center.

4.3.2 Definition of a trap or recombination center

A total simplification of a trap or recombination center is given in idioms of the capture rates in a neutral region within a semiconductor, and the thermal emission rates in the depletion region of a Schottky barrier or the p-n junction [112].

At first, in a neutral semiconductor, a deep level named a recombination center if the capture rates for electrons and holes are large and comparable. A deep level is referred to as an electron trap, for example, if its electron capture rate is at least an order of magnitude greater than its hole capture rate, that is $C_n > C_p$ where C_n and C_p are respectively the electron and hole capture rates in s^{-1}.

Generally, the recombination rate depends on the defect density (or the recombination center density), the free carrier concentration, the electron and hole capture cross sections (σ_n and σ_p) and the energy level position. It is also known that the free electron and hole densities, n and p respectively, are near zero in the depletion region; here the thermal emission rate is more useful than the capture rate for characterizing the behavior of deep levels.

If a deep level has comparable (and large) emission rates for electrons and holes then it is referred to as a generation center, equivalent to a recombination center in a neutral region.

For traps, it is also useful to differentiate between minority and majority traps. A majority traps have a much larger capture rate for majority carriers than for minority carriers. For example, an electron trap is a majority trap in an n-type semiconductor and a minority trap in a p-type semiconductor. These definitions are summarised in Figure 4.9.

The Fermi level commands the occupation of traps and shallow levels. It is therefore beneficial to explain the charge state of electron and hole traps in relation to their Fermi level position. Miller et al.[113] give another definition: "An electron trap is full (of electrons) and therefore is neutral when below the electron quasi-Fermi level E_{Fn}. Moreover, it is empty (of electrons) and thus positively charged when it is above Fermi level E_{Fp}. Similarly, a hole trap is the foil of holes and so neutral when it is above the hole quasi-Fermi level (E_{Fp}) and empty of holes where it is negatively charged and below (E_{Fn}).
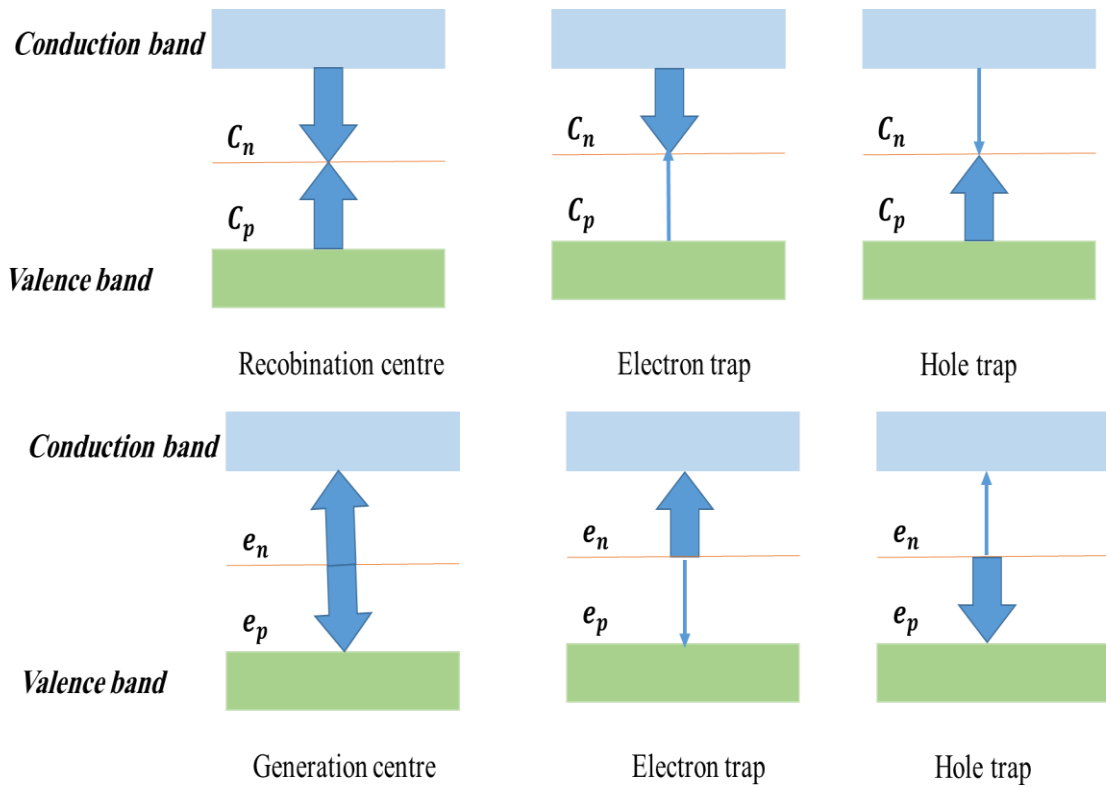
Figure 4.9: Generation-Recombination statistics (Interactions with the conduction and the valence bands).

4.3.2.1 The rate equation

In the presence of traps within the bandgap of the semiconductor, electron and hole transitions occur. That process derived its theory from Shockley and Read [21] and then by Hall [26]. Therefore, these types of defects are referred usually to as Shockley-Read-Hall (SRH) centers. This process contains two essential steps, electron capture, electron emission, hole capture and hole emission. Labeled a, b, c and d, respectively, in Figure 4.10. These processes could be due to a thermal or optical process.

The presence of traps of volume density N_t, which introduces a deep energy level into the bandgap of the semiconductor at position E_t. The level can react with the conduction and valence bands through emission and capture of electrons and holes respectively. Thus, the following four processes need to be considered:

- Emission of electrons to the conduction band with emission rate e_n (in s^{-1}).
- Emission of holes to the valence band with emission rate e_p.
- Capture of electrons from the conduction band with capture rate c_n (in s^{-1})

- Capture of holes from the valence band with capture rate c_p.
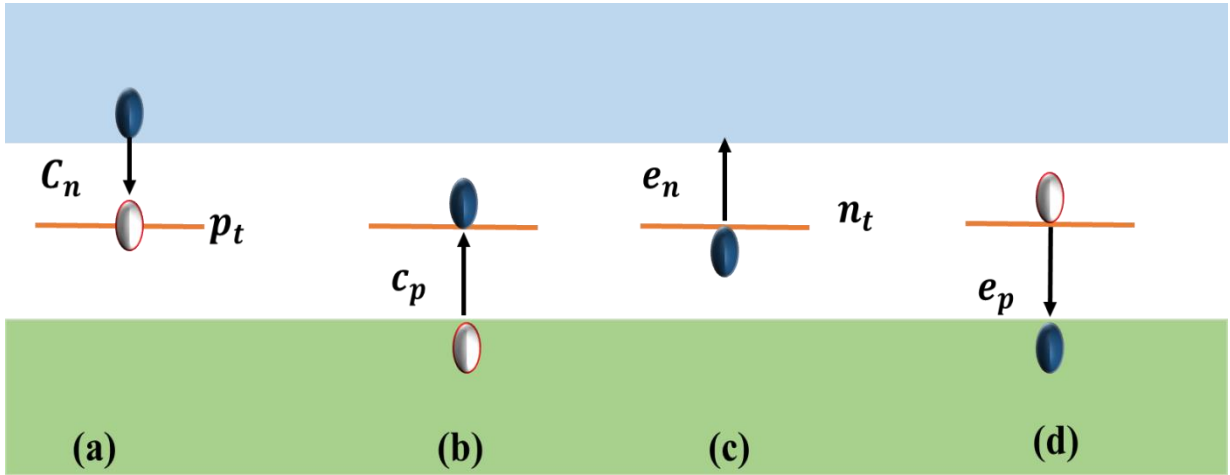
Figure 4.10: Interactions between a deep energy level and the two bands. Electrons and holes are represented by blue and white symbols, respectively.

The volume density n_t of filled traps is set by the competition of those four processes. The emission of electrons and therefore the capture of holes take place from the filled traps, while the emission of holes and therefore the capture of electrons take place from the $(N_t\text{-}n_t)$ empty traps. The interactions are described by the rate equation:

$$\frac{dn_t}{dt} = -\left(e_n + c_p\right)n_t + \left(c_n + e_p\right)(N_t - n_t) \tag{4.4}$$

The steady-state occupancy ratio of the trap is determined by the condition $\frac{dn_t}{dt} = 0$ as

$$\frac{n_t(\infty)}{N_t} = \frac{c_n + e_p}{e_n + c_n + e_p + c_p} \tag{4.5}$$

In n-type material, we have a particular interest in the two special cases, where (i) all traps are initially empty and electron capture is the dominant process, and (ii) all traps are initially full of and electron emission is the dominant process. In these cases, the solution to equation (4.5) is given by:

$$\begin{aligned}
n_t(t) &= N_t(1 - exp(-c_n t)), \quad n_t(t = 0) = 0, c_n \gg e_n, e_p, c_p \\
n_t(t) &= N_t\, exp(-e_n t), \quad\quad\ \ n_t(t = 0) = N_t, e_n \gg c_n, e_p, c_p
\end{aligned} \tag{4.6}$$

Thus, the volume density n_t of filled traps relaxes exponentially towards the steady state values $n_t(\infty) = N_t$ for the capture process and $n_t(\infty) = 0$ for the emission process. The time constants for the processes are given by the inverse capture rate$(c_n)^{-1}$and the inverse emission rate $(e_n)^{-1}$, respectively.

4.3.2.2 The capture process

The electron capture rate $c_n$is proportional to the flux of conduction electrons that passes the center of defect. Thus:

$$c_n = \sigma_n \langle v_n \rangle n_c \qquad (4.7)$$

where;

$$\langle v_n \rangle = \sqrt{\frac{3k_BT}{m_{ce}}} \qquad (4.8)$$

Is the average thermal velocity (in cm s^{-1}) of conduction electrons, and the proportionality constant σ_n, is the electron capture cross section in (cm^2), m_{ce} is the conductivity effective mass of electrons and n_c is the electron concentration in the conduction band .

The value of the capture cross section has approximately atomic dimensions and describes the effectiveness of the center of defect to capture electrons. The product $\sigma_n \langle v_n \rangle$ is known as the capture coefficient (units of cm³s⁻¹). The capture cross section can be independent of temperature or can be thermally activated. In the latter case, the cross section is usually found to follow the behavior [114]:

$$\sigma_n(T) = \sigma_n^\infty exp\left(-\frac{E_{\sigma_n}}{k_BT}\right) \qquad (4.9)$$

Where $E_{\sigma_n,}$ is the energy barrier for capture of electrons and $\sigma_n^\infty$is the electron capture cross section in the limit T $\rightarrow \infty$ [114].

In most cases, the value of the carrier capture cross section can indicate the charge state of the defect centre emptied for carriers. For Coulombically attractive centers, the carrier capture cross section is expected to be$\geq 10^{-14}cm^2$, while one expects this value to be in the range $10^{-16} - 10^{-14}cm^2$ for a neutral defect center and $\lesssim 10^{-17}cm^2$for a repulsive center [115].

4.3.2.3 The emission process

In thermodynamic equilibrium, the principle of detailed balance is applied. This principle states that the exchange of electrons between the deep level and the conduction band and the exchange

of holes between the deep level and the valence band are both balanced, i.e. $e_n n_t = c_n(N_t - n_t)$ and $e_p(N_t - n_t) = c_p n_t$. Combining this principle with Fermi-Dirac statistics yields the electron emission rate [116]:

$$e_n = \sigma_n \langle v_n \rangle \frac{g_0}{g_1} N_c \, exp\left(-\frac{E_c - E_t}{k_B T}\right) \tag{4.10}$$

Where g_0 and g_1 are the degeneracies of the empty and filled energy level, respectively. The temperature dependence of the electron emission rate is determined from the temperature dependencies of the thermal velocity Eq.(4.8), the electron capture cross section Eq.(4.9), the ionization energy Eq.(4.3) and the effective density of states $\left(N_c \propto T^{3/2}\right.$ [117]). The result is:

$$e_n(T) = \gamma_n T^2 \sigma_n^a \, exp\left(-\frac{E_n^a}{k_B T}\right) \tag{4.11}$$

Where:
$$E_n^a = \Delta H_n + E_{\sigma_n} \tag{4.12}$$
$$\sigma_n^a = \frac{g_0}{g_1} \sigma_n^\infty exp(\Delta S_n / k_B) \tag{4.13}$$

γ_n is a constant, E_n^a is the activation energy and σ_n^a is electron capture cross section.

A plot of $\ln(e_n/T^2)$ versus inverse temperature T^{-1} (an Arrhenius plot) gives a straight line with a slope giving the activation energy E_n^a, and the intersection of $\ln(e_n/T^2)$ with the vertical axis provides the apparent electron capture cross section σ_n^a. This, however, does not directly determine the ionization energy $E_c - E_t$ and the true electron capture cross section σ_n. In the case of temperature-independent electron capture, the activation energy E_n^a equals the enthalpy change ΔH_n for the emission process.

The emission rate e_p for emission of holes to the valence band is described by expressions similar to Eqs. (4.11) - (4.13).

4.3.3   Defect production by Irradiation

It is important to describe the dynamics of collision because it is fundamental to defect creation in semiconductors. Assume that an incident particle with kinetic energy E and mass M_1 strikes a target atom of mass M_2 (Figure 4.11).
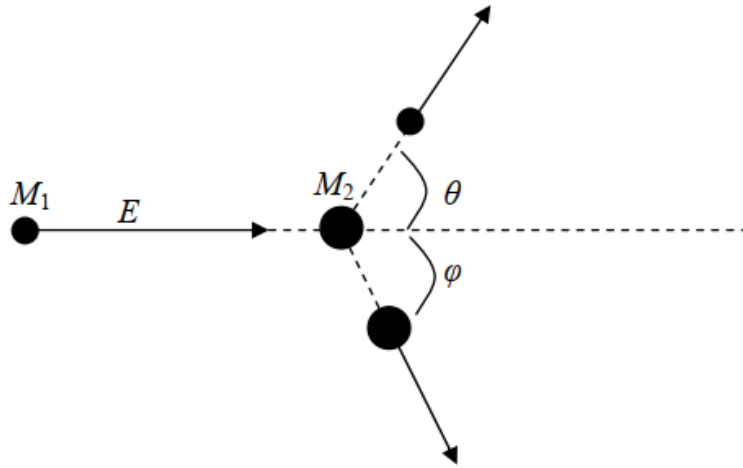
Figure 4.11 : Illustration of the collision between an incident particle of mass M_1 and energy E with a target atom of mass M_2.

The kinetic energy T transmitted to the target atom depends directly on the angular deflection θ of the incident particle (Figure 4.11). For purely elastic collision, (i.e. when momentum and kinetic energy are conserved) the energy transferred is given by [116]

$$T = 2E \frac{M_1}{M_2} \frac{1 - \eta(\theta)}{(1 + M_2/M_1)^2} \tag{4.14}$$

Where, E is the energy of the projectile and M_1 and M_2 have previously been defined and $\eta(\theta)$ is a function implicitly given by

$$cos\ \eta(\theta) = \frac{1 + (M_2/M_1)\eta}{\sqrt{1 + 2(M_2 \cdot M_1)\eta + (M_2/M_1)^2}} \tag{4.15}$$

In the non-relativistic limit, the maximum energy T_{max} is transferred for $\theta = 0$, i.e., for $\eta(\theta) = -1$, therefore [116]

$$T_{max} = \frac{4M_1 M_2}{(M_1 + M_2)^2} E \tag{4.16}$$

In the case where the mass of projectile is approximately equal to the target ($M_1 = M_2$), the expression of the transferred energy will be simplified to

$$T_{max} = E \tag{4.17}$$

For a neutron irradiation, $M_1 \ll M_2$ the energy transferred is now given by [116]

$$T_{max} = \frac{2M_1}{M_2} E \tag{2.17}$$

In the case of electron irradiation, $M_1 \ll M_2$, then relativistic corrections are required and the energy transferred in now written as [116]:

$$T_{max} = \frac{2M_1}{M_2} E \left(2 + \frac{E}{M_1 c^2} \right) \qquad (4.18)$$

where c is the speed of light.

4.4 Effects of defects

When the uniformity of the crystalline lattice is disorganized by the bulk damage cause, new energy levels appear in the forbidden bandgap. Macroscopic evidence for this is available from changes in the bulk electrical characteristics as will be discussed in the following sub-sections.

4.4.1   Effects on leakage currents

In the silicon devices, a little leakage current can arise in the depletion region, from the thermal generation of electron-hole pairs as some electrons gain sufficient energy to move from the valence band to the conduction band, leaving a hole within the valence band and an electron within the conduction band. A large leakage current is raised with the presence of mid-band gap defects. In practice, deep levels can interact with leakage related to carriers in the conduction band or valence band [118]. When a leakage current is present, the majority carrier capture rate cannot be neglected in comparison with the majority carrier emission rate. In such cases, the leakage current has a serious influence on the DLTS spectra and, therefore, on deep level parameter determination[118]. It can thus lead to an incorrect interpretation of experimental results.

4.4.2   Effects in lifetime shortening

It is well known that charge carrier lifetime is an influential parameter for many kinds of silicon devices. The control of the charge carrier lifetime is, then, a key factor in the optimization of device performance. Carrier lifetimes may be defined as the mean times spent by excess electrons and holes in the conduction and valence band respectively. Carrier lifetime is very sensitive to the presence of electrically active defects. It is important to have short values of lifetime to obtain fast switching, but necessary to have long lifetimes for devices such as detectors and solar cells.

4.4.3   Effects on devices

Shallow level impurities are used almost exclusively to provide the necessary carriers, n- or p-type, in semiconductor devices. However, several special cases exist in which deep level defects are also necessary for the operation of a device. For example, in fast switching junctions, deep level traps are used to kill free carrier lifetimes by pulling carriers out of the conduction or valence

band. In the vast majority of cases, deep level defects are undesirable, since traps pose serious problems by eliminating free electrons and holes.

4.6 Defects in the SiO_2

Amorphous SiO_2 is a solid network (Figure 4.12), meaning that it comprises a network of Si-O chains and rings.
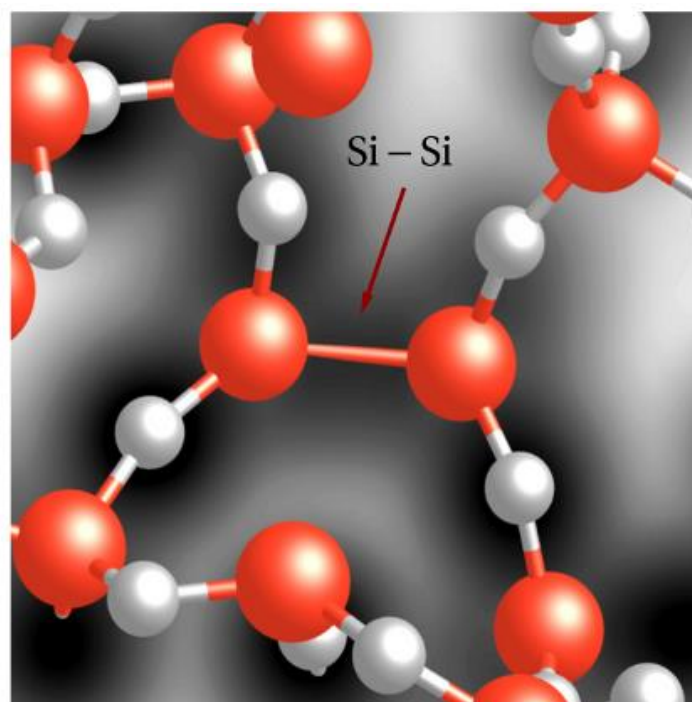
Figure 4.132: An electron density plot of an oxygen vacancy. Red and white spheres represents silicon and oxygen atoms, respectively, and bonds are shown as the sticks connecting these atoms. The Si-Si bond, established after the removal of an oxygen atom, is indicated by a high charge density (dark area) between the neighboring silicon atoms [119].

This structural peculiarity is a result of the fact that the constituent atoms preserve their coordination and juxtaposition; i.e., every Si atom is 4-fold coordinated and every O atom is 2-fold coordinated and Si atoms always connect to oxygens and vice versa. In terms of disruptions in this coordination and ordering, one can define intrinsic defects in amorphousSiO_2. The existence of a stringent ordering in Si-O chains (i.e., the fact that every Si has to be followed by an O and every O has to be followed by a Si) allows an unambiguous definition of an oxygen vacancy. If an O atom is missing from a Si-O chain, the two neighboring Si atoms may undergo some relaxation and produce a (usually strained) Si-Si bond, or, at least, one of the Si atoms may relax behind the

plane of its three remaining oxygen neighbors and bind to network oxygen or silicon atom (puckering). As opposed to oxygen vacancies, a silicon-vacancy would create four dangling oxygen orbitals resulting in a much greater relaxation of the amorphous network as observed in amorphous silicon [120]. The existence of four reactive orbitals in a small volume region would lead to the formation of e.g., peroxy linkages and thus to the restoration of the ring and chain structure of the glass, although with a deviation from the correct stoichiometry [120].

5. *Chapter 5: Tunneling Models and Device Simulation using SILVACO TCAD*

5.1 Introduction

The growing request for higher computing power, smaller dimensions, and lower power consumption of electronic devices leads to a pressing need to downscale semiconductor components. This operation has already led to reduced length scales, where quantum mechanical effects dominate the electrical device characteristics. One of the most interesting effects is the quantum-mechanical tunneling of charge carriers through classically forbidden regions. Therefore, it is needful to account for tunneling effects in the design of semiconductor devices. Several models of varying complexity and accuracy can be derived to describe the tunneling current density in semiconductor devices.

In this chapter, we will start by giving an overview of quantum tunneling. Then, we will shed light on the most tunneling mechanisms through the quantum barrier; taking into consideration the physical models used in silvaco TCAD. Finally, the numerical simulator SILVACO TCAD (used in this study) will be presented, and we will explain how this tool is applied to simulate the electric behavior of our device structure.

5.2 Tunneling Mechanisms

5.2.1 Basic principles of Quantum Tunneling

Quantum tunneling is the phenomenon in which particles penetrate a potential energy barrier with a height greater than the total energy of the incident particles. The phenomenon is interesting and important because it violates the principles of classical mechanics and can efficiently be explained by making use of the concept of duality (wave-particle nature of electrons). An electron can be signified by a wave function $\Psi(x)$ and an energy E, and its wave characteristics are governed by the Schrödinger equation (Eq.5.1) [121].

$$\frac{-\hbar}{2m^*}\frac{\partial^2}{\partial x^2}\Psi(x) + V(x) = E\Psi(x)$$

$$5.1$$

Where "$\hbar$" is reduced Planck's constant, $\Psi(x)$ the wave function, "m^*" is the electron effective mass, "V"- the potential energy of the barrier and "E" stands for the electron's energy.

The solutions of this equation at different boundary conditions will lead to a successful computation of an important tunneling parameter called transmission coefficient (T), which tells us the probability of a carrier (for example electron (e^-)) to tunnel through a potential barrier.

After long mathematical derivation procedures, the final expression for the transmission coefficient (T) can be given as [122]:

$$T = 16 \left(\frac{E}{V}\right) e^{-2\sqrt{\left(\frac{2m}{\hbar^2} \cdot V\right) \cdot a}}$$

5.2

where "a" represents the thickness and "V" the height of the potential barrier.

The transmission coefficient (T) is affected by many factors such as the barrier height, thickness of the barrier, barrier shape, and the incident wave amplitude. Moreover, the transmission coefficient (T) shows a linear and exponential increase, following a decrease in the height and thickness of the tunneling barrier, respectively.

In addition, increasing the incident wave's amplitude will result in an increased "T". Depending on the barrier shape (eg. whether the barrier shape is rectangular, triangular, trapezoidal, or truncated parabolic), the expression for transmission coefficient (T) will give different forms. That is why the barrier shape is highly pronounced to determine the tunneling current passing through the barrier [121, 122].

The solution of Schrödinger equation within the region inside the barrier is given by the expression under Eq.(5.3)[122]:

$$\Psi_{II}(x) = A_{II} e^{-ix\sqrt{\frac{2m}{\hbar^2}(V)}}$$

5.3

Where A_{II} is amplitude of the incident wave.

From this expression, one can easily observe the presence of an exponential decay of the wave function inside the barrier, which is clearly visualized in Figure 5.1.

In moving from a relatively small bandgap material to another with a larger bandgap (e.g. from a semiconductor material to an insulator or another wide bandgap semiconductor), electrons encounter a rectangular potential barrier (V $\gg$ E). In such a case and according to the quantum theory, electrons will have a non-zero probability of penetrating the potential barrier and passing onto the other side, as illustrated in Figure 5.2.(b). Nevertheless, for classical physics, the barrier is a wall and carries could not pass to the other side (Figure 5.2.(a)).
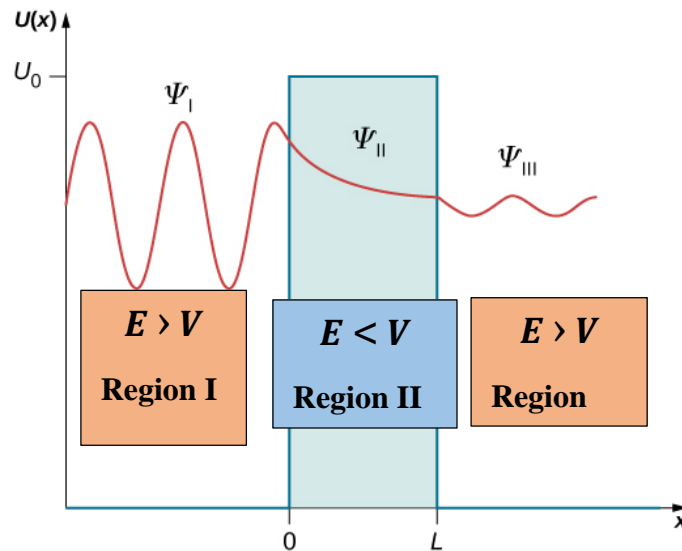
Figure 5.1: Incoming wave (Region I), quantum mechanical tunneling with exponential decay of the wave function (Region II) and the transmitted wave (Region III) [121].
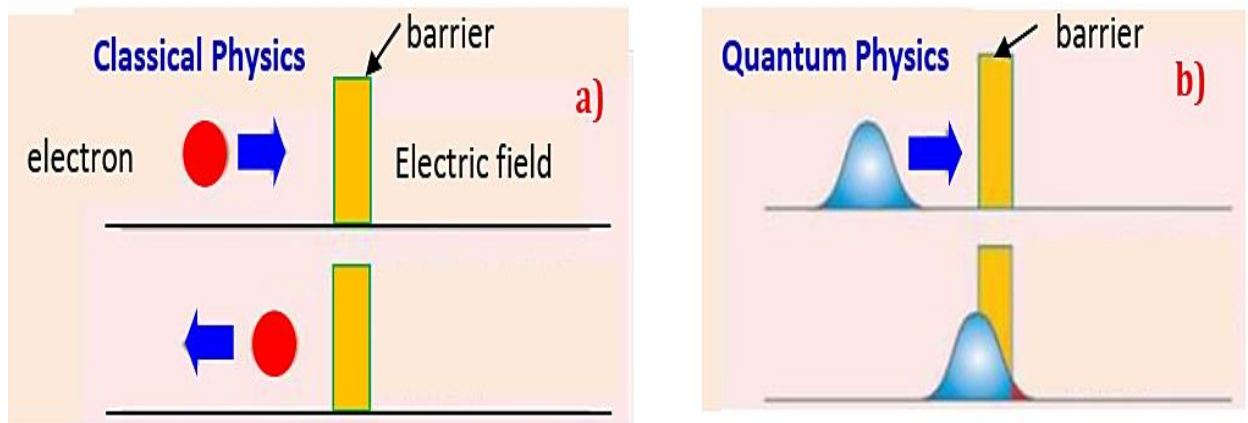
Figure 5.2: Schematic view of an electron encountering a potential barrier in : a) classical physics theory, b) quantum physics theory [123].

5.2.2 Tunneling mechanism across a thin barrier

The main target of the thesis work is the investigation of the tunneling barriers in tunnel oxide passivating contact (Topcon) solar cell. There is no doubt that the tunneling current is the center engine for that type of solar cell. Hence, it is crucial to describe the most common tunneling mechanisms through thin barriers. Here below are the possible transfer mechanisms governing the current transport across barriers, and their respective brief descriptions.

The mechanisms include Direct Tunneling (DT), Fowler-Nordheim Tunneling (FNT), Thermionic /Schottky Emission (SE), Poole-Frenkel Tunneling (PFT), and Trap-Assisted Tunneling (TAT).

Taking into account the physical models used in SILVACO software that express each tunneling mechanism [124] [125] [126].

5.2.2.1 Direct Tunneling (DT)

From the basic principle of quantum tunneling, we know that electrons would face a potential barrier in traversing from a low to high bandgap material. In addition, there is another truth that in the presence of an external electric field, the barrier deforms and changes its shape. As a result, incident carriers (electrons or holes) will see a trapezoidal barrier, which is narrower than the case in the absence of an external field [124].

Figure 5.3 consider a MOS structure as an example, with thin oxide layer and low oxide field. Here, the electrons from the metal surface will be able to tunnel directly through the forbidden energy barrier formed by the dielectric layer to the semiconductor conduction band. This is what we called direct tunneling (DT). It is strongly gaining significance when the dielectric layer gets thinner.
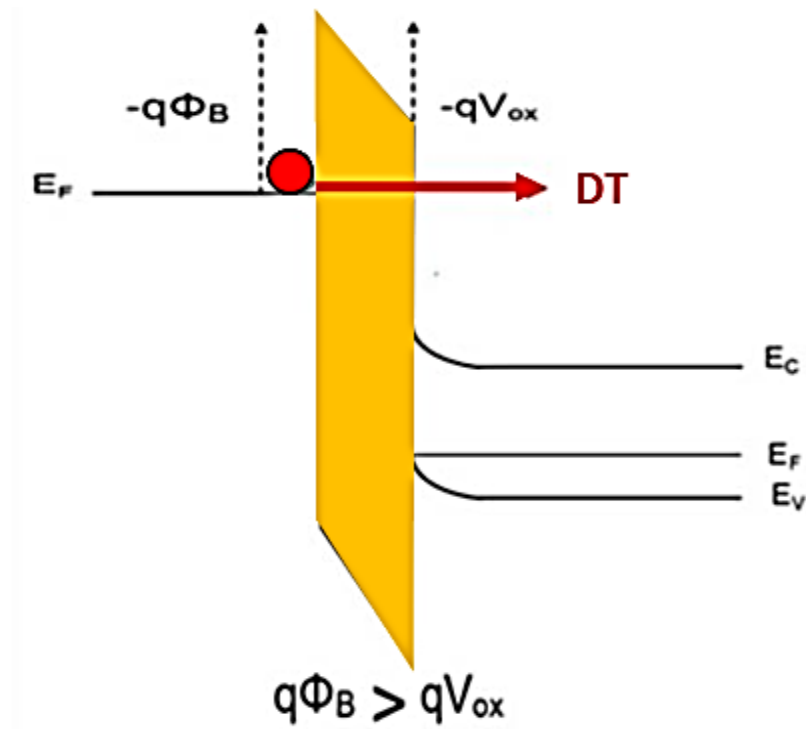
Figure 5.3: Illustration of direct tunneling (DT) through the energy band-diagram of a metal-oxide semiconductor structure.

A common approach to model the tunneling current is the Tsu-Esaki formula [127]

$$J_{DT} = \frac{4\pi q m^*}{h^3} \int_{E_{min,0}}^{E_{max}} TC(E_x, m_{\text{diel}})N(E_x)\mathrm{d}E_x \qquad 5.4$$

where h is Planck's constant, q is the electron charge, m^* is the effective silicon electron mass, m_{diel} the effective electron mass in the dielectric, $TC(E_x, m_{\text{diel}})$ is the transmission coefficient, and $N(E_x)$ the supply function, which is given as [125]:

$$N(E_x) = k_B T \, ln\left(\frac{1 + \exp[(E_{Fl} - E_x)/k_B T]}{1 + \exp[(E_{Fr} - E_x)/k_B T]}\right) \qquad 5.5$$

Here, E_{Fr} and E_{Fl} are the quasi-Fermi levels on either side of the barrier.

The supply function describes the difference in the supply of carriers at the interfaces of the dielectric layer [125].

The values of $E_{min,0}$ and E_{max} in Eq. 5.4 depend on the considered tunnelling process; for the electron tunnelling from the conduction band, $E_{min,0}$ is the highest conduction band edge of the two electrodes and E_{max} is the highest conduction band edge of the dielectric [125].

Atlas simulator can account for several types of tunneling. All these types of tunneling can be used as post-processing calculations or self-consistent calculations [124]. In the post processing implementation, the tunneling current is calculated from the solution to the device equations at each bias step. Atlas then outputs the calculated tunneling currents to a log file. In the self-consistent implementation, the tunneling current is included directly in the current-continuity equations. Thus, it is part of the solution to the equations and gives accurate current continuity for the device, therefore, the terminal currents are self-consistent [124].

5.2.2.1.1   Direct Quantum Tunneling Model

The first type of direct tunneling available in silvaco assumes the material on the left hand side of the insulator (oxide) is polysilicon (Figure 5.4). Hole tunneling occurs when holes tunnel from one valence band to the other. If the bias applied to the contact is sufficiently large, then the situation illustrated in Figure 5.4 can occur. In this case, an electron in the silicon valence band tunnels through the insulator to the polysilicon conduction band. If the bias is reversed, then the opposite occurs in which an electron in the polysilicon valence band tunnels to the Silicon conduction band. Both of these cases are referred to as band-to band Tunneling. These should not be confused, however, with the other band-to-band tunneling models implemented in Atlas, which apply to regions of high electric field within a semiconductor [124].
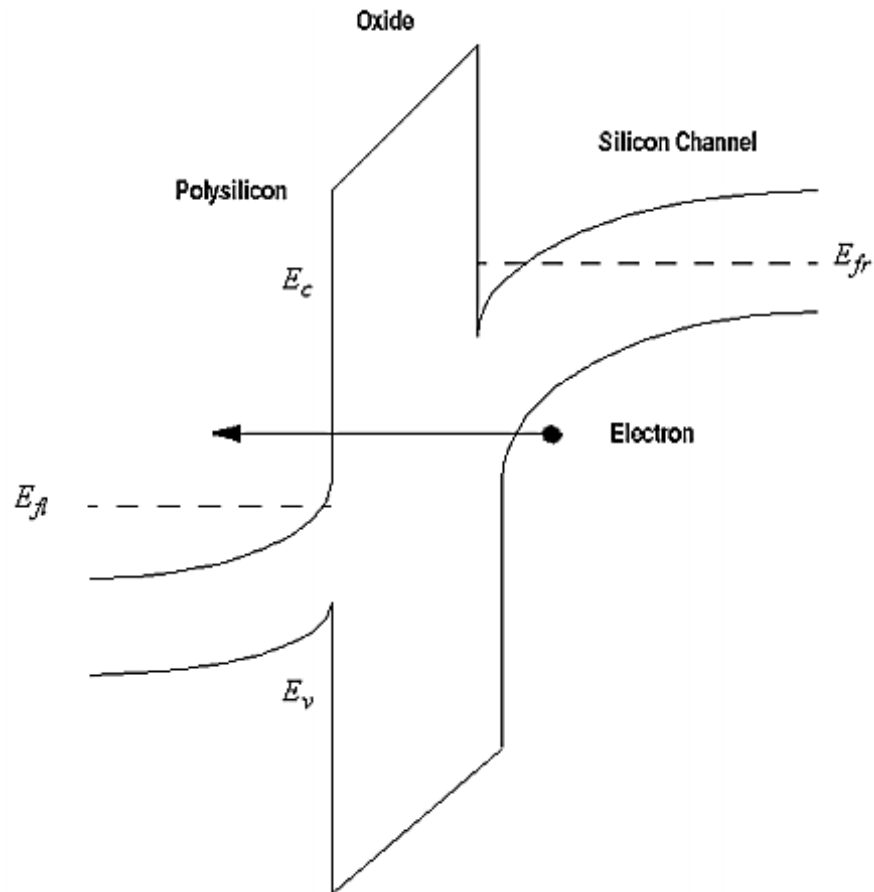
Figure 5.4: Schematic of band-to-band tunneling across a gate insulator with a polysilicon gate [124].

To enable the quantum tunneling model for electrons (holes), we specify `QTUNN.EL(QTUNN.HO)` in the `MODELS` statement. To enable Band-to-Band tunneling, we specify `QTUNN.BBT` in the `MODELS` statement. In order to enable all three options, we specify `QTUNN` in the `MODELS` statement.

```
models QTUNN.EL QTUNN.HO QTUNN.BBT
```

To enable the self-consistent versions of the quantum tunneling models, we specify the `QTNLSC.EL, QTNLSC.HO` and `QTNLSC.BBT` for electrons, holes and band-to-band tunneling options respectively.

```
Models QTNLSC.EL QTNLSC.HO QTNLSC.BBT
```

5.2.2.1.2   Non-local Quantum Barrier Tunneling Model (SIS)

To calculate the tunneling current between two semiconducting regions separated by a quantum barrier, we will be able to use the `SIS.EL` and `SIS.HO` models. The barrier layer may be either an insulator layer or a wide bandgap semiconductor. This model supposes that, the charge tunnels across the whole barrier, with the source/sink at the interface with the semiconductor regions. Tunneling current is evaluated for all energies at which tunneling is possible, up to the maximum of the band energy at the interface. The current in a range E_X to $E_X + dE$ is given by Eq.(5.4). The transmission probability, $T(E)$, is evaluated at each energy from a solution of the one-dimensional Schrodinger equation. To use the Wentzel-Kramers-Brillouin (WKB) approximation to solve the Schrodinger equation, we specify `TUN.WKB` on the `METHOD` statement. The `TUN.WKB` option will omit some quantum interference effects, but will result in a much quicker calculation. The tunneling current is then converted into a recombination or generation rate and inserted into the current continuity equation at each end of its tunneling path.To enable this model we specify `SIS.EL` for electron tunneling or `SIS.HO` for hole tunneling on the `MODELS` statement.

5.2.2.2 Fowler-Nordheim Tunneling (FNT)

The application of a high enough external electric field to the previous structure sufficiently leans the conduction and valence bands of the dielectric layer (Figure 5.5). This affects the oxide barrier width successively by decreasing, leaving the effective barrier relatively narrower. Therefore, the electrons of Fermi-level will face a triangular barrier in the oxide's conduction band, for $V_{ox} > \Phi_B$. As clarified in Figure 5.5, the effective barrier width gets narrower progressively (L, L', L''), since the barrier conduction band successively becomes steeper in response to the increasing applied electric field. Therefore, carriers will become easier to tunnel across the triangular barrier with a narrow effective width. This kind of tunneling mechanism is called "the Fowler-Nordheim tunneling" (FNT), and occurs in thicker oxides and desires higher electric fields, compared to direct tunneling (DT) [124, 128, 129].

Taking into consideration the WKB (Wentzel-Kramers-Brillouin) approximation, the Fowler-Nordheim tunneling model can be developed by solving the non-relativistic, time-independent, one-dimensional Schrödinger equation, for a triangular potential barrier [130]. The Fowler Nordheim Equation expresses the FN tunnel current density for electrons through the oxide as [126]:

$$J_{FN} = \frac{m_0 q^3}{8\pi h m_{\text{diel}} \Phi_B} E_{ox}^2 \exp\left[\frac{-8\pi\sqrt{(2m_{\text{diel}})\Phi_B}^{3/2}}{3hqE_{ox}}\right] \qquad 5.6$$

where E_{ox} is the magnitude of the electric field within the oxide, q the electron charge, m_0 the free electron mass, m_{diel} the effective electron mass in the insulator, h the Planck's constant, Φ_B the energy-barrier height (which is assumed to be independent of the electric field) [126].
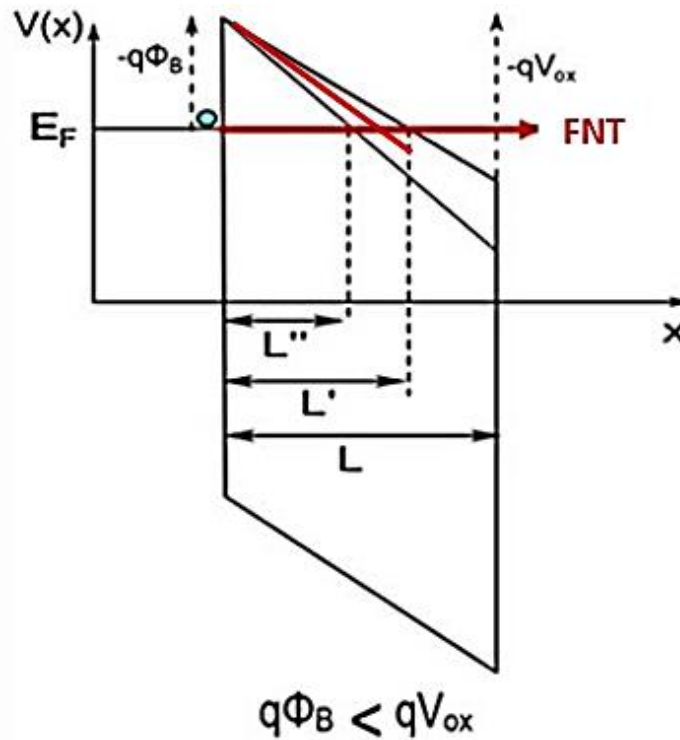
Figure 5.5: Band diagram illustrating how the FNT barrier becomes narrower when the electric field is increased. The barrier seen by the electron in the metal/insulator interface is triangular [122].

From Eq.5.6, one can easily see the strong oxide field dependency of the FN tunneling current, and hence higher oxide field would result in a larger FN tunneling current.

In silvaco Atlas, the Fowler-Nordheim model is implemented in two ways: the post processing or the self-consistent implementation. To enable the post processing version, we use the `MODELS` statement parameters `FNPP` for electron current and `FNHPP` for hole current. To enable the self-consistent solution, we use the `MODELS` statement parameters `FNORD` for electrons and `FNHOLES` for holes. Setting the parameter `FN.CUR` is the same as specifying `FNORD` and `FNHOLES` [124].

5.2.2.3 Thermionic/ Schottky Emission (SE)

Electrically charged particles are emitted from a conducting body heated to a sufficiently high temperature and can be drawn off by an external electric field. Depending on the emitter nature and the pertaining conditions, these emitted particles could be either electrons or ions. It is known as "thermions", and the process they are obtained through it is generally known as "thermionic emission". The Schottky or thermionic emission occurs when thermally-activated electrons are injected above the energy barrier into the oxide conduction band's as shown in Figure 5.6 [131]. It is one of the most observed conduction mechanisms in oxides, especially in relatively high temperatures. Taking MOS structure as an example, electrons are thermally emitted and traverse through the insulating layer in between two conducting electrodes [132].
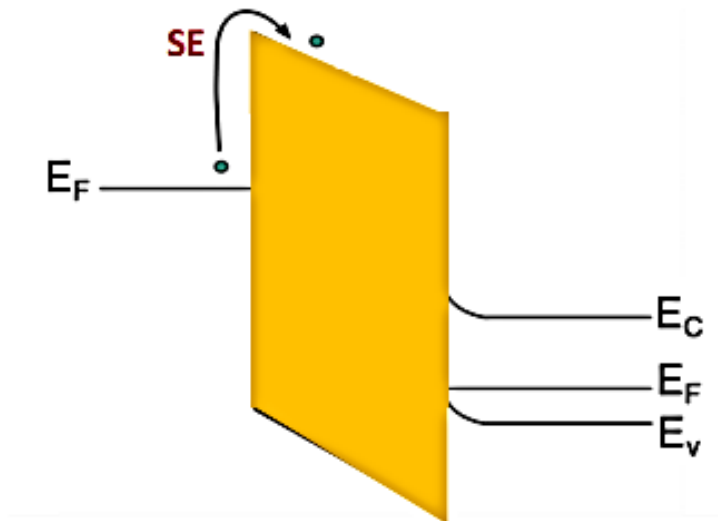
Figure 5.6: Schematic diagram illustrating a thermally excited electron jumping over an energy barrier, to the conduction band of the oxide, by means of thermionic emission.

With rising temperature, the thermal activation will enable electrons to overcome the energy barrier at the interface. Consequently, electrons jump directly from the electrode to the insulator conduction band, as shown in Figure 5.6. This type of electron transfer mechanism is what we called above thermionic/Schottky emission, and whose higher carrier energy than the potential barrier is a prerequisite to happen.

The current density J_{SE} can be related to electric field across the oxide (E_{ox}) and temperature (T) by the Schottky equation as shown in Eq.(5.7) [124, 131]:

$$J_{SE} = \frac{4\pi q m_{\text{diel}}(k_B T)^2}{h^3} \exp\left(\frac{-q\left(\Phi_B - \sqrt{qE_{ox}/4\pi\varepsilon_{ox}}\right)}{k_B T}\right) \qquad 5.7$$

where m_{diel} is the electron effective mass in the oxide, k_B is Boltzmann's constant, T is the absolute temperature in 0 K, h is Planck's constant, Φ_B is the junction barrier height and ε_{ox} is the permittivity of the oxide layer [124, 131].

According to Eq.(5.7), the Schottky emission current strongly depends on temperature . In addition, this temperature is associated with the energy of the carriers (i.e. higher temperatures will offer higher average energy to carriers).

To enable the thermionic transport model in Silvaco Atlas, we must specify `THERMIONIC` on the **interface** statement. We must also set the `S.S` parameter on the **interface** statement to indicate that the model applies to semiconductor-semiconductor interfaces.

5.2.3 Defect Mediated Tunneling (DMT)

Other transfer mechanisms consider the effects of defects/traps/interface states. One can know that oxide defects, trap sites or interface states could be induced during either the device fabrication processes or due to repeated high-field stress during electrical characterization [133, 134]. These induced traps or interface states can therefore act as mediators and assist the electron transport process in the oxide. This type of current transport mechanism in general can be referred as defect mediated tunneling (DMT) [122]. Poole-Frenkel tunneling and Trap assisted tunneling are included, and are addressed right below.

5.2.3.1 Poole-Frenkel Tunneling (PFT)

The existence of a high density of charged traps/impurities in the bulk of thin oxides is the precondition for Poole-Frenkel tunneling (PFT) to occur. However, these oxides must be thicker enough to suppress direct tunneling[1, 135]. During the Poole-Frenkel (PF) effect, the coulomb potential of charged impurities reduces the potential barrier height in an external field, due to which an enhanced emission rate occurs at low fields [135], and only occurs when there is a Coulomb interaction between the trap and the carrier.

The schematic energy band diagram of Poole-Frenkel (PF) tunneling is depicted in Figure 5.7 [122]. Electrons from the electrode's conduction band undergo direct tunneling and reach the first trap site in the localization of the interface, as indicated in Figure.5.7 (a). The injected electron will face a barrier of height Φ_B, which will be finally lowered by the Coulomb potential of charged impurities, which result from the applied external electric field (Figure 5.7 (b)). As a result, a thermally excited electron will afford to pass over the barrier (thermionic emission) and arrives at the next trap site. This "trap-detrap" process will repeat until the electron crosses the whole barrier.
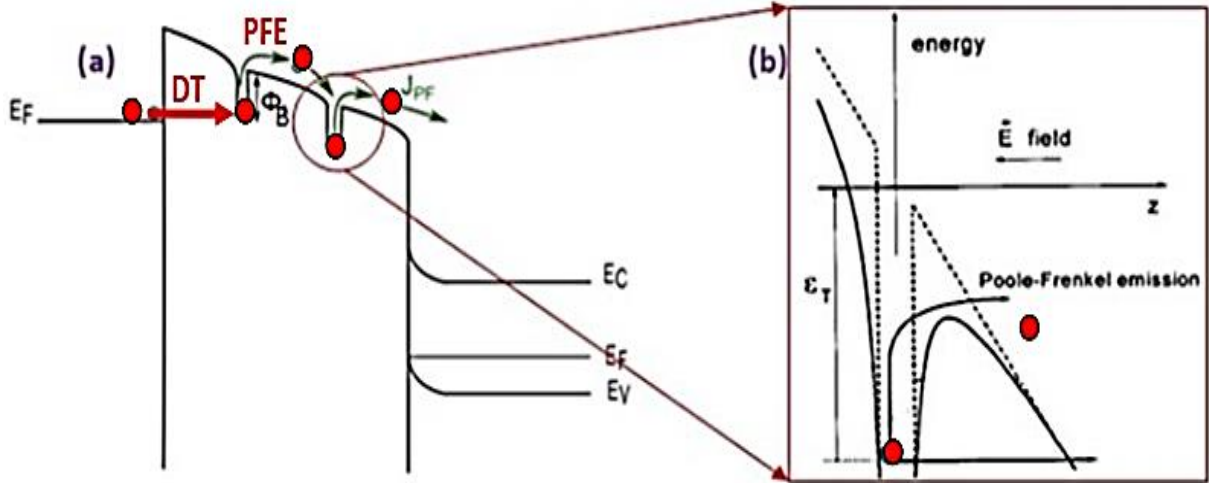
Figure 5.7: Energy band diagram showing: (a) Poole-Frenkel (PF) tunneling; and (b) barrier lowering by the columbic potential of impurity charges because of an applied external field in PF effect. The red arrow assuming that the interface-to-trap distance is very small[122].

The resulting current density J_{PF} can be expressed in Eq. (5.8) [122]:

$$J_{PF} = q\mu_n N_C E_{ox} \exp\left[\frac{-q\left(\phi_B - \sqrt{qE_{ox}/\pi\varepsilon_i\varepsilon_0}\right)}{k_B T}\right] \qquad 5.8$$

where k_B is Boltzmann's constant (in $eV/K°$), E_{ox} is the electric field across the dielectric (oxide), μ_n is the electronic drift mobility, ϕ_B is the trap depth from the conduction band, q is the electron charge, N_C is the density of states in the conduction band, ε_o is the permittivity of free space and ε_i is the relative dielectric constant [136]. One can infer that Pool Frenkel current density (J_{PF}) is dependent on the temperature and electric field. In addition, it is worth mentioning here that, during the Poole-Frenkel conduction, the energy that an electron needs to transfer from the localized trap to the conduction band decreases by increasing the electric field.

To enable this model in Silvaco tcad, we must specify `TRAP.COULOMBIC` in the `MODELS` statement, then, the Schockley-Read-Hall electron and hole recombination model will include the Poole-Frenkel effect.

5.2.3.2 Trap-Assisted Tunneling (TAT)

As the name indicates, Trap-assisted tunneling (TAT) is the transport mechanism in which electrons (holes) are assisted by defects/traps in the oxide to be transported through this layer to the conduction band of the electrode. At high electric fields, tunneling of electrons from the

valence band to the conduction band through trap or defect states can have an important effect on the current. TAT process can be of many kinds depending on: the nature of traps, density, and depth of traps from the conduction band; as well as on the conservation of energy of electrons during the process. Number of these varieties could be: "elastic or inelastic trap assisted tunneling", "single trap or multi-trap assisted tunneling", and "shallow-trap or deep trap assisted tunneling". The existence of defects within the oxide would divide the traverse length into two or more parts that make electrons feel like they progressively face thinner barriers at a time. The TAT process can be either elastic, in which the carrier energy is conserved, or inelastic, where the carrier loses energy due to the phonons emission [128].

As shown in Figure. 5.8 (a), the tunneling electron in the elastic mechanism does not lose energy during the whole transport. In this case, the total elastic tunneling rate is defined by the overlap between the left (occupied state) side and the right (unoccupied state) side. In the inelastic case, the tunneling of electrons can excite an electromagnetic oscillator (light or Surface plasmon polaritons (SPPs)) and lose energy corresponding to the energy difference between the two electronic states, as shown in Figure. 5.8 (b).
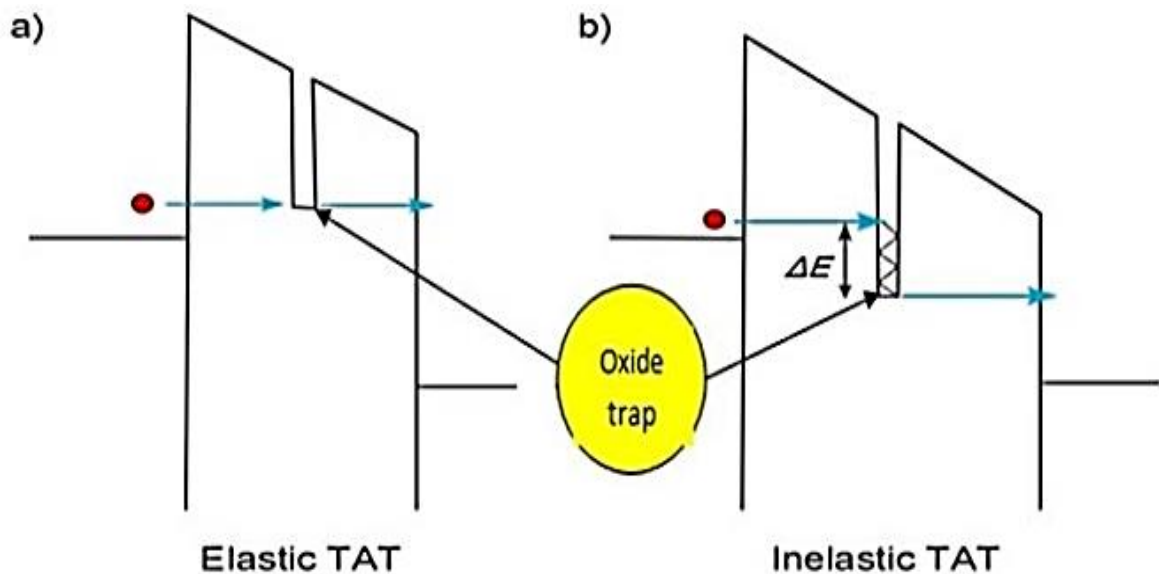
Figure 5.8: a) Elastic TAT (without energy loss) and b) inelastic TAT (with losing energy ΔE) [122].

For very thin oxides, only a single-trap could be considered to model the TAT current. For thicker oxides however, one-trap may not be good enough to produce tunneling current and hence multi trap model shall be used [137]. This is due to the fact that, presence of several traps in the oxide would generate a way in the barrier, for electrons to tunnel through [120].

5.2.3.2.1 Model Overview

Multiple models have been submitted to describe trap-assisted tunneling in the gate dielectric of MOS devices. These models commonly share the equation for the current density, which is given by integration along the gate dielectric[138].

$$J = q \int_0^{t_{\text{dicl}}} \frac{N_{\text{T}}(x)}{\tau_{\text{c}}(x) + \tau_{\text{e}}(x)} dx \qquad 5.9$$

where N_{T} denotes the trap concentration, τ_{c} and τ_{e} denote the capture and emission times of the considered trap respectively.

Because both capture and emission processes must occur in succession, they both define the current density. However, there are differences in how to calculate the capture and emission times. Some of the models utilize constant capture and emission cross-sections to calculate the respective times. Another important mark is the distribution in space, where the traps are usually assumed to follow a Gaussian distribution. Moreover, the distribution of energy is crucial. Commonly, it is assumed either that traps have a Gaussian distribution in energy or that they are located at a certain energy level below the dielectric conduction band [128].

5.2.3.2.2 Chang's Model

A commonly used model is the generalized trap-assisted tunneling model presented by Chang   et al [139, 140]. The current density reads as

$$J = q \int_0^{t_{\text{diel}}} A N_{\text{T}}(x) \frac{P_1(x) P_2(x)}{P_1(x) + P_2(x)} dx \qquad 5.10$$

where A is a fitting constant, $N_{\text{T}}(x)$ is the spatial trap concentration, P_1 and P_2 are the transmission coefficients of electrons captured and emitted by traps.

5.2.3.2.3 lelmini's Model

Considerable research has been done by Ielmini et al.[141]. To describe the inelastic trap assisted tunneling (ITAT), taking into account the hopping conduction. The model derives the trap-assisted current by the integration along the dielectric thickness and energy.

$$J = \int_0^{t_{\text{dicl}}} dx \int_{\varepsilon_{min}}^{\varepsilon_{max}} \tilde{J}(\varepsilon_{\text{T}}, x) d\varepsilon \qquad 5.11$$

J is the net current flowing through the dielectric, given as the difference between capture and emission currents through either side of the dielectric as expressed in Eq. (5.12).

$$J(\mathcal{E}_T, x) = J_{cl} - J_{el} = J_{er} - J_{cr} = qN_T'W_c\left(1 - \frac{f_T(\mathcal{E}_T, x)}{f_l(\mathcal{E}_T, x)}\right) \qquad 5.12$$

Where f_T is the trap occupancy, $\mathcal{E}_T$ is the trap energy, W_c the capture rate, and f_l the energy distribution function at the left interface. The symbol N_T' denotes the trap concentration in space and energy.

Otherwise, Ielmini developed the model to include transient effects, and notes that in this case, the net difference between current from the left and right interfaces equals the change in the trap occupancy multiplied by the trap charge [128, 141].

$$(J_{cl} - J_{el}) + (J_{cr} - J_{er}) = qN_T\frac{\partial f_T}{\partial t} \qquad 5.13$$

Where J_{cl} and J_{cr} are the conduction current due to electrons coming from the left and right sides respectively,

According to trap assisted tunnelling mechanism (tunneling through deep level defects), the indirect current, through the SiO_2 layer, is calculated taking into account the capture/emission from/to Si, and the capture/emission from/to poly- Si for a trap with a discrete energy level $E_t(x)$ and a density with spatial distribution $N_t(x)$, where x is its spatial position within the SiO_2 layer[141, 142]. Applying this relationship on electrons, the current from the left- and right-hand sides into traps can be written as [124] :

$$J_L(x) = qN_tb_L(E_t, E_{Fl}, x)\left[f_L(E_t, E_{fl}, x) - f_t(E_t, x)\right]\Delta x \qquad 5.14$$

$$J_R(x) = qN_tb_R(E_t, E_{Fr}, x)\left[f_R(E_t, E_{Fr}, x) - f_t(E_t, x)\right]\Delta x \qquad 5.15$$

where, f_L, f_R are the probabilities of electrons being at energy E_t at the left and right edges of the oxide respectively, E_{Fl} and E_{Fr} are the statistical factors at the left- and right-hand side quasi-Fermi level, f_t is the probability of the trap being occupied by an electron and b_L and b_R are the effective capture rates left and right of the quantum barrier respectively:

$$b_L = \frac{4.\pi.m^*.k_BT.\sigma}{h^3.f_L(E_t, E_{Fl}, x)}\int_{E_{min}}^{E_{max}} log\left(1 + exp\left[\frac{-(E - E_{Fl})}{k_BT}\right]\right)W(E, x)dE \qquad 5.16$$

$$\qquad 5.17$$

$$b_R = \frac{4.\pi.m^*.k_BT.\sigma}{h^3.f_R(E_t, E_{Fr}, x)} \int_{E_{min}}^{E_{max}} log\left(1 + exp\left[\frac{-(E - E_{Fr})}{k_BT}\right]\right) W(E, L - x)dE$$

where σ is the trap cross-section, m^* is the effective mass, k_B and h are Boltzmann's and Planck's constants respectively, T is the device temperature and $W(E, x)$ is the tunneling probability factor at point x. $W(E, L - x)$ is the tunneling probability factor from position L to position x. E_{min} in the evaluation of b_L is the maximum of either the trap energy at position x or the electron energy at the left-hand side of the oxide and E_{max} is the greater of the conduction band energy at position x or the conduction band energy at the left hand side of the oxide. Finally, the total trap assisted tunneling current is evaluated by summing the currents for all positions:

$$J_{ITAT} = \sum_i J_R(x_i) = -\sum_i J_L(x_i)$$

5.18

Thus, the total trap-assisted tunneling current is evaluated by using the value of the steady state trap occupancy at each position ($f_t(E_t, x)$), and summing the contributions from each length Δ_x at position x_i where the sum is across the oxide thickness. More details on these equations resolution and Physical phenomena are given in Ref [124, 143]

To activate the self-consistently ITAT model in Silvaco Atlas, we must specify ITAT.SC.EL on the MODELS statement for electron current, ITAT.SC.HO for hole current, or RTAT.SC for both electron and hole current with recombination. While, in order to activate the post-processing option, we must specify ITAT.PP.EL on the MODELS statement for electron current, ITAT.PP.HO for hole current, or RTAT.PP for electron and hole current, where the trap can act as a recombination center [124].

For example:

```
MODELS    ITAT.SC.EL    ITAT.SC.HO

MODELS    ITAT.PP.EL    ITAT.PP.HO
```

5.3 SILVACO TCAD Simulation

SILVACO TCAD software is the abbreviation of Silicon Valley Corporation Technology Computer-Aided Design. It is a simulation package process of semiconductor devices that contains lots of physically based simulators (ATHENA, ATLAS, MERCURY, SSUPREM3, etc.) grouped under one environment called DECK BUILD. Each of them has the role of simulating different processes. Among many of SILVACOs modules, ATLAS is the most suitable module to be used in this work. Atlas is a physically based two and three-dimensional device simulator. It predicts

the electrical behavior of specified semiconductor structures and provides insight into the internal physical mechanisms associated with the device operation. The obtained results are plotted and analyzed by a special tool named TONYPLOT. TONYPLOT is a conception tool that plots the obtained results during the simulation process. Moreover, it provides scientific visualization capabilities including XY plots with linear and logarithmic axes, polar plots, surface and contour plots [124].

5.3.1 Structure specification
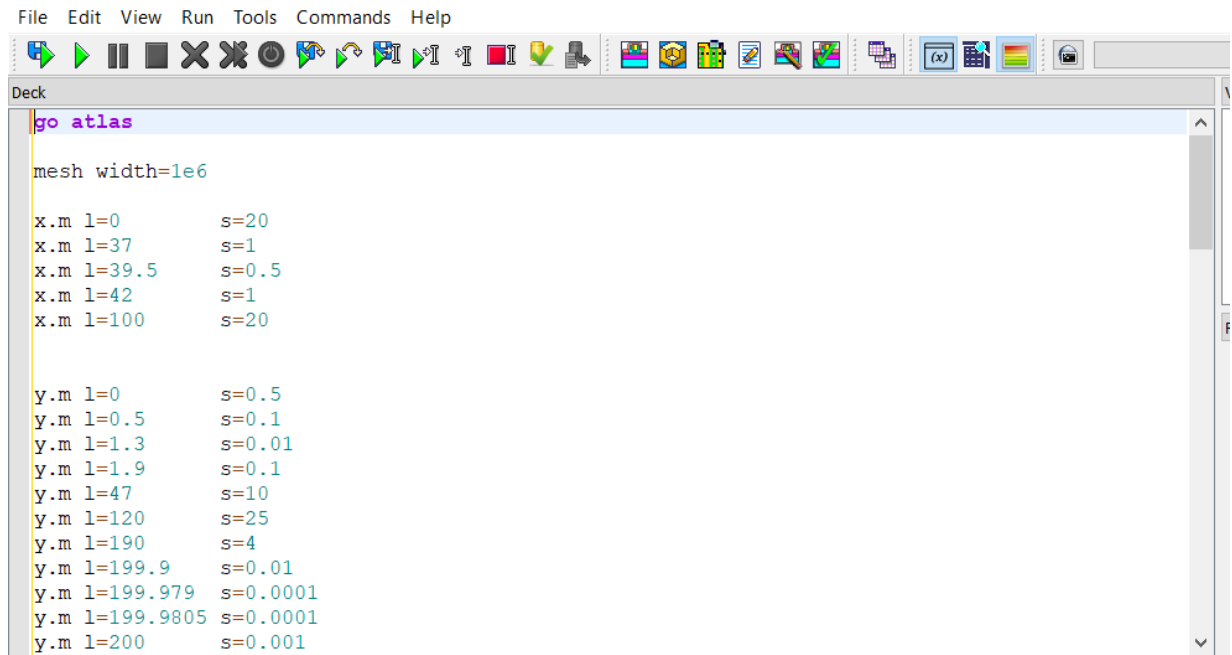
It is the first step in the Atlas commands file to define the simulated structure. It contains four statements arranged as follows:

- Mesh
- Region
- Electrodes
- Doping

To run on Atlas inside DECK BUILD, one must start with the command:

go atlas

The next step is defining the mesh. A mesh indicates a collection of elements whose union defines the device (see Figures5.9 and 5.10). It is built by overlapping two sets of parallel and perpendicular lines to each other to form a network that has the device shape. To define the mesh, three important pieces of information must be defined: lines direction (line x or y), the principle lines locations of (l) then the steps between them (s) which explain the distance between secondary lines in micrometer (Figure 5.9).

Figure 5.9: Mesh generation.

After that, we define the used material types. That is done with REGION statements:

```
region num=1 silicon     x.min=0  x.max=100  y.min=0          y.max=199.979

region num=2 material=sio2 x.min=0 x.max=100 y.min=199.979  y.max=199.9805

region num=3 polysilicon x.min=0  x.max=100  y.min=199.9805  y.max=200
```

The "`material`" or "`mat`" statement specifies the material composition. The `x.min`, `x.max`, `y.min` and `y.max` parameters are to specify the location, extent of the region and its geometry, in unit of microns.

The next step is the electrodes statement. Electrodes are specified using the `ELECTRODE` statement. `ELECTRODE` specifies the locations and names of electrodes in a previously defined mesh. `ELECTRODE` should be an n-digit integer, where each of the digits is a separate electrode number.

```
elec num=1 name=anode   x.min=37 x.max=42
elec num=2 name=cathode x.min=0 x.max=100 y.min=200 y.max=202   mat=Aluminum
```
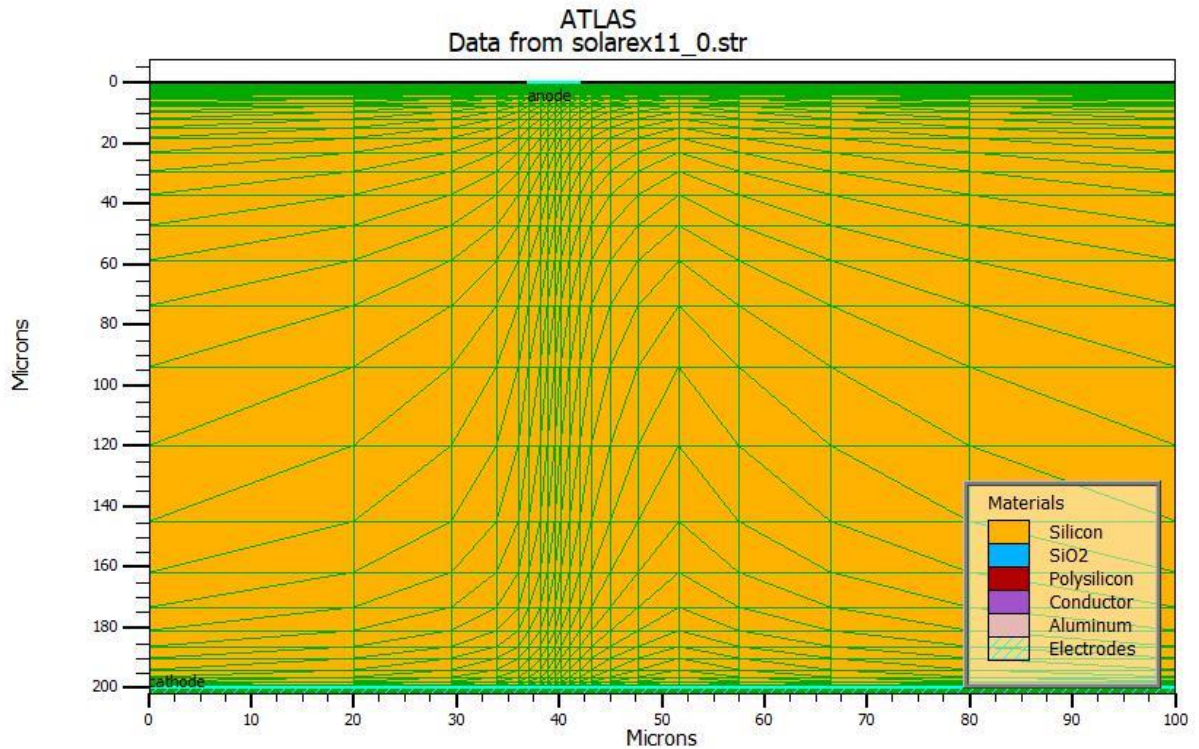
Figure 5.10: Mesh and structure generation.

The `DOPING` statement is used to define doping profiles in the device structure. Each building has a `DOPING` statement different from the others.

```
doping uniform p.type conc=1e19  y.min=0        y.max=1.3
doping uniform n.type conc=5e16  y.min=1.3      y.max=199.979
doping uniform n.type conc=1e20  y.min=199.9805  y.max=200
```

5.3.2   Models specification

To obtain simulation results close to the realistic ones, we must take into consideration lots of complex dependencies of the device properties. ATLAS provides independent models to describe every device property dependency individually, so they can be activated separately. The accuracy of the obtained results depends on the physical models used during the simulation process.

Physical models are specified using the "`models`" statement. An example of it:

```
models sis.el sis.nlderivs ust auger bgn conmob temp=300 print
```

where: (`sis.el sis.nlderivs ust auger bgn conmob`) enable the specific models. The "`temp`" parameter specifies the general temperature of the structure in Kelvin, and the "`print`" command prints in the output window of DECKBUILD the basic information used in the simulation; such

as the status of all models (which models are activated and which are not), basic constants, coefficients used in every model.

5.3.3 Numerical method selection

The electrical properties of the device are modeled using numerical solutions of fundamental partial differential equations that link the electrostatic potential with the carrier densities. ATLAS provides various numerical methods to calculate the solutions to semiconductor device problems. The main types of these numerical methods are [124]:

The first method is the GUMMEL type, which is useful where the system of equations is weakly coupled but has only linear convergence. The second method is NEWTON, which is useful when the system of equations is strongly coupled and has quadratic convergence. The final method is the BLOCK method, which can provide faster simulation times in situations where the NEWTON method struggles. BLOCK iterations involve solving subgroups of equations in various sequences.

Numerical method is enabled in the METHOD statement as:

```
method GUMMEL NEWTON
```

5.3.4 Solution specification

Atlas can calculate DC, AC small signal, and transient solutions. Getting solutions is similar to setting up parametric test equipment for device tests. One generally defines the voltages on each of the device electrodes. Atlas then calculates the current through each electrode. It also calculates internal quantities, such as carrier concentrations and electric fields throughout the device, which is a difficult or impossible quantity to measure. During all simulations, the device starts with zero bias on all electrodes. Solutions are obtained by stepping the biases on electrodes from this initial equilibrium condition. The saving results process is done using the `SAVE` statements [124].

The terminal characteristics calculated by Atlas will be stored in Log files. These characteristics are current and voltages for each electrode in DC simulations. For example, the statement:

```
LOG OUTFILE=solar.log
```

To obtain convergence for the used equations, we supply a good initial guess for the variables to be evaluated at each bias point. Atlas uses this initial guess and iterates to a converged solution. When no previous solutions exist, the initial guess for potential and carrier concentrations must be made from the doping profile. This is why the initial solution performed must be the zero bias (or thermal equilibrium) case. It is specified by the statement:

```
Solve init
```

Since, we are simulating a solar cell, there must be light for the process to take place. The illumination turns on by assigning the beam intensity on a SOLVE statement as follows:

```
beam num=1 AM1.5 x.origin=40 y.origin=-1.0 angle=90.0 reflect=1/
wavel.start=0.3  wavel.end=1.2 wavel.num=120
```

```
solve b1=1
```

Solution and structure files provide an image of the device at a particular bias point. This gives us the ability to view any evaluated quantity within the device structure. The SAVE statement enters all node point information into an output file. The following is an example of the "save" statement:

```
save outfile=solar.str
```

```
save outfile=solar.log
```

5.3.5   Results analysis

Once the solution has been found and saved in files, the information can be extracted as numerical values and displayed graphically.

The EXTRACT command allows extracting device parameters as numerical values. It operates on the previous solved curve or structure file. By default, EXTRACT uses the currently open log file. The next statement is an example of extract command.

```
extract  name="Jsc"  y.val  from  curve(v."anode",  i."anode")  where
x.val=0.0
```

The last step is to sketch the saved files. The process is doing using the "tonyplot" command. The following is example to draw the structure file.

```
tonyplot solar.str
```

6. *Chapter 6: Results and discussion*

6.1 Introduction

Crystalline silicon solar cells have been dominating the photovoltaic market. Since PV technology became an applicable renewable energy source due to the highly-developed manufacturing technology with low manufacturing cost, abundant environmentally friendly raw materials, and high-level market acceptance. With the advancing manufacturing technology, solar cell efficiency has been increased steadily lately, especially with some innovative cell structures introduced to reduce the recombination losses of solar cells. Moreover, and contrary to the harmful role of defects, some recent suggestions have claimed that they might be very beneficial [9]. It mentioned the possibility of suppressing the carrier recombination by introducing deep-level defects [9].

Starting from the crystalline silicon (c-Si) wafer as a base layer, numerous solar cells designs have been studied, which use different passivating layers as well as have different geometrical structures. That is what we will do in this chapter. We will start with the study of a p-n single junction device based on c-Si. Then, we will investigate the BSF structure in which an n^+ polysilicon, as a back-surface field (BSF) layer, will be introduced between the back contact and the n- type silicon layer to get the p-n-n^+ structure. Thereafter, the tunnel oxide passivated contact (TOPCon) structure will be studied. This latter includes a wide bandgap (nitride or oxide) passivation layer (PL); which is inserted between the n-Si layer and the n^+ polysilicon and metal contact on the entire back side of n-type Si cell. The BSF and the tunneling layers influence on the p-n structure will be discussed in detail. After that, and by taking a suitable thickness of the tunneling layer, we will study the influence of deep level defects, presented in the passivation layer, on the solar cell performance. The deep defects effect includes : the energy level position, the defects density , the defective tunneling layer thickness and the capture cross-section. A similar study is carried out on p-type Si-based TOPCon solar cell with n-p-p^+ structure, in which carrier transport and tunneling process are mainly achieved by holes. The simulation is carried out using the two-dimensional (2D) SILVACO-ATLAS module, and by considering the AM1.5G solar spectrum at ambient temperature (T=300 °K).

6.2 Effect of a Back-Surface Field and Passivation Layer on a Silicon Schottky Solar Cell

6.2.1 Device structure

The structure of the simulated solar cell in this work is illustrated in Figure 6.1. It is a 2D p–n single junction device. The emitter is made of p-type monocrystalline silicon (c-Si) while the base is phosphorus-doped monocrystalline silicon. The anode (front contact) is an ohmic contact while the back contact is either an ohmic or a Schottky contact. All the simulation operations are carried out under the AMG1.5 solar spectrum with an incident power density of 100 mW/cm^2 at room temperature (T=300 K). The input simulation parameters of the studied solar cell are listed in Table 6.1 [124], [144].
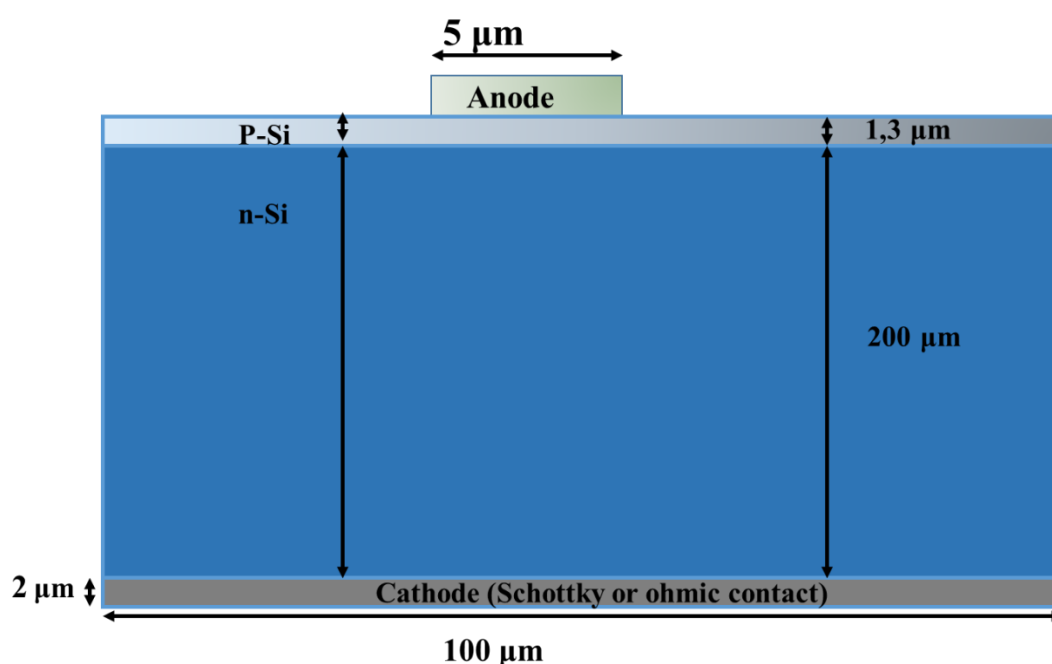
Figure 6.1: Schematic view of the simulated solar cell.

Table 6-1 : The solar cell input parameters [124], [144].

Parameter	Term	Si
d (µm)	Thickness (total)	203.3
Eg (eV)	Bandgap	1.08
χ (eV)	Affinity	4.17
ε_r	Permittivity	11.8
N_c (cm^{-3})	Effective density of states at CB	2.8×10^{19}
N_v (cm^{-3})	Effective density of states at VB	1.04×10^{19}
μ_n (cm^2/v s)	Electrons mobility	1000
μ_p (cm^2/v s)	Hole mobility	500
N_a (cm^{-3})	Density of p type doping	10^{19}
N_d (cm^{-3})	Density of n type doping	5×10^{16}

6.2.2   Schottky and Ohmic Contact effects

Aluminum (Al) is used as a back contact in such structures due to its abundance and it is a benign impurity in silicon [145]. To know which contact can improve the solar cell, two different contacts (Schottky and ohmic types) were modeled to evaluate their effect on solar cell performance. The modification is applied to the Al work function based on literature [144] .

The Schottky barrier (or Schottky contact) is a metal/semiconductor junction where the metal work function (ϕ_m) is greater than the semiconductor electron affinity (χ_{SC}). In contact, these two materials form a fixed energy barrier of constant height but varying width.

As we said above, the Al back-contact work function (ϕ_m) is higher than the silicon electron affinity (χ_{SC}) for the Schottky contact simulation case. The condition is inversed ($\phi_m < \chi_{SC}$) while simulating the ohmic contact case. The energy band diagrams corresponding to the two cases (ohmic and Schottky contacts) are shown in Figure 6.2.
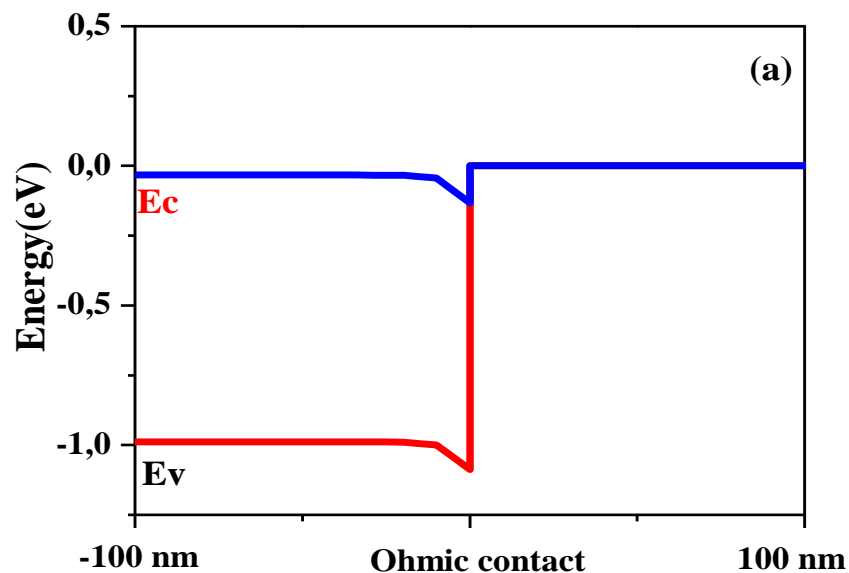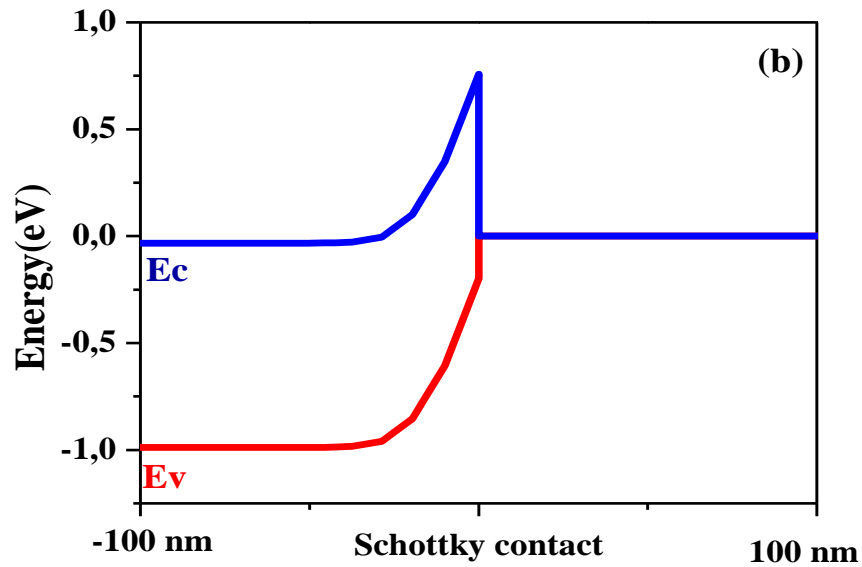
Figure 6.2: Band bending diagram at the Silicon/metal back interface in the case of: (a) Ohmic, and (b) Schottky contact.

The obtained current density-voltage $(J - V)$ characteristic of both contacts is shown in Figure 6.3 and the electrical output parameters extracted are inserted in Table 6.2. With the silicon electron affinity $\chi_{SC} = 4.17\ eV$, the Schottky contact case corresponds to $\phi_m = 4.99\ eV$, for ohmic contact $\phi_m = 4.1\ eV$ [144].
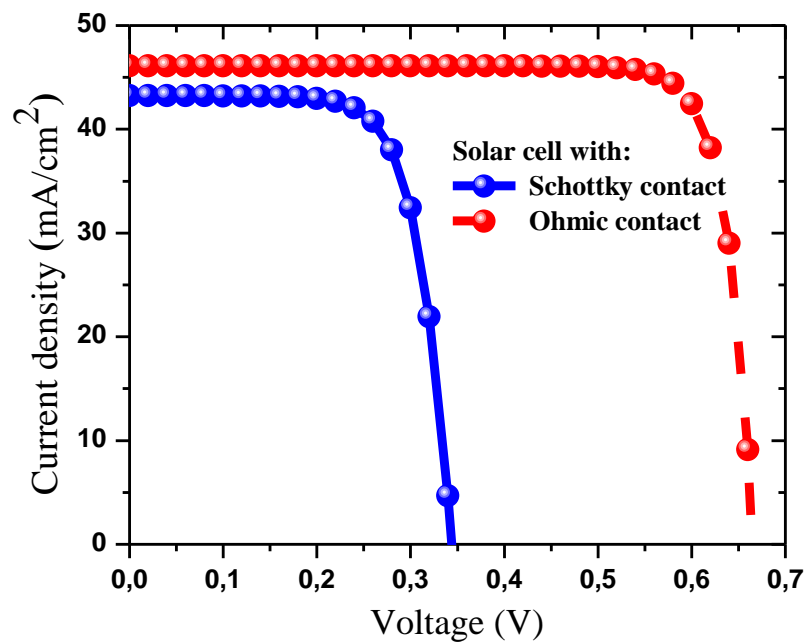
Figure 6.3: The current density–voltage $(J–V)$ curves of Schottky and Ohmic contacts based simple solar cells.

Table 6-2: Effect of contact types on the output parameters.

Contact	ϕ_m (eV)	J_{sc} (A/cm^2)	V_{oc} (V)	FF (%)	η (%)
Schottky	4.99	43	0.34	71.53	10.63
Ohmic	4.1	44	0.64	83.73	23.63

As shown in Figure 6.3 and Table 6.2, the Schottky-based solar cell shows an inferior performance compared to its ohmic-based counterpart, the efficiencies are 10.63 and 23.63% respectively. This is because the current goes through the Schottky contact and encounters a barrier and a larger depletion layer. While in the case of ohmic contact, electrons can pass freely to the other side. This result serves as an important step toward understanding the BSF layer in Schottky-based solar cells.

6.2.3   Field-Effect Passivation Due to BSF

To generate the field-effect passivation, a back-surface field (BSF) layer of n$^+$ polysilicon is added to the backside of the p–n single junction to give the p-n-n$^+$ structure. The BSF layer is thin (~20 nm) and usually heavily doped, then it will include a neglected part of the depletion region established at the n–n$^+$ space charge region [146]. Because of the abrupt change in the doping concentration level (N_D) at the n–n$^+$ interface, a voltage builds up (Eq.(6.1)), and a high electric field (BSF) is generated. The latter has the same direction of the electric field established at the frontal p–n junction [146].

$$V_b = \frac{kT}{q} \ln\left(\frac{N_D^+}{N_D}\right) \qquad\qquad 6.1$$

Due to the diffusion gradient caused by high dopant concentration, the back surface field accelerates the minority carriers in the n-type region (holes in this case) toward the front side of the cell (p-type region) [124]. In other words, the BSF layer can help block minority carrier holes from diffusing to the bottom and back-contact layer of the solar cell, and thus is helpful to reduce the bottom surface recombination [147].

For that reason, a BSF layer is included now to get, as we said above, the pnn$^+$ structure. The BSF layer effect on the solar cell performance is investigated by changing the BSF doping concentration from 5×10^{16} to 1×10^{20} cm^{-3}. The corresponding current density-voltage ($J - V$) characteristics of both Schottky and Ohmic contact samples are shown in Figure 6.4.

According to the obtained results (Figure 6.4), only the $J - V$ characteristics of the Schottky sample are affected. Figure 6.4 shows the doping concentration effect of the n^+ layer on the solar cell Figures

of merit for the cases of Schottky and Ohmic contact samples. It can be seen that all parameters increase with increasing doping density of the n^+ layer for the Schottky contact but not in the case of the Ohmic sample.
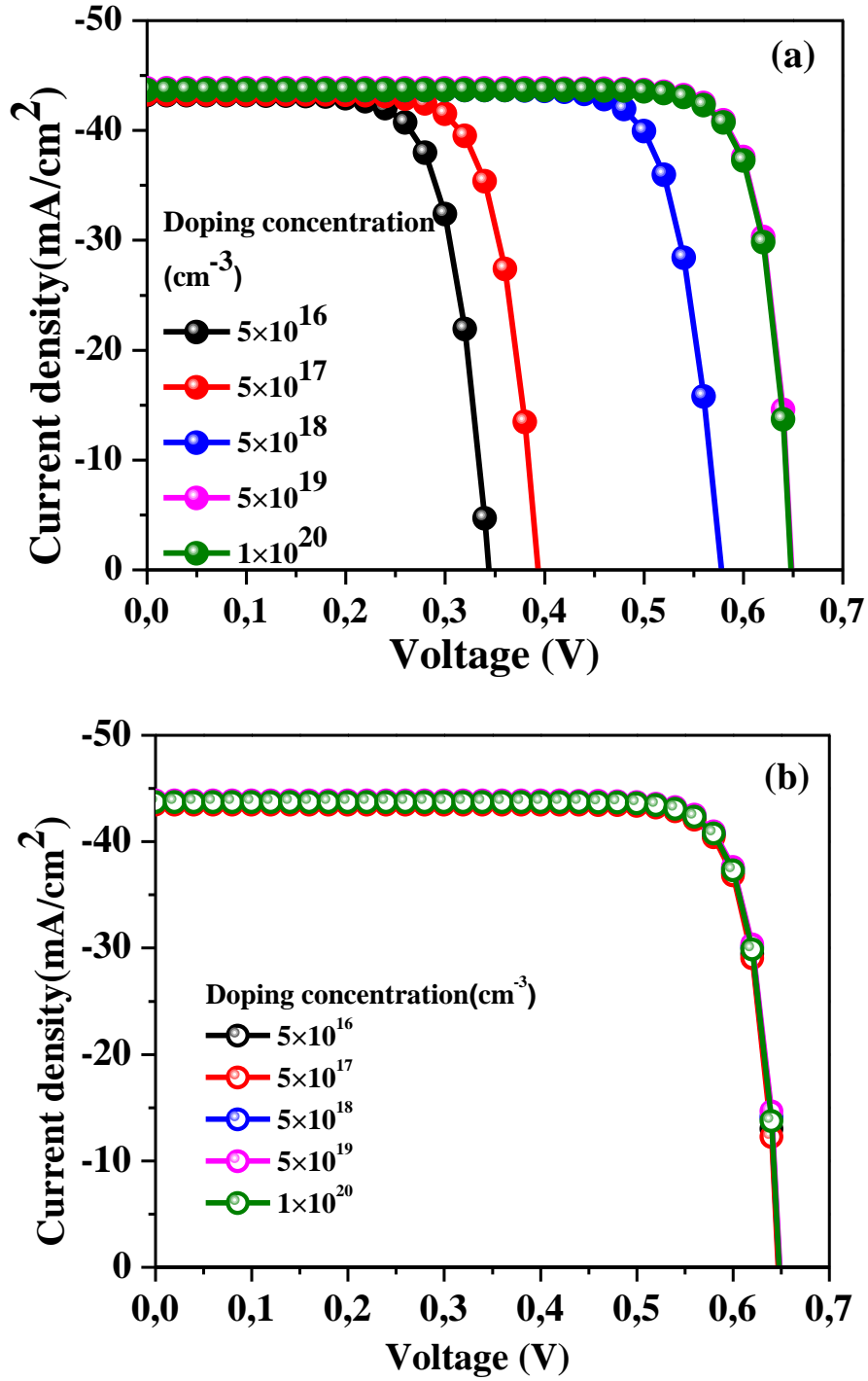
Figure 6.4: BSF doping concentration effect on the $(J - V)$ characteristic of c-Si based pnn$^+$ solar cell with : a) Schottky contact , b) Ohmic contact.
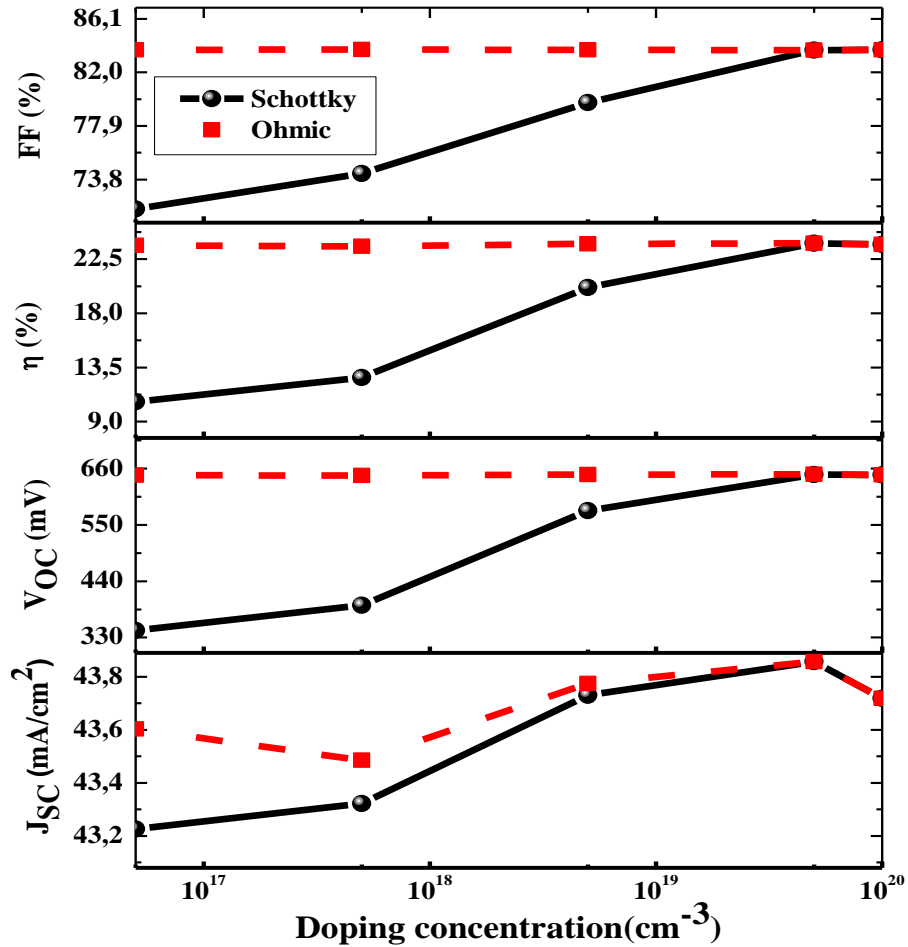
Figure 6.5: BSF doping concentration effect on the output parameters of the c-Si based pnn+ solar cell with Schottky and Ohmic contacts.

The improvement in the Schottky contact based solar cell is probably due to the enhanced tunneling through the heavily doped layer that provides a large number of electrons and reduces the depletion region thickness as shown in Figure 6.6. Thus, reducing the number of holes, and reducing the recombination, which increases the conversion efficiency from 10.63 % with doping of 5×10^{16}cm$^-$^{3} to 23.7 % with doping of $10^{20} cm^{-3}$.

Indeed, in the Schottky contact case, the Fermi level alignment (dashed lines in figure 6.6) induces the silicon conduction band to bend upwards. Therefore, the electrons move out from the silicon side to the metal one facing a Schottky barrier. By increasing the doping concentration of the BSF layer, the created electron barrier at the n/n+ interface decreases which makes electrons pass freely. At the same time, the hole barrier increases by increasing the BSF doping concentration which reduces the hole current. In the ohmic contact case, however, the conduction and valence bands are bending downward because of the Fermi level alignment (as illustrated in Figure 6.7). Therefore,

the electrons this time move freely from the semiconductor side to the metal side independently of the n$^+$ doping concentration; which gives a negligible effect on the silicon cell output parameters.
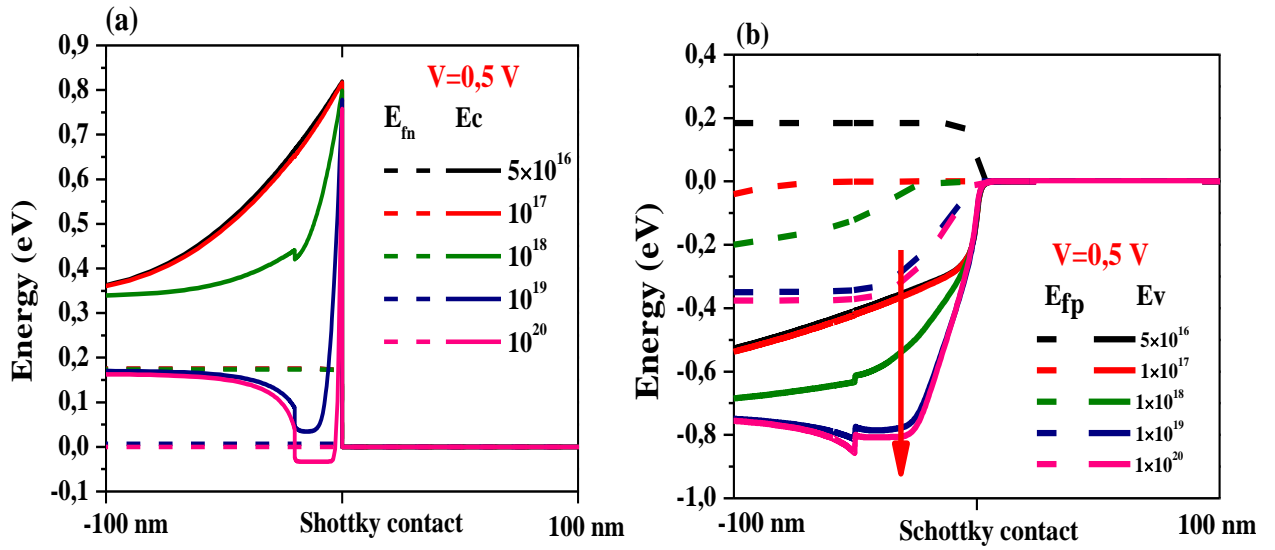
Figure 6.6 : BSF doping concentration (cm^{-3}) effect on the conduction and valence band bending near the Schottky contact for a forward bias of V=0.5 V.
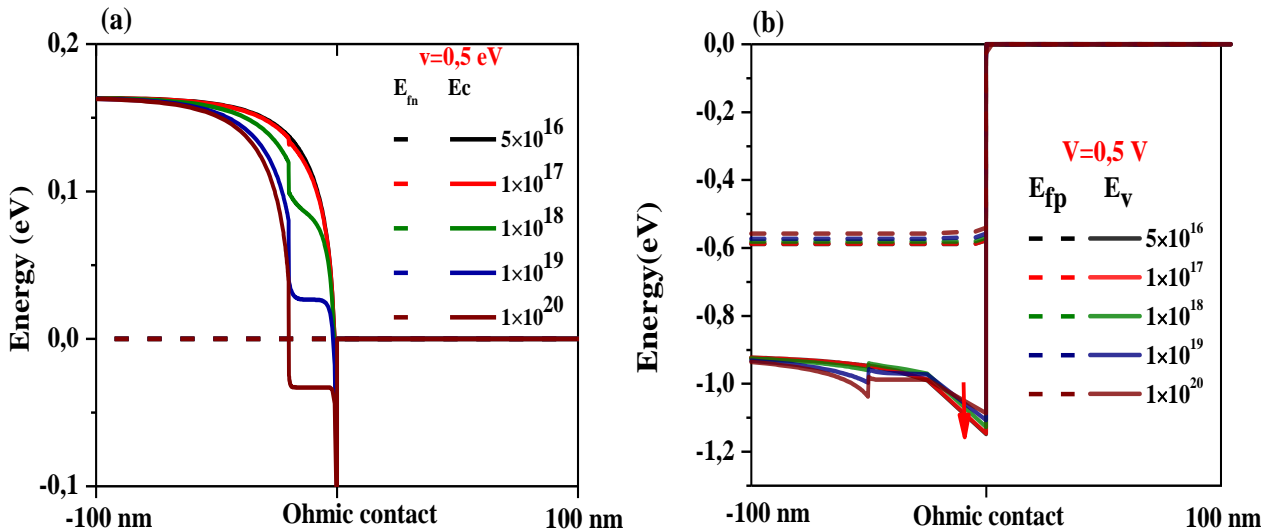
Figure 6.7 : BSF doping concentration (cm^{-3}) effect on the band bending near the Ohmic contact for a forward bias of V=0.5 V.

6.2.4   Effect of the tunneling layer

Defects on the front and back surface of silicon (Si)–based solar cells can be passivated by depositing an additional layer of silicon oxide (SiO_x) or silicon nitride (SiN_x) [34, 148]. Therefore, tunneling contact passivation using Al_2O_3 [34, 149]and SiO_2 [150] is considered as one of the best solutions to give high efficiencies of Si-based solar cells [151] due to its excellent passivation

quality that reduces the surface recombination velocity in Si-oxide. Thus, it was shown that the tunnel oxide is a vital element of this contact [152], where it reduces minority carriers recombination and simultaneously does not hamper majority carriers flow [148, 153]. This process occurs since a potential barrier is formed in the valence and conduction bands of the Si semiconductor. The barrier prevents the passage of minority carriers while majority carriers pass through the tunneling effect. Thus, it increases the majority carrier concentration near the contact, and decreases minority carrier concentration; which reduces recombination in the heavily doped region of the solar cell [152].

The first tunneling layer used in this work, a passivation layer (PL), is from SiO_2 . This latter is inserted between the n-Si layer and the n$^+$ polysilicon (with the doping of $10^{20} cm^{-3}$) and the metal contact on the entire backside of the n-type Si cell. The generated structure and mesh of the solar cell taken by Atlas from Silvaco are presented in Figure 6.8.
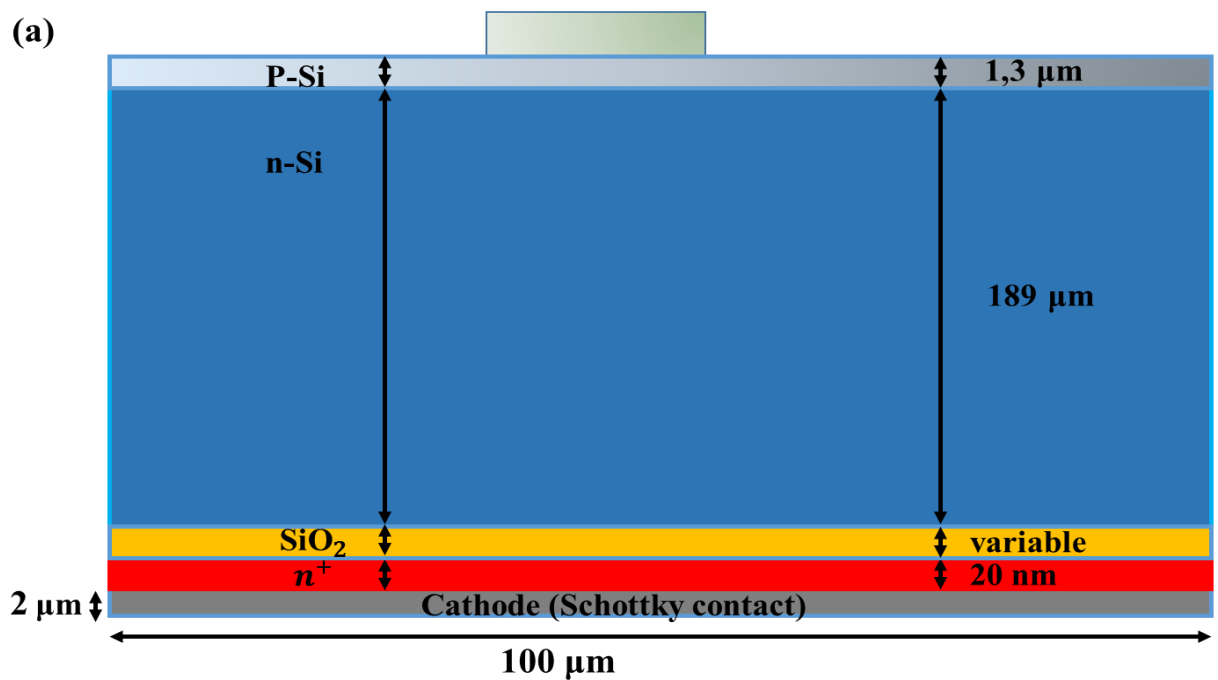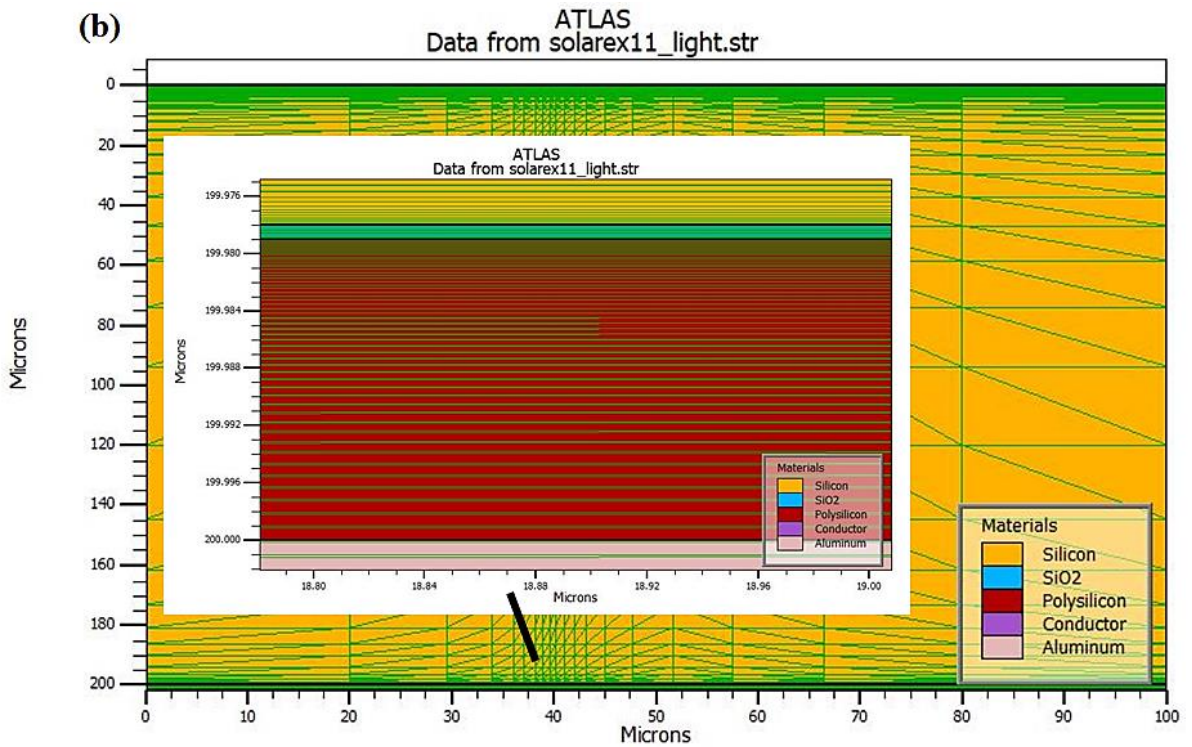
Figure 6.8: (a): Schematic view of n-type silicon-based solar cell including SiO_2 passivation layer and **(b):** its mesh taken from Silvaco Atlas.

The simulated $J - V$ characteristics are shown in Figure 6.9 and the extracted Figures of merit in Table 6.3. The passivation layer is sufficiently thin ($10\ A°$) to allow tunneling.
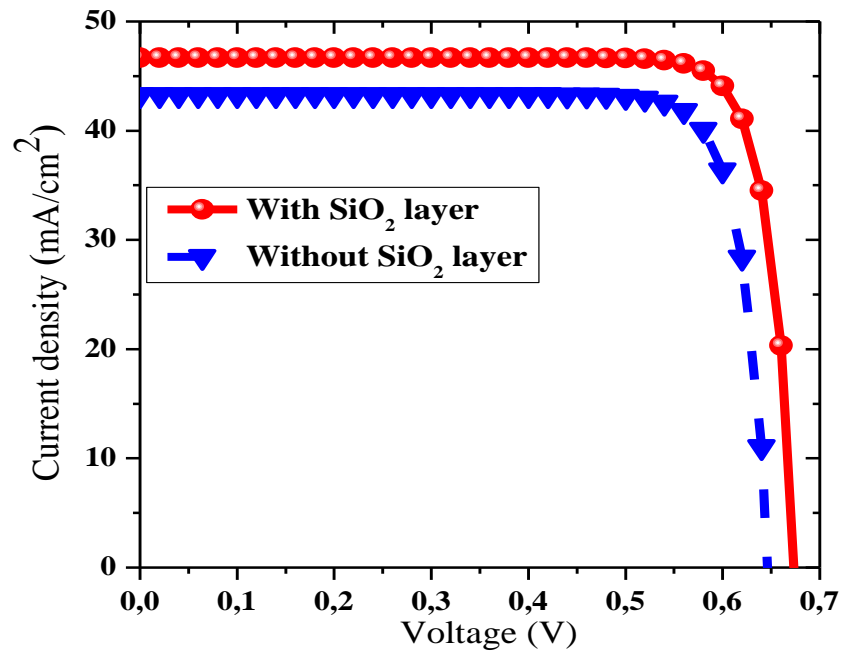
Figure 6.9: Comparison of the $J-V$ characteristics between Si-based solar cell with and without passivation layer.

Table 6-3: Effect of SiO_2 layer on the output parameters.

	J_{sc} (mA/cm^2)	V_{oc}(V)	FF (%)	η (%)
Without SiO_2	43.18	0.64	83.74	23.4
With SiO_2	46.5	0.67	84.16	26.45

Table 6-4 summarizes some experimental results of high TOPCon solar cell using SiO_2 tunneling layer for comparison with our simulation results (table 6-3). We can notice an agreement between results particularly for FF and η of ref [100].

Table 6-4 : Some experimental results of high TOPCon solar cell using SiO_2 tunneling layer

J_{sc}(mA/cm^2)	V_{oc}(mV)	FF (%)	η (%)	**Reference**
42.87	724.1	83.1	25.8	[154]
42.62	726.6	84.28	26.1	[100]
42.5	725	83.3	25.7	[34]
41.2	712	81.1	26	[155]

From Figure 6.9 and Table 6.3, one can note that all the output parameters are affected by the presence of the SiO_2 passivation layer. They increased significantly; the biggest increase occurs for the conversion efficiency η, of which a value of 26% is achieved. SiO_2 has a wider energy gap compared to Si, which creates a barrier in the valence and conduction bands at the same time (Figure 6.10). In the valence band, the barrier prevents the passage of minority carriers (holes), therefore increases V_{oc}. The discontinuity in the conduction band allows the majority carriers (electrons) to bypass the barrier by the tunneling effect which increases their concentration near the contact, and decreases minority carrier concentration, therefore decreasing recombination rate, which leads to an increase of the photocurrent and hence J_{sc}. The same behavior was observed in the experimental work of [42, 156].

Even if some holes are able to tunnel through the SiO_2, they will run into the heavily doped n$^+$ poly-Si layer that offers a barrier for holes to get to the metal contact and recombine [155, 157]. Figure 6.10 displays how electrons pass through the barrier and how holes are repelled.
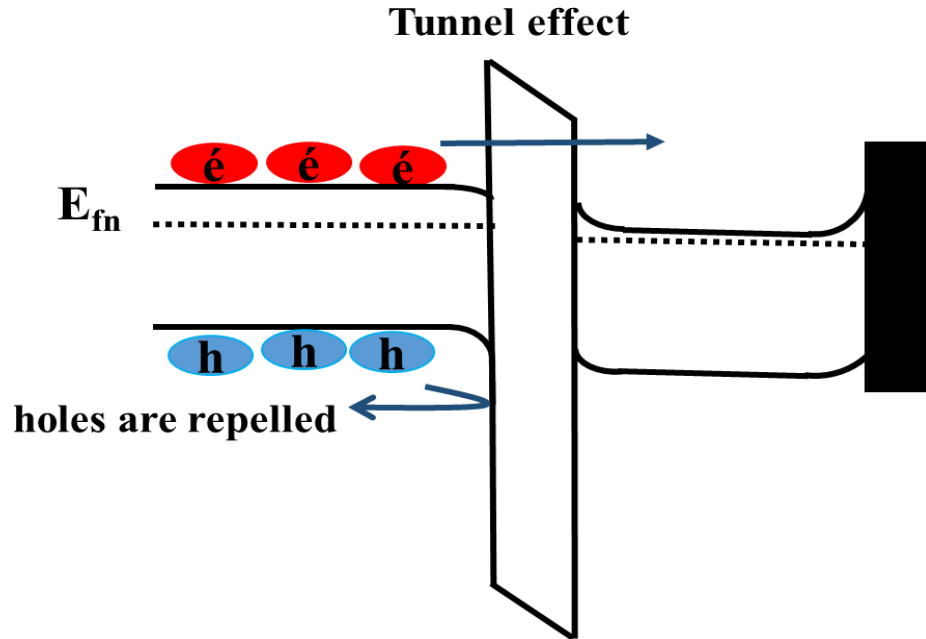
Figure 6.10: Schematic band diagram of the passivation layer in case of Schottky contact.

6.2.4.1 Optimization of Tunnel Oxide Thickness

The tunnel passivation layer (PL) should be designed considering the required thickness to suppress the minority-carrier and maintain the majority-carrier current. This implies that a lower oxide PL thickness degrades V_{OC}, thus, increasing the majority-carrier tunnel current. However, a higher PL thickness degrades FF, therefore, decreasing the current of majority carrier [31]. Only of angstroms (~ A°) order, tunnel oxide thickness has a significant influence (improvement or deterioration) on the solar cell transport characteristics. Therefore, determination of the oxide PL thickness is crucial. Experimental studies proved that the SiO_2 passivation layer should be inferior to 20 $A°$ at which the tunneling becomes efficient [42, 153].

To investigate the PL thickness effect on the $J - V$ characteristics, the back tunneling layer thickness is changed from 10 to 20 $A°$, and the results are compared to the absent PL (0 A°) case. Figure 6.11 presents such characteristics for the BSF doping concentration of 10^{20} cm-3.

As the oxide PL thickness increases, the quantum efficiency increases up to a certain value before it deteriorates. Thus, optimization is required to achieve high performance and good tunneling current in the solar cell. This is well presented by the evolution of the solar cell Figures of merit with increasing the PL thickness as presented in Figure. 6.12.
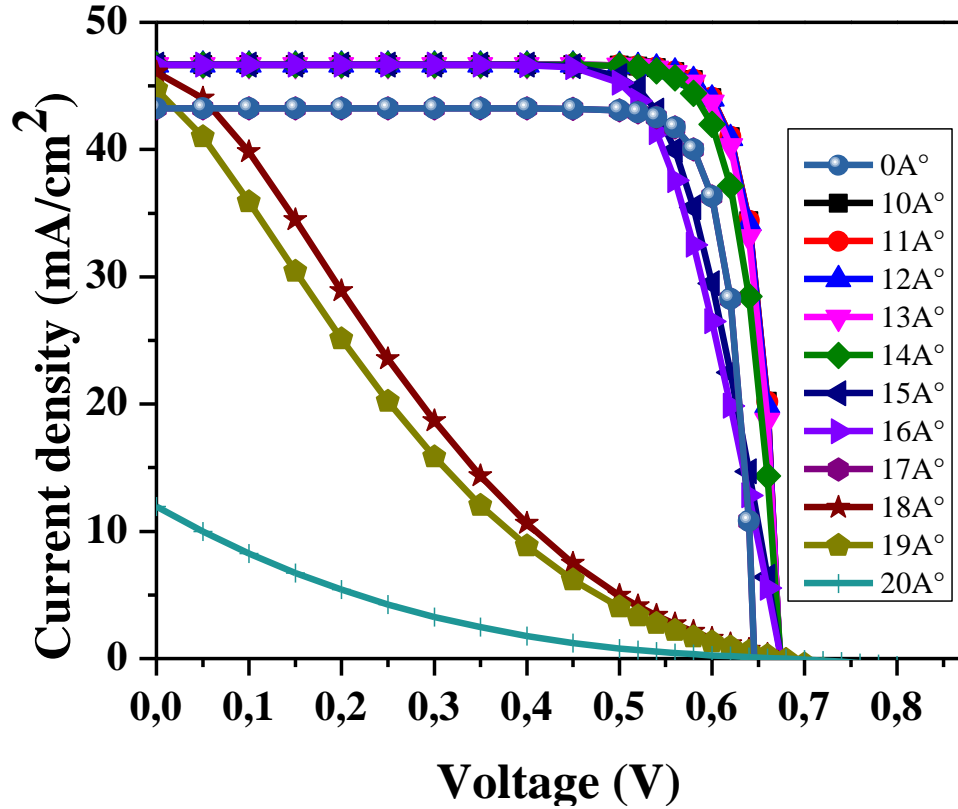
Figure 6.11: Thickness effect of SiO_2 passivation layer on the simulated $J{-}V$ characteristics.

The improvement in the solar cell performance is due to the tunneling effect of electrons through the passivation layer. While, the barrier prevents the passage of holes, hence reducing recombination. (Figure 6.10). This leads to an improvement in the overall performance.

However, as this layer thickness reaches an optimum thickness (13 A°), the fill factor (FF) is vastly deteriorated indicating a series resistance effect as illustrated in Figure 6.13, in which the increase of the SiO_2 PL thickness increases the series resistance (R_s), which affects the fill factor by deterioration [15, 158]. The dropping of FF induces an equivalent reduction of the solar cell efficiency η (Figure. 6.12).

The series resistance (R_s) calculation is achieved by implanting the simulated dark $J - V$ in the Matlab code file and minimizing the $F(V,T)$ function expressed as follows [159] :

$$F(V,T) \; = \frac{V}{2} - \left[(k_B T) \times log\left[\frac{J\,(V)}{T^2 \times 120}\right]\right] \qquad 6.2$$

The series resistance (R_s) corresponds to the current density J_m ,which gives a minimum $F(V,T)$ value. 120 A $. cm^{-2}. K^{-2}$is the effective Richardson constant and R_s is calculated as follow:

$$R_s = k_B T/J(F_m) \qquad 6.3$$

where $J(F_m)$ is the current equivalent to the minimum value of $F(V,T)$ at a fixed temperature.
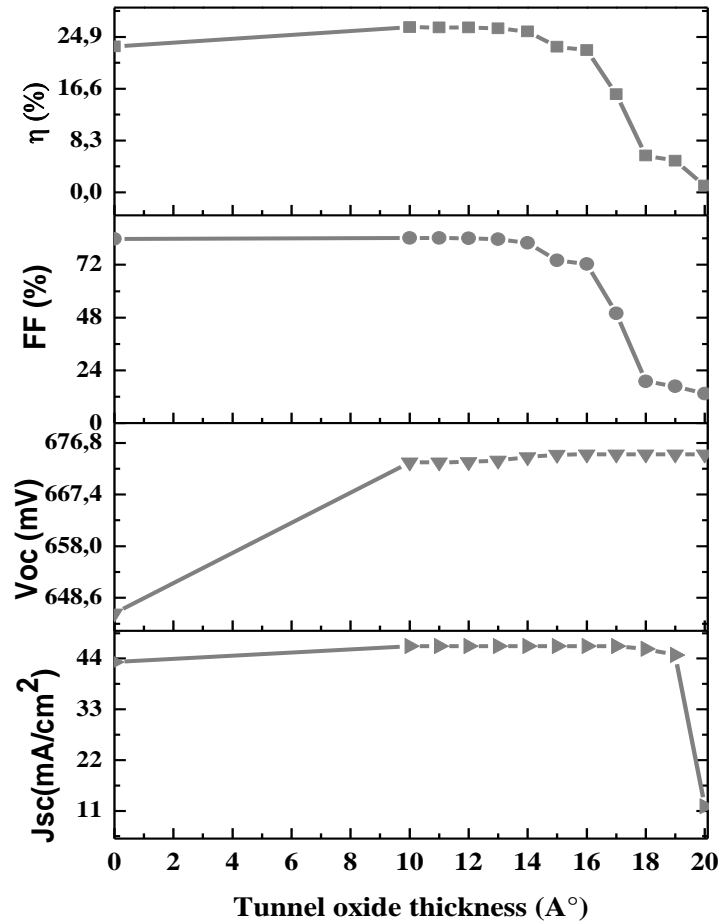
Figure 6.12 : Effect of SiO_2 PL thickness on the Si-based solar cell output parameters.
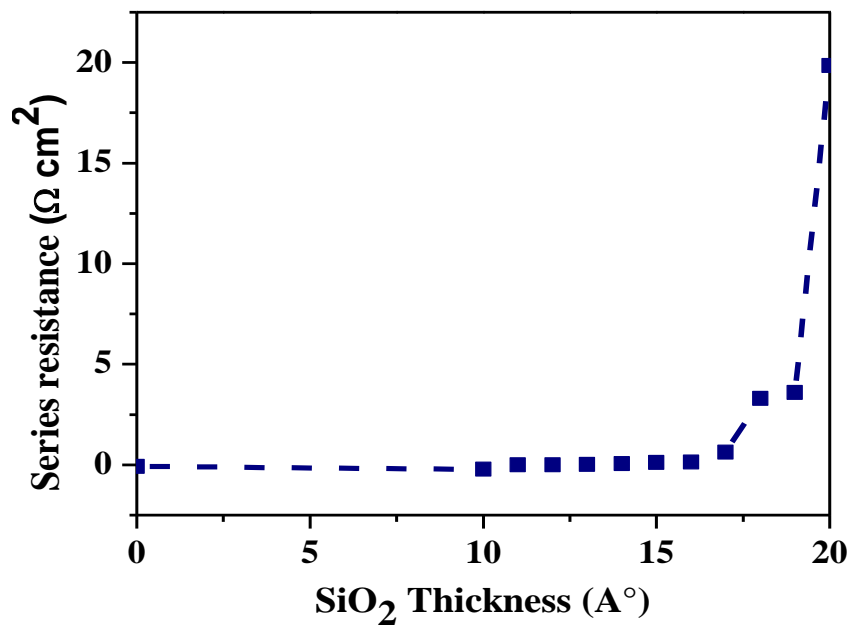
Figure 6.13: Thickness effect of SiO_2 passivation layer on the series resistance of the solar cell.

6.2.4.2 Effect of different tunnel dielectric materials

An unlimited number of studies have focused on the use of SiO_2 as a tunnel oxide or passivation layer. Therefore, research on the replacement of SiO_2 with other materials is required to improve cell performance and explain the dependence of performance on tunnel oxide thickness. In this section, the solar cell performance estimations will be studied by changing the tunnel dielectric material from SiO_2, to Si_3N_4, Al_2O_3, TiO_2, and HfO_2, which are the candidate passivation materials in solar cells. The parameters of tunnel dielectric materials are unique to each material (Table 6.5) and taken from literature [31, 160].

Table 6-5: Tunneling parameters of the included dielectric materials [31], [124].

Parameters	Symbol	SiO_2	Si_3N_4	Al_2O_3	TiO_2	HfO_2
Relative permittivity	ε_{ox}	3.9	7.5	9.1	12	22
Band gap (eV)	E_g	9	5.2	8.72	3.19	6.25
Electron tunnel mass	m_e/m_0	0.4	0.5	0.41	0.4	0.11
Hole tunnel mass	m_h/m_0	0.32	0.41	0.36	0.16	0.29

The tunneling dielectric layer is varied from 10 to 20 A°, in which the thick layer (~20 A°) makes carrier transport quite difficult because insufficient transport channels are provided by the tunnel dielectric layer. Except for HfO_2 where the thickness of the layer can reach up to 40 A° as reported in the literature [31]. The combination of the n-type bulk and the prospective materials has the advantage of improving the solar cell performance. It is revealed that the maximum tunnel dielectric thickness of each material is determined by the majority-carrier effective mass [31]. The energy band diagram of Si and the tunnel dielectrics are shown in Figure 6.14.
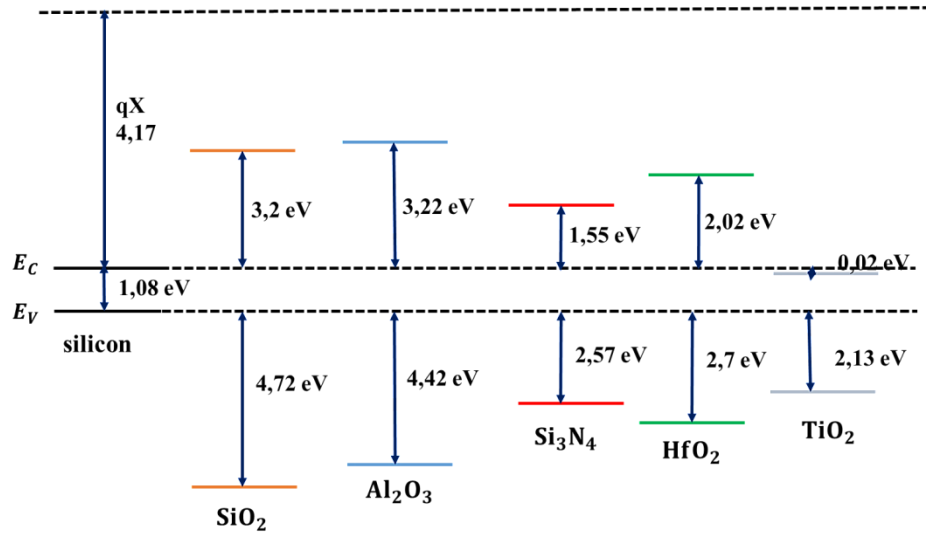
Figure 6.14: Energy band diagram of the tunnel dielectrics aligned with the Si band edges.
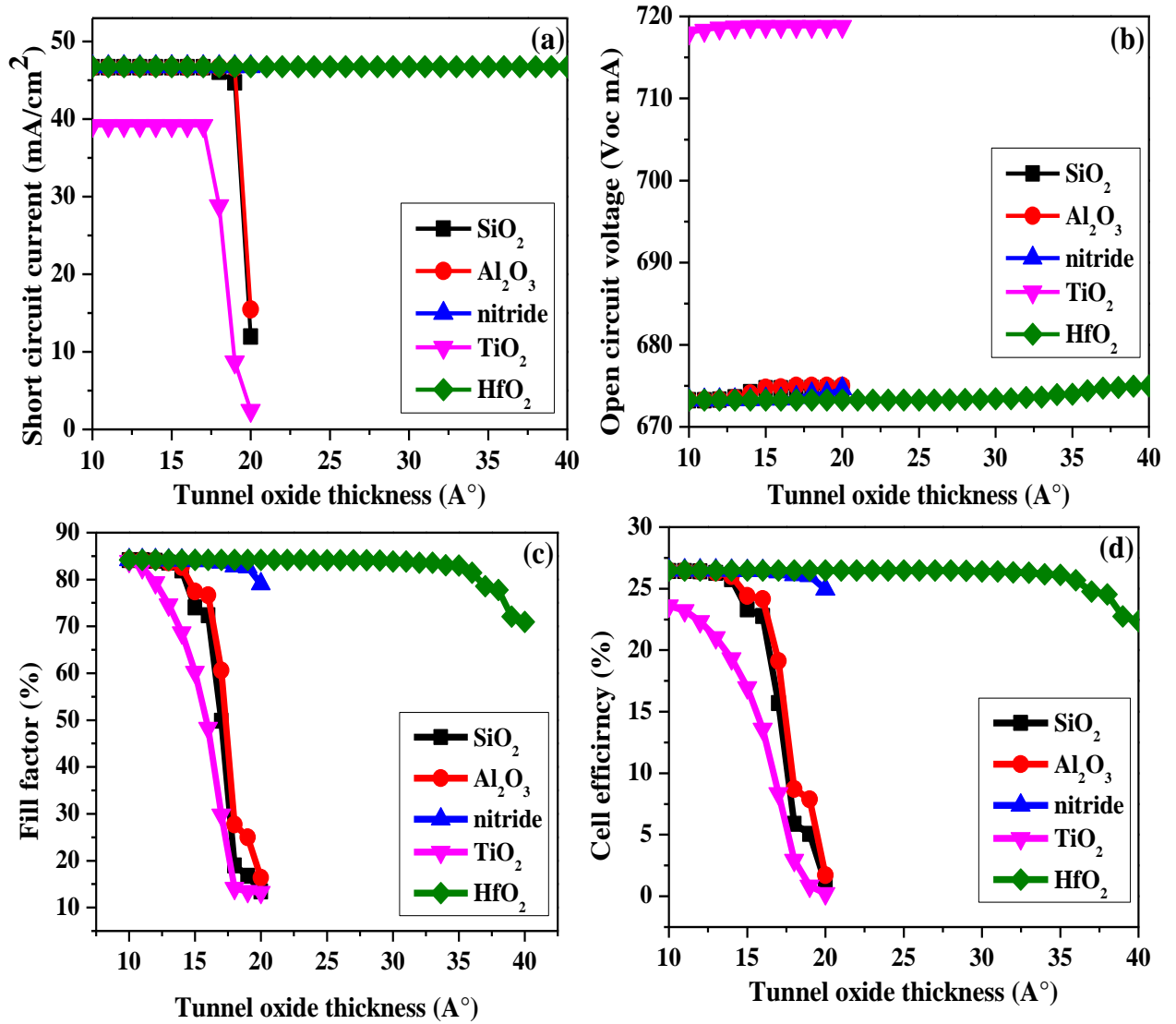
Figure 6.15: Output parameters of the n-type Si-based solar cell against tunnel PL thickness.

Figure 6.15 shows the output parameters of the n-type Si-based solar cell against the tunnel PL thickness. For the four materials SiO_2, Si_3N_4, Al_2O_3 and HfO_2, the maximum performances are almost equal except for the thickness at which FF drops, which is determined by the tunnel barrier. Only Si_3N_4 and HfO_2 showed high cell performances with the thicker tunnel PL of over 15 °A.

Moreover, we can note a negligible change in V_{oc} of the SiO_2, Si_3N_4, Al_2O_3, and HfO_2, materials, except for TiO_2 that increased to more than 715 mV. This increment is probably due to the low bandgap position of this material compared with the others.
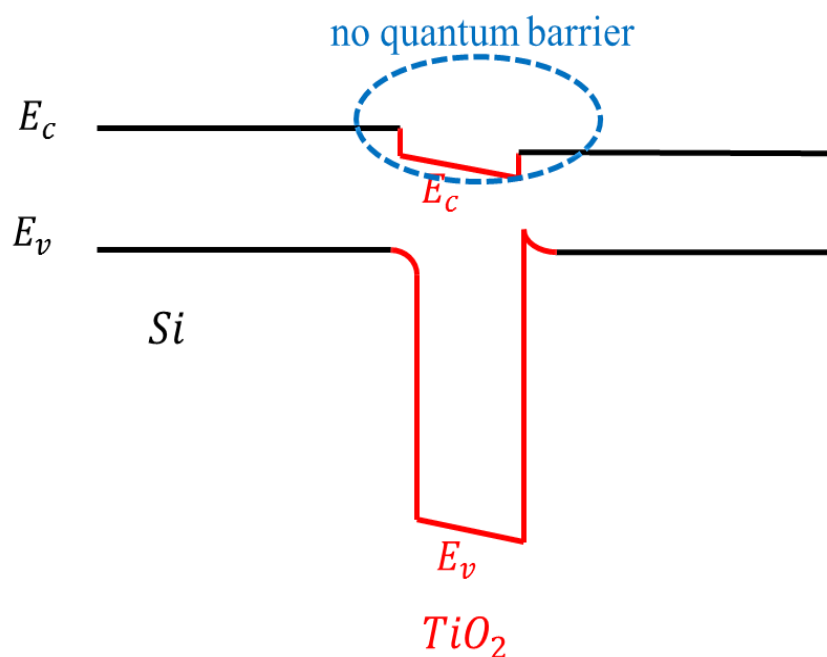
Figure 6.16: Schematic representation of band diagram and tunneling through TiO_2 .

TiO_2 shows the worst performances for J_{SC} (36 mA/cm^2) and efficiency η (~20 %) with the thickness of 15 A° compared to the unpassivated condition (see table 6.3). It is due to its negative electron barrier at the Si/TiO_2 interface. The electrons, when passing from Si to the TiO_2 layer, they suffer a significant concentration reduction because of the large bandgap of TiO_2 (3.19 eV) relative to the silicon bandgap (1.08 eV). Herein, the TiO_2 works as a wide bandgap semiconductor rather than an insulator. As displayed in Figure 6.16, the bottom of the conduction band of TiO_2 is lower than the bottom of the silicon conduction band, so it does not work as a good carrier-selective, degrading consequently the solar cell performance.

The work of Takaya [31] shows the same behavior, and the work of Xinbo Yang.[53] achieved an efficiency of 21.6% for crystalline silicon solar cells featuring a full-area TiO_2-based electron-

selective contact (Thin TiO_2). That approximately agrees with our results in which we achieved efficiency in the range of 23.6 % to 21.02 % with the thickness of 10 to 13 A° respectively.

Considering the cell efficiencies, the choice of the tunnel dielectric material affects only the maximum thickness that the TOPCon solar cell output enough power but provides little difference for the cell efficiency except for TiO_2.

6.3 Effect of deep level defects on the solar cell performance

The performance of commercial solar cells is strongly dominated by defects and impurities. Defects create deep levels energy in the semiconductor bandgap and usually have undesired effects of degrading the carrier lifetime and quantum efficiency of solar cells [162, 163]. Although shallow level defects are often used to introduce charge carriers into semiconductors by doping, deep level defects are frequently found to be harmful in optoelectronic devices, such as solar cells, mainly because they could recombine charge carriers and then diminish the device efficiency [9].

Contrary to the harmful role of defects, some suggestions have claimed that they might be in fact very beneficial [164]. Hu et al.[165] have shown that by coating a "defective TiO₂ layer" of 4 to 143 nm, the Si, GaAs, and GaP photoanodes are chemically stabilized with high efficiency from water oxidation. This is probably because of the excellent surface passivation of the semiconductor by TiO_2, as well as the effective hole transport assisted by the defects. Another hypothesis, which was put forward by Liu et al.[9], mentioned the possibility of suppressing the carrier recombination by introducing deep-level defects. The hypothesis demonstrated on a Si-based solar cell, including a SiO_2 passivation layer, is as follows; "if the deep levels are located in the right energetic position, of the passivation material bandgap, then they will have an affirmative role, which facilitates the transport of the majority carriers, and/or reduces the concentration of minority carriers, at the carrier-collecting region".

To help electron transport, the deep level defects must be slightly above the conduction band minimum (CBM) of the n-type absorber layer (n-type Si-based TOPCon solar cell). While to assist hole transport, defect levels must be slightly below the valence band maximum (VBM) of the p-type absorber layer (p-type Si-based TOPCon solar cell), as illustrated in Figures 6.17 and 6.27, respectively.

In this section, we will investigate the effect of the selected defects in the SiO_2 passivation area, and the carrier transport mechanisms through it, on TOPCon solar cells based on n-type and p-type Si, respectively.
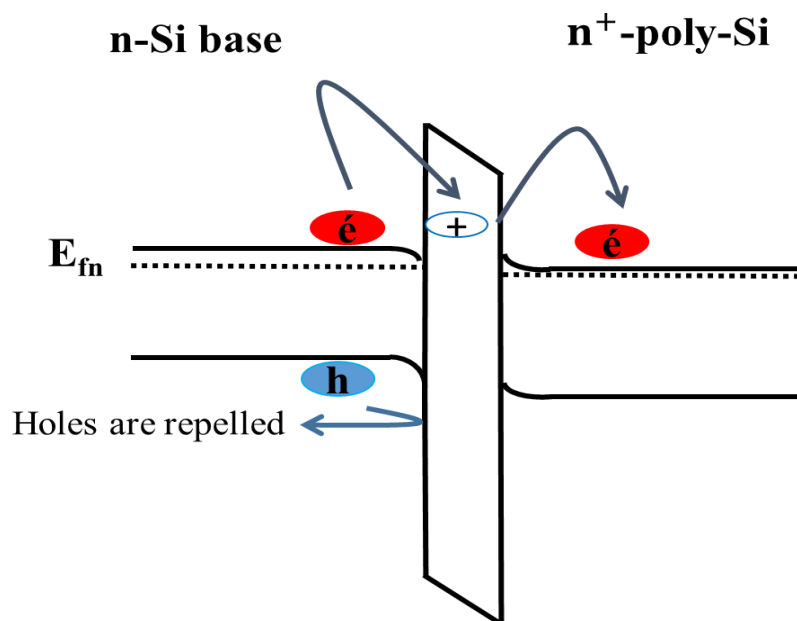
Figure 6.17: Schematic representation of "recombination-suppressing" defects (positively charged) in the SiO_2 layer, which can help transport of electrons and repel holes in the n-type Si-based TOPCon solar cell. Positively charged defects in the insulator layer are represented by the blue circle.

6.3.1   N-type Si-based TOPCon solar cell

6.3.1.1 Device structure

Figure 6.18 depicts the structure of the simulated n-type Si-based TOPCon solar cell. The lower part of the cell includes a full area tunneling contact with a passivating SiO_2 interlayer combined with a heavily n$^+$-doped polysilicon (20 nm), which separates the Al back contact from the n-type Si active layer (200 µm). The input parameters are taken from the literature [144, 153], and are listed in Table 6.6. Electrons and holes photogenerated in the n-type Si layer are separated by the electric field of the p-n junction. Then, they are ultimately collected by the metal contacts on both sides of the cell. Experimentally, and due to the presence of a large density of gap states, metal/Si contacts are especially detrimental. Therefore, in a typical Si-based cell, most of the front area (>95%) is passivated by dielectric layers, such as SiO_2 or Al_2O_3, while only 5% area constitutes metal/Si contact, which is kept to collect carriers[9]. However, neither an AR coating nor any front passivation layer is used in our work (planned for future work).
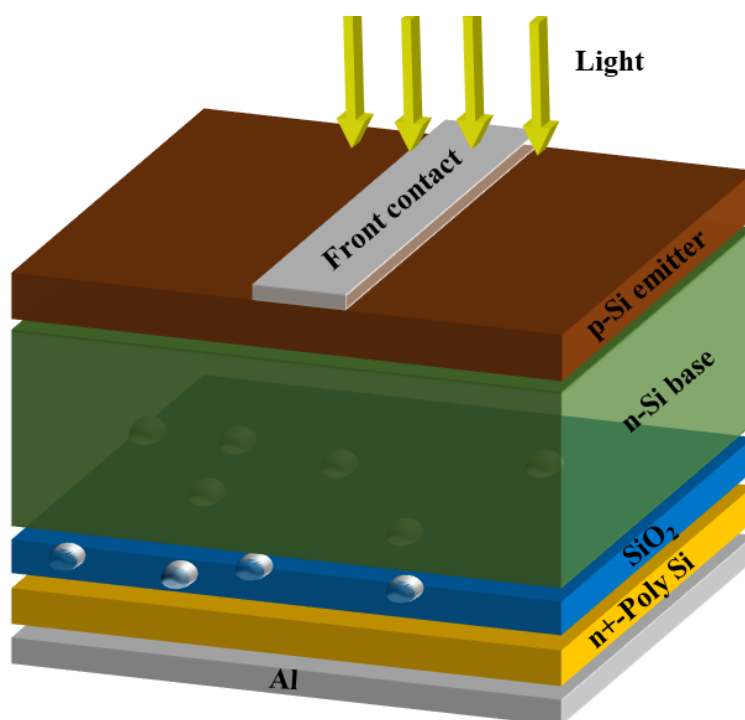
Figure 6.18: Schematic view of the simulated n-type Si-based TOPCon solar cell (pnn$^+$ structure).

Table 6-6: Input parameters related to the simulated solar cell [144, 153].

Layer	Parameters	Designation	Value
	E_g (eV)	Bandgap	1.08
	N_D (cm^{-3})	Density of n-type doping	5×10^{16}
	N_A (cm^{-3})	Density of p-type doping	10^{19}
	n_i (cm^{-3})	Intrinsic carrier density	1.45×10^{10}
	τ (s)	Bulk minority carrier lifetime	1×10^{-6}
	d (µm)	Thickness	200
SiO_2	N_C	Electron effective density	1×10^{19}
	N_V	Hole effective density	1×10^{19}
	E_g	Band Gap	9
	ε_{ox}	Permittivity	3.9
	χ	Electron affinity	0.9
	d (A°)	Thickness	8-18
Polysilicon	N_D	Density of n type doping	10^{20}
	d(nm) [134]	Thickness	20

In our study, we focused on studying defects in the passivation layer, in particular, and its impact on the cell performance but not on other constituents parts of the solar cell. Therefore, it is expected that their presence or absence does not affect the way how deep levels in the rear passivation layer

influence the solar cell performance. The front contact is a simple metallic contact (i.e. there is no loss). The emitter is p-type Si (Figure 6.18). The bulk minority carrier lifetime is $1 \times 10^{-6}\,s$ (which is the default value in Silvaco for Si).

As we were shown in chapter 3, the carrier transport through such structures has been very well studied theoretically and experimentally because of the application of tunneling metal oxide semiconductor diodes (MOS or MIS) [166-168]. The highly doped n$^+$ polysilicon layer provides strong field effect passivation in addition to the chemical passivation of Si by SiO_x, which also eliminates/modifies the interface states on the SiO_2/ n$^+$ polysilicon interface[152, 169].The physical mechanism of this is that SiO_2 for compensates some dangling bonds at the polysilicon (pc-Si) surface and hence reduces surface defects due to these dangling bonds. The combination of the SiO_2 layer and the heavily doped n$^+$ polysilicon achieves excellent surface passivation properties and preserves, at the same time, excellent contact resistance properties, as reported by several research groups[42, 152, 169, 170]. Unfortunately, the thicker passivation layers (more than 15 A°) are not very conducive enough, which blocks the carrier collection and decreases the cell's fill factor. If possible, one would like to make the passivation layer more conductive for majority carriers.

Different phenomena can be involved, as the result of the oxide passivation layer inserted between the two silicon regions of the studied solar cell. In this work, we take into consideration: the direct tunneling mechanism through the potential barrier formed by the oxide layer, and the indirect trap assisted tunneling through the bandgap trap states. The two mechanisms were well described in chapter 5 together with their activation method in the Silvaco Atlas module.

6.3.1.2 Effect of defect level position in the SiO_2 band gap

During this part, we want to demonstrate how one can engineer defect states in the dielectric layer adjacent to Si to enable efficient carrier transport through it, while retaining a very high degree of passivation. This refers to the SiO_2 layer at the back of the solar cell. For that purpose, the solar cell performance is simulated with the presence of defect levels inside the SiO_2 bandgap, where this latter is entirely scanned. The conversion efficiency (η) is the key parameter of the solar cell performance and its evolution, as a function of the defect level position (E_t) in the SiO_2 bandgap is presented in Figure 6.19, for both acceptor and donor traps with a high density of $N_t = 10^{17}$ cm^{-3}[171, 172], and a large cross-section for carrier capture ($10^{-10}\,cm^2$) [173, 174], which could facilitate the carrier transport. These two parameters suggest that it is possible to further tune the

effectiveness of the designated defects. The extracted output parameters are summarized in Tables 6.7 and 6.8 under the effect of acceptor and donor defects, respectively.
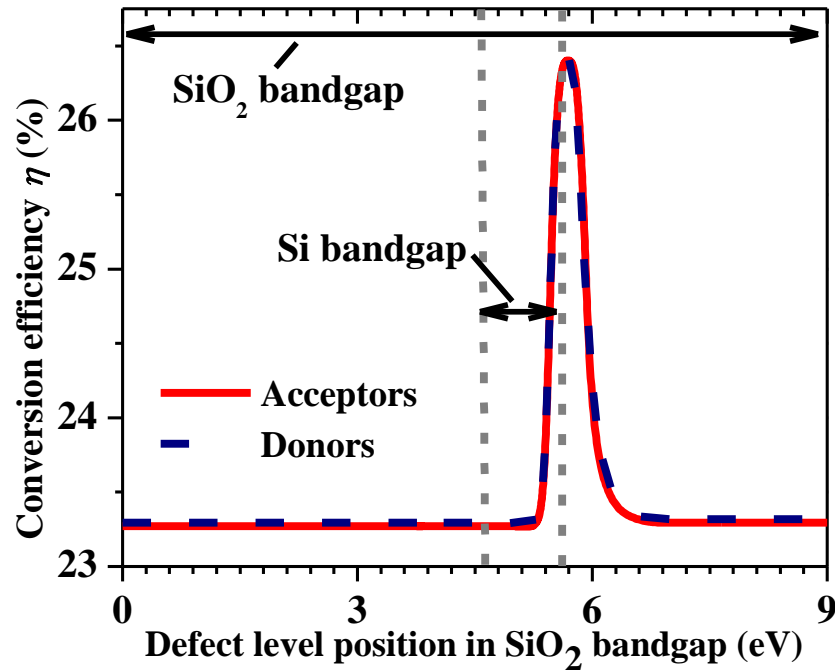
Figure 6.19: The solar cell efficiency (η) evolution as a function of the defect level position (solid lines: deep acceptors and dashed lines: deep donors) in the SiO_2 band gap of the n-type Si-based TOPCon solar cell with PL thickness of 15 A°, and a high defect density of $10^{17} cm^{-3}$.

Table 6-7 : Effect of acceptor defects on the output parameters of the n- type TOPCon structure.

Energy above E_{c-Si} (eV)	0	0.1	0.2	0.3	0.4	0.5	0.6
J_{sc} (mA/cm²)	46,63	46,63	46,63	46,63	46,63	46,63	46,63
V_{oc} (mV)	674.7	674.7	674.7	674.7	674.7	674.7	674.7
FF (%)	74.75	80.70	83.95	84.14	84.06	84.06	74.73
η (%)	23.53	25.38	26.41	26.39	25.76	23.51	23.28

Table 6-8 : Effect of donor defects on the output parameters of the n-type TOPCon structure.

Energy above E_{c-Si} (eV)	0	0.1	0.2	0.3	0.4	0.5	0.6
J_{sc} (mA/cm²)	46,63	46,63	46,63	46,63	46,63	46,63	46,63
V_{oc} (mV)	674.7	674.5	673.4	673.3	673.4	674.3	674.7
FF (%)	74.86	80.75	83.96	84.14	84.06	81.91	74.83
η (%)	23.56	25.39	26.36	26.42	26.39	25.76	23.54

Noting here that ATLAS has a special method for calculating the donor and acceptor defects level E_T from the conduction and valence band edges of the semiconductor(E_c and E_v), as shown in Figure 6.20.
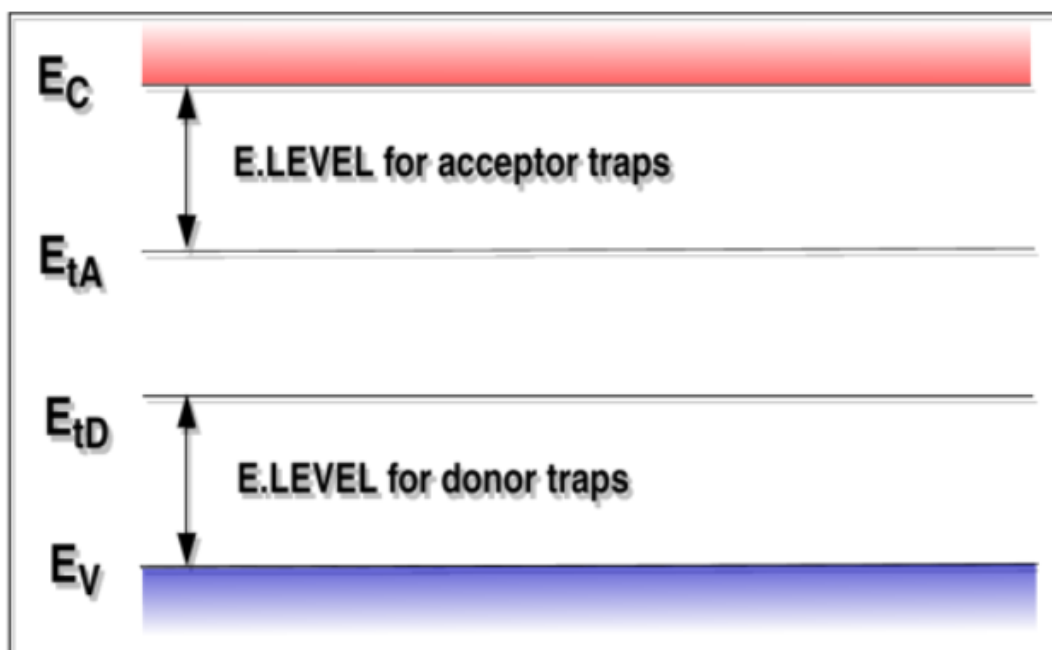
Figure 6.20: ATLAS definition of the trap energy level for acceptor and donor traps in reference to the conduction and valence band edges.

According to the obtained results, the conversion efficiency η reaches more than 26% and the fill factor *FF* reaches more than 84% with either acceptor and donor deep levels that are slightly above the Si CBM ($\sim (E_{C-Si} + 0.3\ eV)$)). This means that only the mentioned deep levels are responsible for assisting the transport of electrons as presented in Figure 6.17. The transport through the untainted passivation layer encounters a large barrier that is defined by the band offset between Si and the passivation material (as seen in Figures 6.10 and 6.17).

If a defect in the passivation layer creates an energy level close to the Si band edge, then the barrier is reduced to the energy difference between the defect level and the Si band edge. In other words, carriers can "leak" through the passivation layer through these defects, therefore reducing the contact resistance. In addition, the defects should avoid creating electronic levels inside the Si bandgap; otherwise, they would cause recombination. Considering these two considerations, one concludes that, to assist the electron transport, ideally the defect level should be slightly above the conduction band minimum (CBM) of the absorber layer. Similarly, to help the hole transport, the defect level should be slightly below the absorber layer valence band maximum (VBM) [9]. The

obtained simulation results are fully consistent with the presented hypothesis of Yuanyue Liu et al [9].

Figure 6.21 shows the calculated defect levels in SiO_2. At the back of the cell, the contacting Si is n-type and the Fermi level of the system lies close to Si CBM. As mentioned before, the selected defects should assist electron transport without causing any additional losses in efficiency.
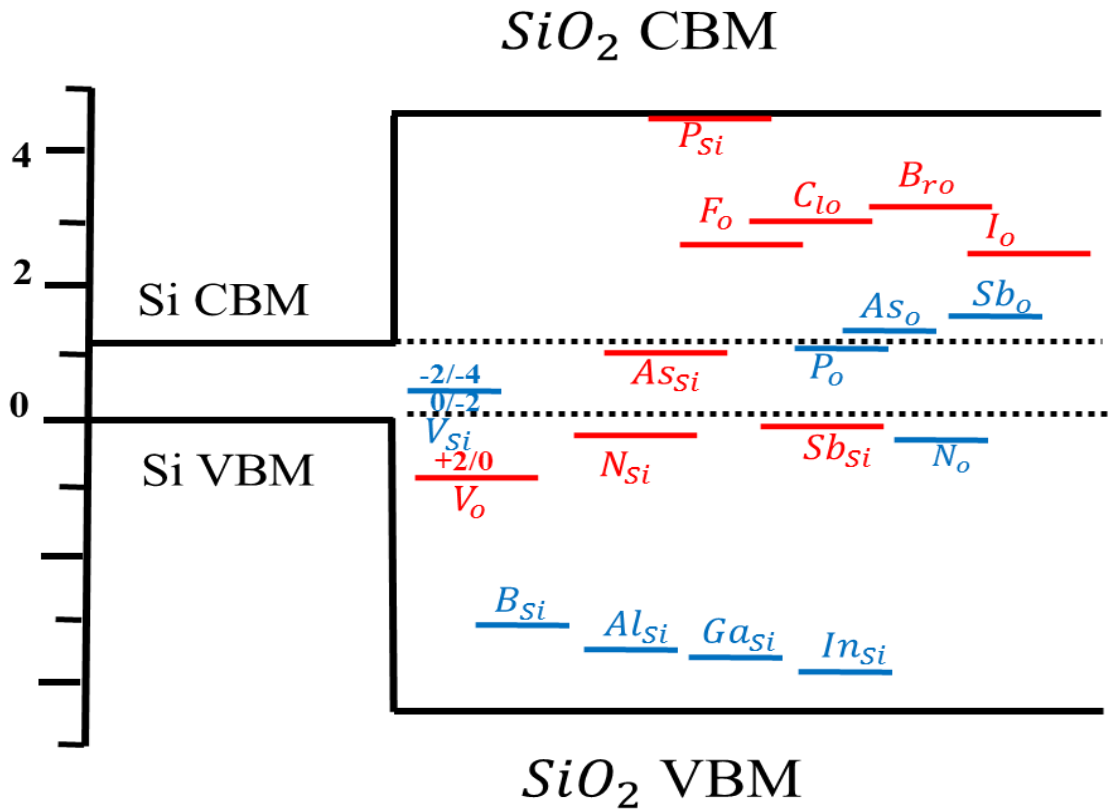
Figure 6.21: Deep level defect position in SiO_2 layer, aligned with the Si band edges. Unless specified, blue bars show the transition levels of +1/0 (donor levels) and red bars show the transition levels of 0/-1 (acceptor levels) [9].

From literature [9, 175, 176], As_O (Arsenic) and Sb_O (Antimony) remain neutral and have levels slightly above the Si CBM, which makes it good candidates for facilitating the electron transport. Furthermore, substituting the oxygen (O) with group VII elements (F, Cl, Br, and I) creates levels close to the Si CBM, and positively charged which could repel holes. By considering Si vacancy (V_{Si}) in SiO_2, clearly, it is undesirable as it has levels within the Si bandgap, which would induce recombination. While the O vacancy (V_O) creates levels outside the Si bandgap and has a level located below the Si VBM [177]. For that, it helps the tunneling of holes instead of electrons and thus is not a beneficial defect for n-type back-contact. Replacing Si by group III elements ($B, Al, Ga,$

andIn) creates negatively charged defects that repel electrons, impeding the electron collection. Moreover, replacing Si with group V elements ($N, P, As,$ and Sb) is not a good choice, because their levels are either inside the Si bandgap, below the Si VBM, or far above the Si CBM. O substitution by N or P is also detrimental because it creates negatively charged defects; in particular, P_O level falls inside the Si bandgap.

6.3.1.3 Effect of defects concentration

To demonstrate that increasing the defect density in a reasonable range, which does not degrade the host material, can enhance the solar cell performance, the defects density will be varied in the range of $10^{13} - 10^{17} cm^{-3}$[178, 179], with the selected energy level of defects (E_t) appropriately chosen (Figures 6.19 and 6.20). Figure 6.22 shows, in (a) and (b) cases, the effect of the acceptor and donor defect densities respectively at the energy levels ($E_{tA}=E_{C-Si}$ +0.3 eV), on the $J - V$ characteristics of the studied solar cell.
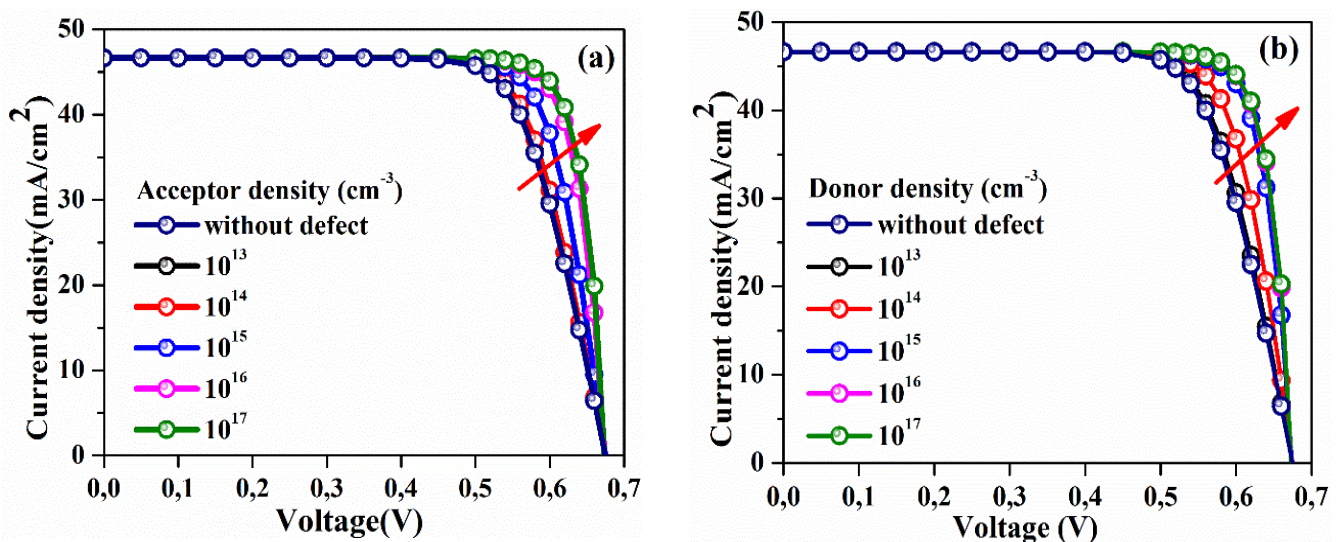
Figure 6.22: $J - V$ characteristics of the n-type Si-based TOPCon solar cell simulated for different: (a) acceptor and (b) donor defect densities, with a PL thickness of 15 A°.

Clearly, there is an enhancement in the solar cell efficiency as the density of either type of defect is increased. The efficiency increases from 23.38% (case without traps) to more than 26.4% for a high trap density ($10^{17} cm^{-3}$) of either acceptor or donor deep defects.

A noticeable fill factor (FF) improvement, and therefore the efficiency (η), are obtained with the deep level defect density increment. This FF enhancement proves that tunneling, through the deep defect, provides a high transport channel for carrier transport, and hence reduces the series resistance [153], which improves the solar cell performance, as shown in Figure 6.23. Therefore, the selected

defects in the SiO_2 layer that are slightly above the n-type Si CBM, and have enough high density, play an intermediary role in helping charge carriers to tunnel through the passivation layer towards the collecting electrode, and consequently enhance, the solar cell efficiency η .
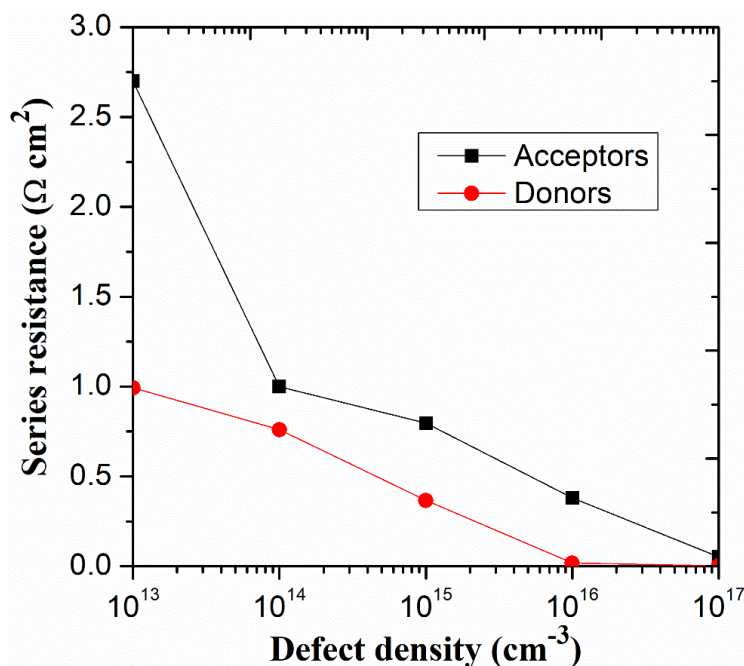
Figure 6.23: Effect of deep level defect density on the series resistance of the n-type Si-based TOPCon solar cell.

6.3.1.4 Effect of the defective PL thickness variation

In this part, the SiO_2 tunneling layer thickness effect on the solar cell performance will be studied. For that purpose, the thickness will be changed from 8 to 18 A°. For each thickness, the acceptor defect density, as an example, will be increased from 10^{13} to 10^{17} cm^{-3} .

Figure 6.24 presents the cell performance parameters versus the acceptor defect density with the SiO_2 PL thickness variation. To have the defects desirable effect, which enhances both of FF and η as the defect density increase, the PL thickness has to be large enough (18 A°) as shown in cases (c) and (d) of Figure 6.24.

For thinner passivation layers (8 -14 A°), the FF and η are already improved, and are slightly affected by the change of defects density. In this case, the transport that allows most of the photo-carriers to pass freely through the SiO_2 layer is dominated by the high direct tunneling current, i.e. the direct tunneling mechanism, through the thin passivation layers. That is to say, direct tunneling dominates the tunneling through traps (Trap assisted tunneling) and ensures FF and η improvement independently of the defect density increase. However, as the passivation layer becomes thicker (more than 16 A°), the indirect tunneling process through the defect levels, becomes more

101

significant with the defect density increment, as it is shown in Figure 6.25. This can be beneficial to improve both *FF* and η as mentioned above. The change in V_{oc} and J_{sc} are very small (less than 1 meV and 0.3 mA/cm^2 respectively). Therefore, they can be considered constant.
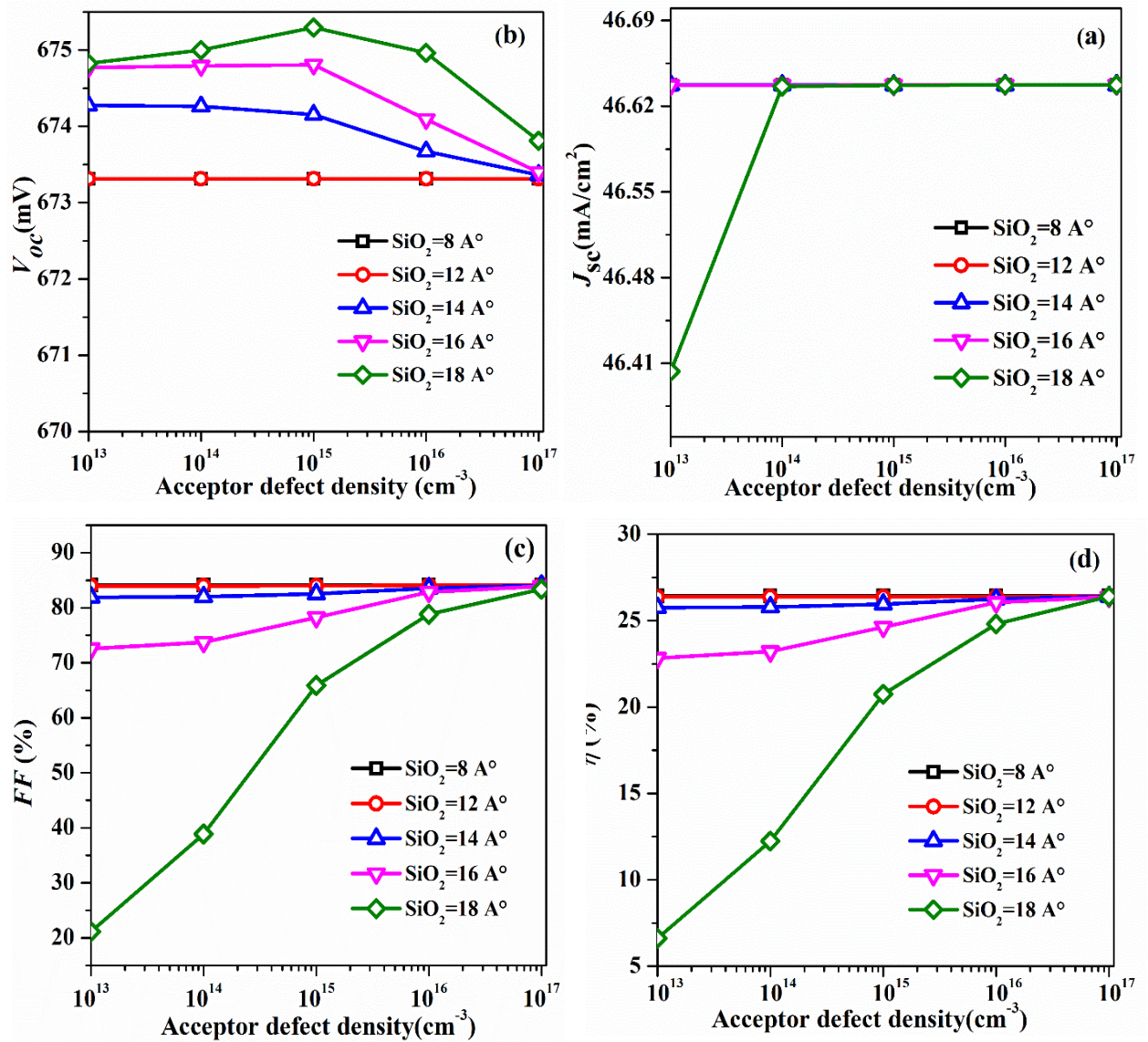
Figure 6.24: Solar cell performance parameters of the simulated n-type TOPCon solar cell versus acceptor defect density with the PL thickness variation: (a) J_{sc}, (b) V_{oc},(c) *FF* and (d) η.

6.3.1.5 Effect of direct and indirect currents

This study aims to find which of the current component dominates the other (direct or indirect), by increasing the PL thickness and the defect density. Figure 6.25 presents the simulated $J - V$ characteristics of the n-type Si-based TOPCon solar cell including the contribution of both direct and indirect (trap-assisted) tunneling currents to the net current density of the solar cell.

Cases (a) and (c) of Figure 6.25 correspond to the thin passivation layer (12A°) with a low defect density of $10^{13} cm^{-3}$ and a high defect density of $10^{17} cm^{-3}$ respectively. We can distinguish the $J - V$ characteristics in the case of indirect current increased by increasing the density of defects without affecting the net current while the direct current is at its maximum value. Cases (b) and (d) of the same figure 6.25 correspond to a thick passivation layer (18 A°) with a low defect density of $10^{13} cm^{-3}$ and a high defect density of $10^{17} cm^{-3}$, respectively. Here we observe the opposite case, the $J - V$ of indirect current increases significantly by increasing the defects density leading to an increase in the net current while the $J - V$ characteristic of the direct current remains constant in the two cases .

As mentioned above, Figure 6.25 proves, as well, that the direct current is dominant for thinner layers. While, for relatively thicker layers, the indirect current through traps becomes the most influential as the defect density increases.

One can conclude that the increase of both PL thickness and the defect density drops the direct tunneling effect sharply. Here and with the defect density increase, the trap-assisted tunneling effect rises and plays an important role in the majority carriers transport through the SiO_2 passivation layer. That improves the net current through the passivation layer and therefore enhances the solar cell output parameters, especially FF and η, compared to the case without defects. It is well known that the distance that carriers travel through the barrier is inversely related to the direct tunneling effect. While this distance is represented by the SiO_2 PL thickness in the direct tunneling case, it is represented by small gaps between traps in the case of the indirect tunneling assisted by traps. Therefore, the total SiO_2 PL thickness will have less effect in the last case, where the trap assisted tunneling effect takes place with the defect density increment.
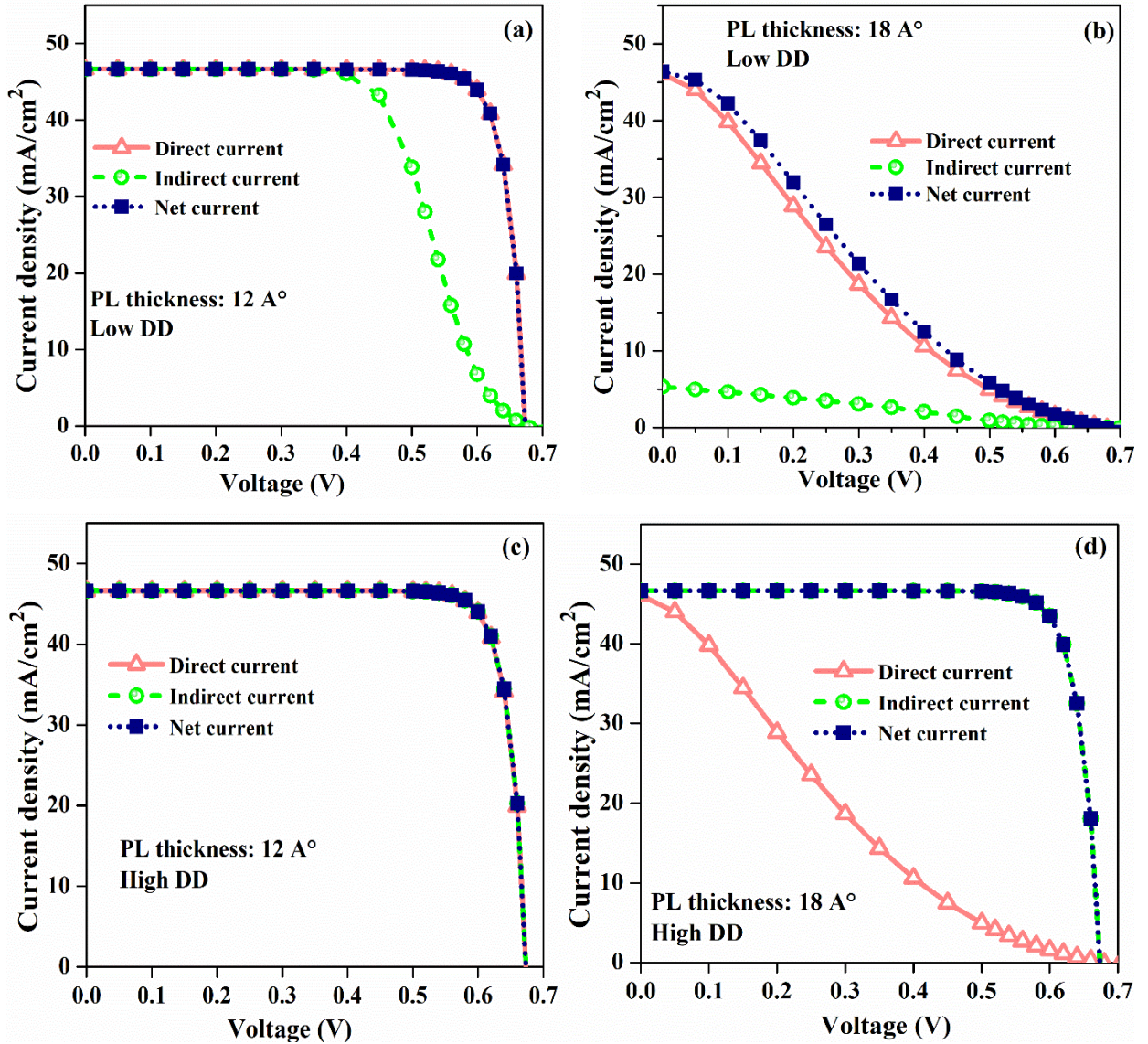
Figure 6.25 : $J - V$ characteristics of the simulated n-type Si-based TOPCon for : (a) thin and (b) thick passivation layer corresponding to a low defect density of $10^{13} cm^{-3}$, (c) thin and (d) thick passivation layer corresponding to a high defect density of $10^{17} cm^{-3}$. The contribution of both the direct and indirect tunneling currents to the net current density is shown.

6.3.1.6 Effect of capture cross section

The capture cross-section is one of the lesser-known magnitudes involved in the charge balance during trapping-detrapping phenomena in the oxide of a metal-oxide-semiconductor structure (MOS) [180]. The work of Yuanyue Liu [9] proposed that a large cross-section for carrier capture could facilitate carrier transport. For that purpose, we used during all previous simulations a large cross-section of $10^{-10} cm^2$ [173, 174].

In this study, however, we will change the capture cross-section in its specified range from 10^{-16} to $10^{-10}\ cm^2$ [173, 174] to see its effect on the output parameters of the simulated n-type Si-based TOPCon solar cell as shown in Figure 6.26.

According to cases (c) and (d) of Figure 6.26, the fill factor FF and the conversion efficiency η are the most sensitive parameters by changing the capture cross-section value. These two parameters display the same shape of increase as the capture cross-section increases. The change in V_{oc} is nearly 1 meV, however J_{sc} is considered constant.

The obtained results intend that the selected defects previously, which are slightly above the silicon CBM, must have a high capture cross section ($10^{-10}\ cm^2$) to enhance the solar cell performance.
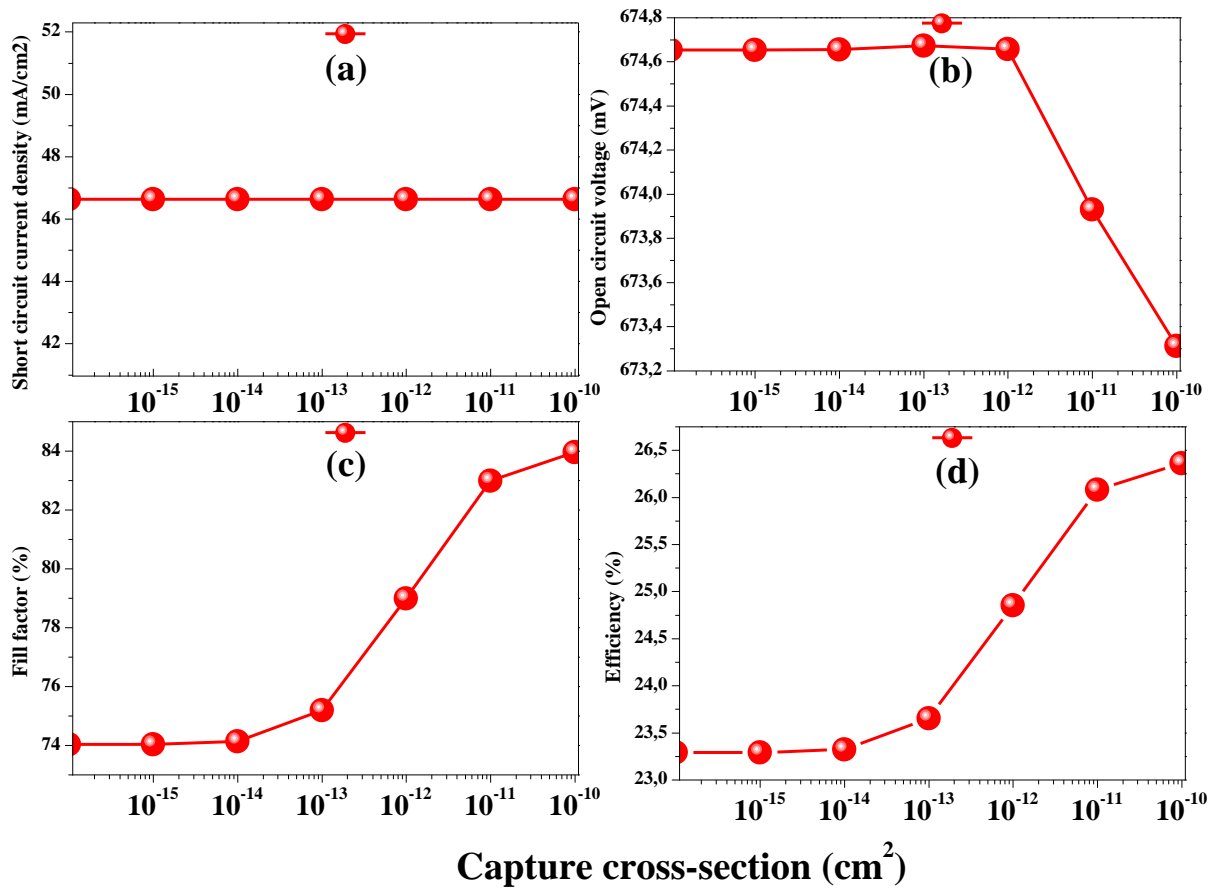
Figure 6.26: Capture cross section effect on the output parameters of the simulated n-type Si-based TOPCon solar cell. (a) J_{sc}, (b) V_{oc},(c) FF and (d) η.

6.3.2 P-type Si-based TOPCon solar cell

The idea of adding defects to assist the transport of majority carriers and/or repel the minority carriers can be applied also to p-type Si (carriers transport through holes) passivated contact with SiO_2 tunneling layer. For that purpose, a similar study is carried out for an npp$^+$ solar cell (Figures 6.27 and 6.28) and analogous results are obtained but with defects slightly under the Si VBM in contrast to the pnn$^+$ solar cell where the defects have to be slightly above the Si CBM, as seen in Figure 6.27.
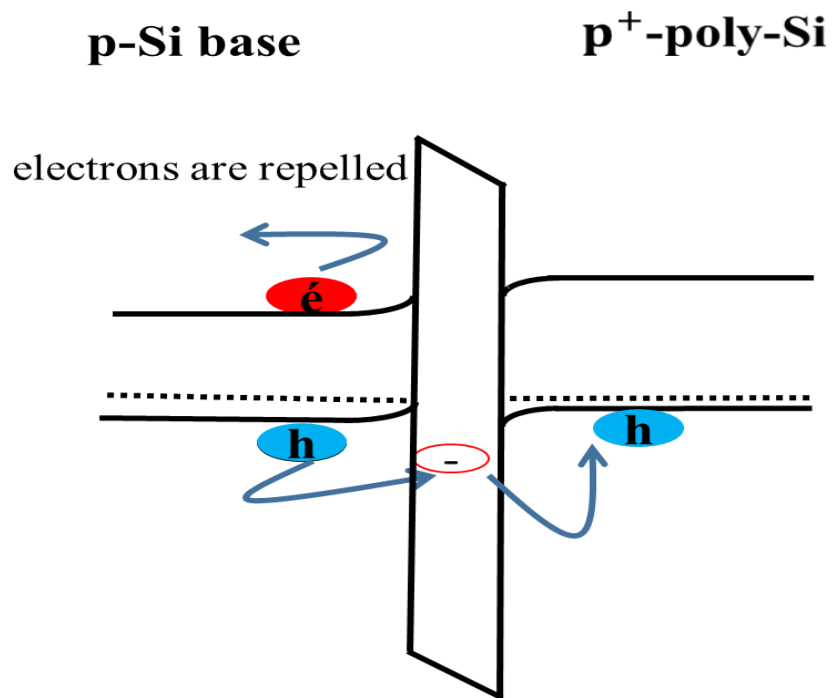
Figure 6.27: Schematic representation of "recombination-suppressing" defects in SiO_2 layer, which can help the transport of holes, and repel electrons in p-type Si-based TOPCon solar cell. Negatively charged defects in the insulator layer are represented by red circles.
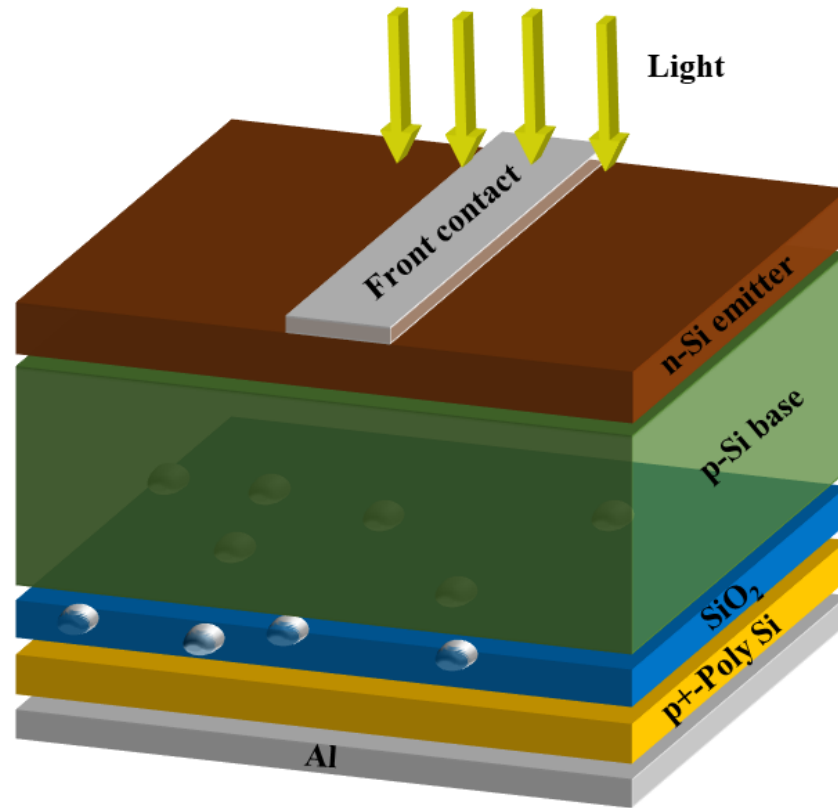
Figure 6.28: Schematic view of the simulated p-type Si-based TOPCon solar cell.

6.3.2.1 Effect of defect level position in the SiO_2 band gap

The whole band gap of SiO_2 is scanned with the presence of deep levels with high density of $10^{17}\ cm^{-3}$ and a large cross section for carrier capture ($\sigma = 10^{-10}\ cm^2$) as illustrated in Figure 6.29. The extracted output parameters are summarized in Tables 6.8 and 6.9 under the effect of acceptor and donor defects, respectively.

From the obtained results, one can be said that the existence of either acceptor or donor deep defects that are below the Si valence band maximum (VBM) with high deep levels enough can enhance the solar cell performance. In which the conversion efficiency η reached more than 25% in presence of defects located at $\sim E_{v-si} - 0.3\ eV$, compared with other defects position.
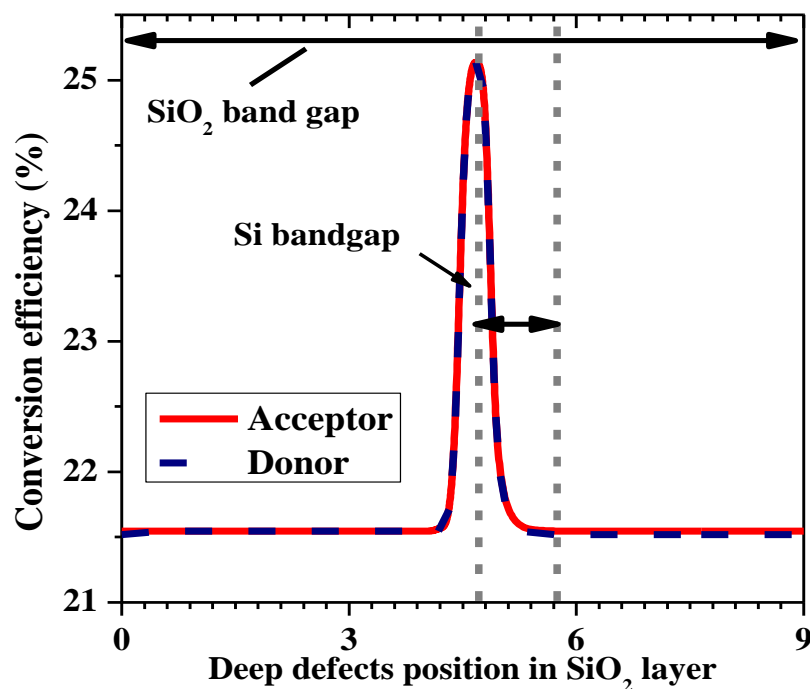
Figure 6.29: The solar cell efficiency *(η)* evolution as a function of the defect level position (solid
lines: deep acceptors and dashed lines: deep donors) in the SiO_2 band gap of the p-
type Si-based TOPCon solar cell with PL thickness of 15 A°, and a high defect density
of $10^{17} cm^{-3}$.

Table 6-9: Effect of acceptor defects on the output parameters of the p-type TOPCon structure.

Energy under E_v (eV)	0	0.1	0.2	0.3	0.4	0.5	0.6
J_{sc} *(mA/cm²)*	45.29	45.29	45.29	45.29	45.29	45.29	45.29
V_{oc} *(mV)*	662.05	662.07	661.63	661.48	661.5	661.96	662.08
FF (%)	71.98	76.07	83.44	83.94	83.89	81.47	73.64
η (%)	21.59	22.81	25.01	25.15	25.14	24.43	22.08

Table 6-10: Effect of donor defects on the output parameters of the p-type TOPCon structure.

Energy under E_v (eV)	0	0.1	0.2	0.3	0.4	0.5	0.6
J_{sc} *(mA/cm²)*	45.29	45.29	45.29	45.29	45.29	45.29	45.29
V_{oc} *(mV)*	662.1	662.01	661.63	661.41	661.52	661.93	662.01
FF (%)	72.00	76.00	83.34	83.93	83.71	81.47	73.66
η (%)	21.50	22.61	24.5	25.11	25.18	24.23	22.01

As we see in Figure 6.21, the O vacancy (V_O) creates levels outside the Si band gap. However, it helps the tunneling of holes instead of electrons, because it has a level located below the Si VBM. Also, $B_{Si}, Al_{Si}, Ga_{Si}, In_{Si}$ creates defects below the VBM with a negative charge that repels electrons and then impede the collection of electrons. This allows us to say that, for p-type Si-based TOPCon solar cell (hole collecting), the selected defects in the SiO_2 passivation layer that are under the Si VBM of the absorber p-type layer play an important role in helping charge carriers to tunnel through the passivation layer, thus suppressing the recombination at the carrier collecting region, therefore, improving the efficiency.

6.3.2.2 Effect of defects concentration, defective layer variation, direct and indirect currents and capture cross-section

Similar results to those of pnn$^+$ solar cell case are obtained for hole transport, but with defects slightly under the Si VBM. Figure 6.30 presents the defects concentration effect on the $J - V$ characteristics of p-type Si-based TOPCon solar cell, in (a) and (b) cases of the acceptor and donor defects respectively. The solar cell efficiency η is enhanced as the density of either type of defect is increased. Indeed, the efficiency increases from 21% (case without traps) to more than 25.5% for a high trap density($10^{17} cm^{-3}$) of either acceptor or donor deep defects.
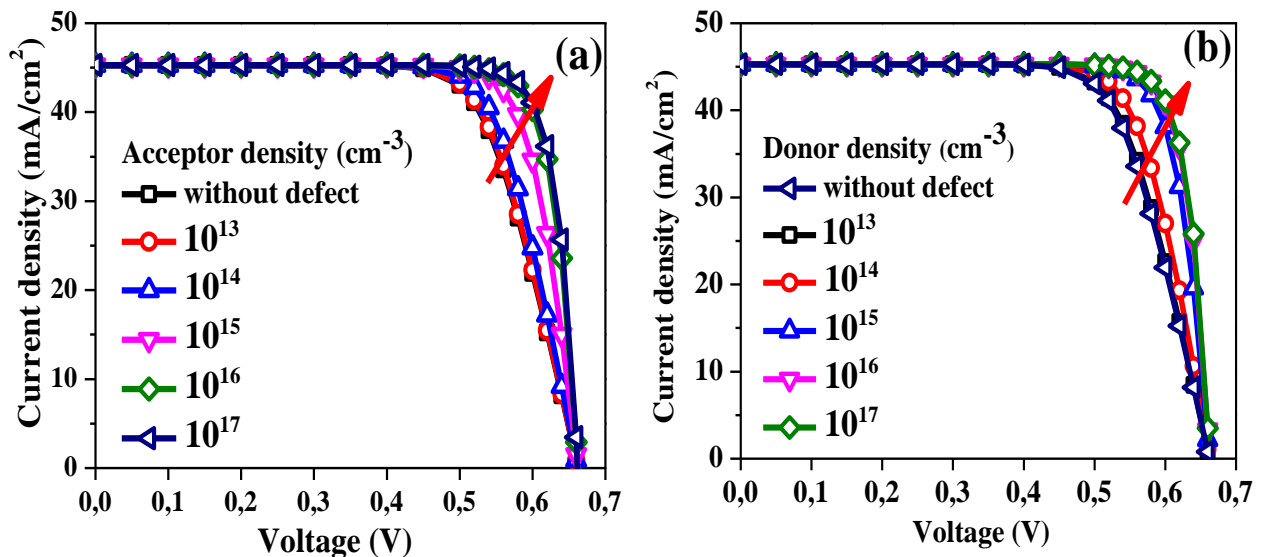
Figure 6.30: $J - V$ characteristics of the simulated p-type Si-based TOPCon solar cell for different: (a) acceptor and (b) donor defect densities, with a PL thickness of 15 A∘.

Figure 6.31 displays the acceptor defects density effect on the solar cell output parameters with PL thickness variation. One can see that defects have a useful effect when the PL thickness becomes

$\geq\ 14A°$. While, for thinner passivation layers, the solar cell performances are already improved and show a neglected sensitivity to the change of defect density.
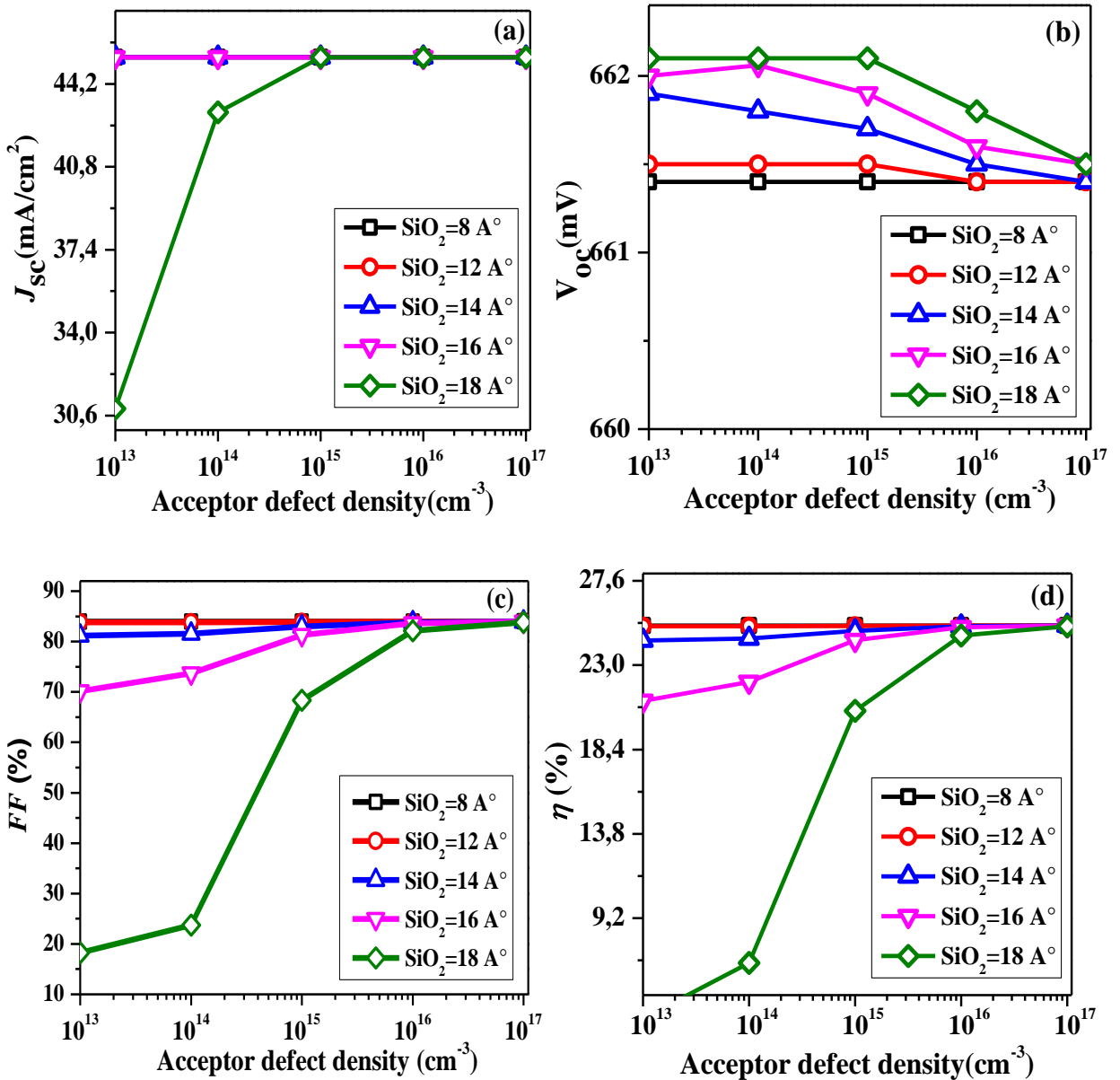
Figure 6.31: Solar cell performance parameters of the simulated p-type Si-based TOPCon solar cell versus acceptor defect density with the PL thickness variation: (a) J_{sc}, (b) V_{oc}, (c) FF and (d) η.

Figure 6.32 presents the simulated $J - V$ characteristics of the p-type Si-based TOPCon solar cell, showing both the direct and indirect (through defects) tunneling currents together with the net current density of the solar cell.

We can see similar behavior to the n-type Si-based solar cell results. Indeed, the high defect density is beneficial only for relatively thicker passivation layers. In this case, the defect level should be

slightly below the silicon VBM to help the hole current tunneling effect through them. For thinner passivation layers, however, the presence of defects has an asignificant effect.
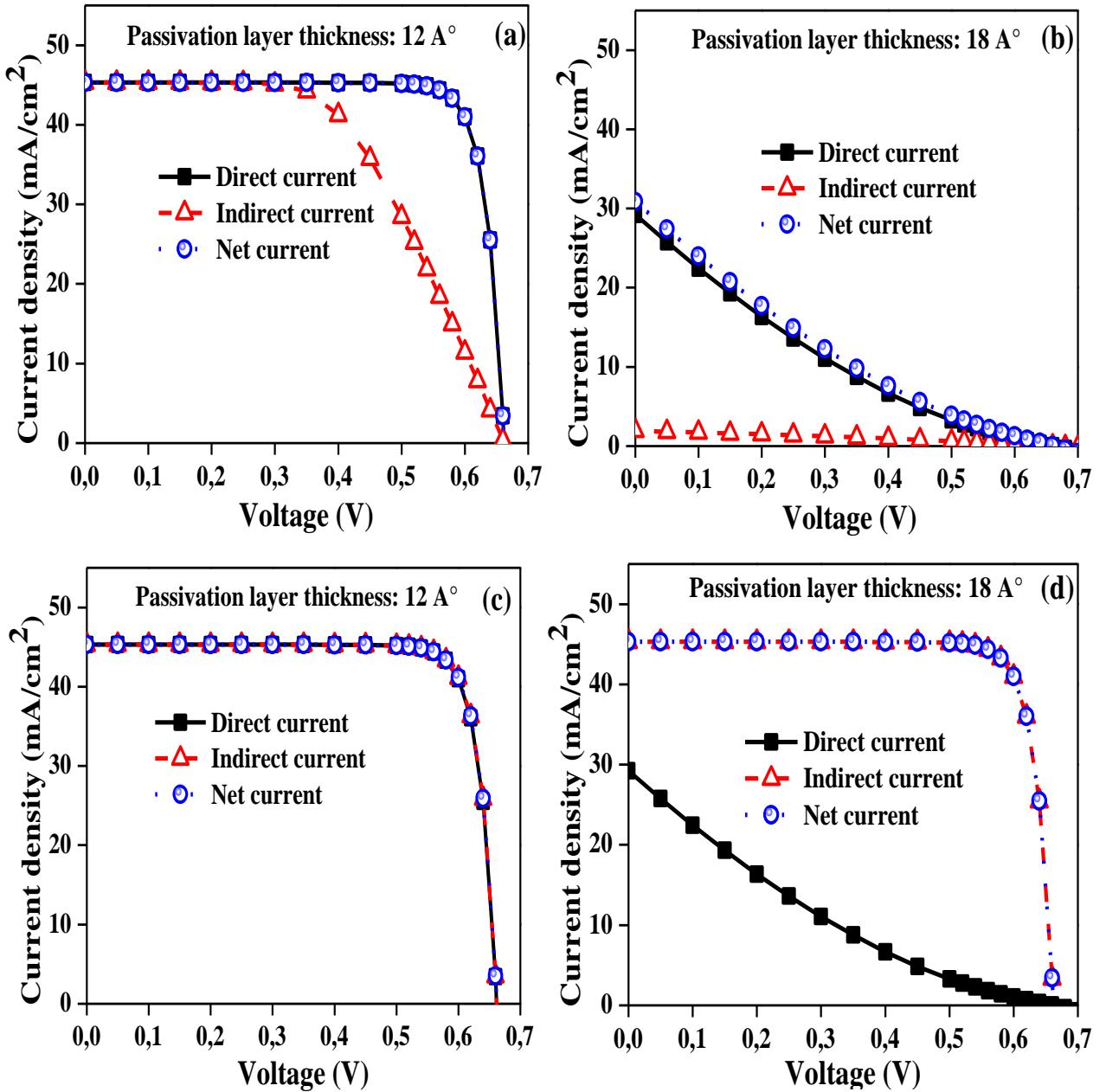
Figure 6.32: $J - V$ characteristics of the simulated p-type Si-based TOPCon solar cell for: (a) thin and (b) thick passivation layer corresponding to a low defect density of $10^{13} cm^{-3}$, (c) thin and (d) thick passivation layer corresponding to a high defect density of $10^{17} cm^{-3}$. The contribution of both direct and indirect tunneling currents to the net current density is shown.

Figure 6.33 illustrates the capture cross-section effect on the output parameters of the simulated p-type Si-based TOPCon solar cell. The cases (c) and (d) of Figure 6.33 show a significant capture

cross-section dependency of FF and η. These two parameters exhibit the same behavior as the capture cross-section increases. The V_{oc} and J_{sc} however, are almost insensitive
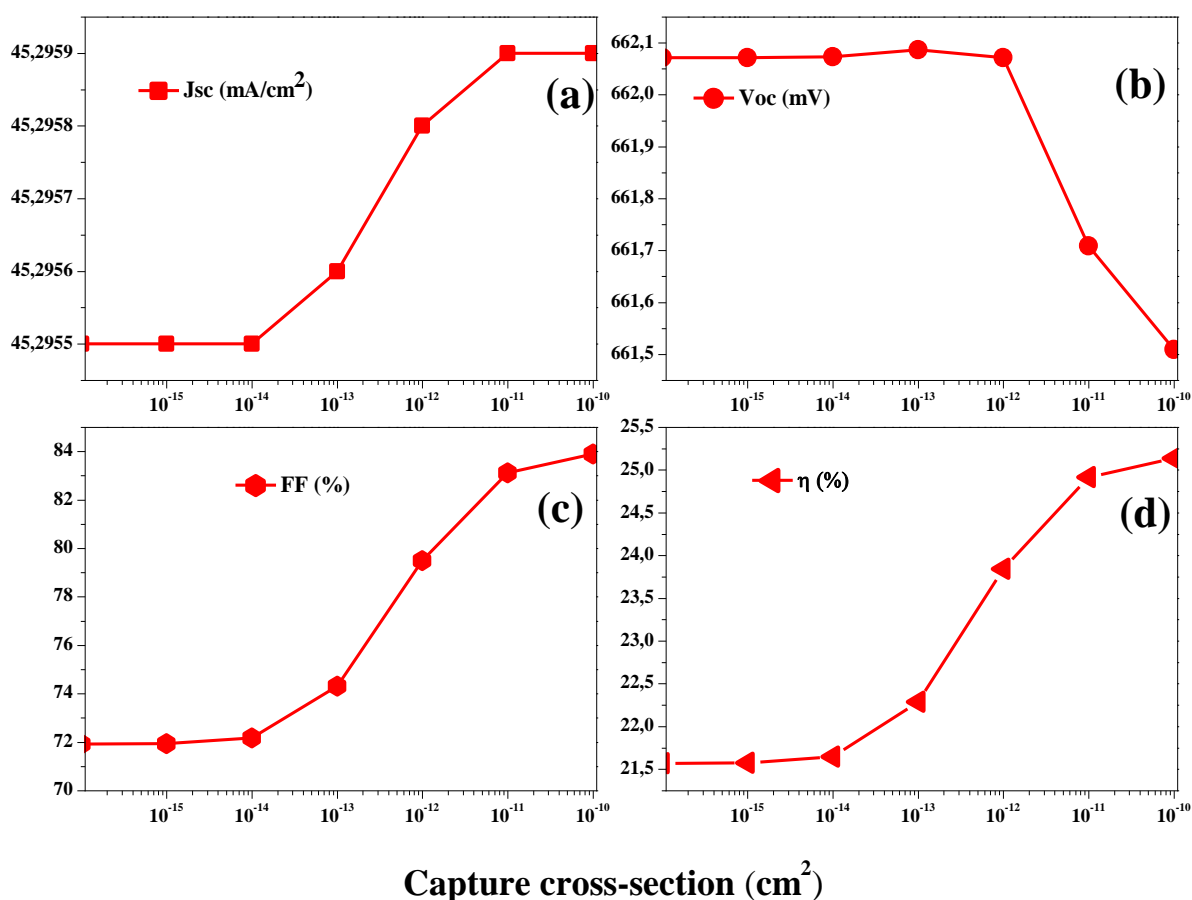
Figure 6.33: Capture cross section effect on the output parameters of the simulated p-type Si-based TOPCon solar cell: (a) J_{sc}, (b) V_{oc},(c) FF and (d) η.

From this study, we can conclude that there is a proper amount of deep defects inserted into the passivation layer, which are needed to get high-efficiency silicon solar cells with relatively thick PL of at least 15 °A. This is essential to improve the solar cell performance. However, the challenge is how to implement the idea in experimental. How to select a proper SiO_2 thickness and control the deep levels density. Choosing the appropriate method to introduce the designated defects is a kind of technical art, and a significant effort is needed for the optimization of the material properties and device structure.

Liu et al. [15] pointed out that the designated defects could be introduced experimentally, by plasma enhanced chemical vapor deposition (PECVD) (PECVD has been used to introduce fluorine (F) into SiO_2) [181, 182], ion implantation [183], oxidation of an impurity-enriched layer of Si wafer, thermal or plasma nitridation, or Atomic layer deposition [20] with various precursors containing the desired elements [9, 184].

<u>Conclusion</u>

With the manufacturing technology advancement, silicon-based solar cell efficiency has been increased progressively recently, especially with some innovative cell structures introduced to reduce the recombination losses of solar cells. Recently, the passivation of solar cells surfaces became an additional step to improve their efficiency. It is used in photovoltaic cells in order to limit the defects created at the different stages of the cell manufacturing process, and to obtain high conversion efficiencies. Moreover, and contrary to the harmful role of defects, some recent suggestions have claimed that they might be very beneficial. It mentioned the possibility of suppressing the carrier recombination by introducing deep-level defects.

In this work, we have investigated the tunnel oxide passivated contact (TOPCon) solar cell based on n-type Si (p-n-n$^+$ structure), and p-type Si (n-p-p$^+$ structure), respectively, using the two-dimensional (2D) SILVACO- ATLAS module, and by considering the AM1.5G solar spectrum at ambient temperature. We started by the study of a p-n single junction device. Then, we investigated the p-n-n$^+$ configuration in which an n$^+$ polysilicon layer is added as back-surface field (BSF) layer in both Schottky and Ohmic contact samples. The BSF layer reduces the barrier height of the Schottky barrier, and creates a supplementary field, which helps block minority carriers (holes) from diffusing to the back-contact layer of the solar cell. This is helpful to reduce the bottom surface recombination, and enhance the majority carrier collection. By increasing the BSF layer doping concentration from 5×10^{16} to 1×10^{20} cm^{-3}, an improvement has been fulfilled in the output parameters of the Schottky contact based solar cell. This is probably due to the enhanced tunneling through the heavily doped layer that provides a large number of electrons and reduces the depletion region thickness.

A passivation layer, which acts as a tunneling path for electrons and a barrier for holes to reduce recombination, can further enhance the solar cell performance. For that purpose, a wide bandgap (SiO_2) passivation layer (PL) has been included, between the absorber and BSF layers, to investigate the tunnel oxide passivated contact (TOPCon) solar cell. The combination between the SiO_2 passivation layer and the BSF layer has improved the passivation quality of the contact (adding chemical passivation to field passivation). The performance improvement of the solar cell, resulting from the PL insertion, is due to the tunneling effect of electrons through the passivation layer while the barrier prevents holes, hence reducing recombination. However, when SiO_2 PL thickness become higher than an optimum value around ~ 15°A, the fill factor (FF) is vastly

deteriorated, indicating a series resistance effect, which induces an equivalent reduction of the solar cell efficiency η.

Due to the possibility of a beneficial defect effect on the Si-based solar cell performance, we explored the effect of the PL deep level defect, which includes the energy level position, the defects density, the defective tunneling layer thickness and the capture cross-section. For the n-type Si-based TOPCon solar cell, the conversion efficiency η and the fill factor *FF* reached more than 26% and 84%, respectively, with either acceptor and donor deep levels that are slightly above the Si CBM ($\sim (E_C + 0.3\ eV)$)). This means that, to assist the electron transport, ideally the defect level should be slightly above the CBM of the Si absorber layer. Then, the well-selected defects can facilitate the transport of majority carriers, and/or repel minority carriers. It was also found that deep defects with high density (of $\sim 10^{17} cm^{-3}$) have a beneficial role only for relatively thick passivation layers ($\geq 15\ A°$). However, the presence of defects for thinner passivation layers has no valuable effect. In this case, the direct tunneling effect dominates the process, relatively to tunneling via defect levels.

The capture cross-section variation in its specified range from 10^{-16} to $10^{-10}\ cm^2$ has shown a significant effect on *FF* and η. These two parameters exhibit similar augmentation as the capture cross-section increases. The V_{oc} and J_{sc} however, stay almost sensitive.

An additional study by changing the tunnel dielectric materials from the conventional SiO_2 to Si_3N_4, Al_2O_3, TiO_2 and the prospective HfO_2 was realized. The choice of the tunnel dielectric material affects only the maximum thickness that the TOPCon solar cell output enough power but provides little difference for the cell efficiency except for TiO_2.

Finally, a similar study was carried out on the p-type Si-based TOPCon solar cell, in which the carrier transport and tunneling process are mainly achieved by holes. In this case, the defect level should be slightly below the silicon VBM ($\sim E_v - 0.3\ eV$) to help the hole current tunneling effect through them. With this condition, the conversion efficiency η and the fill factor *FF* reached more than 25% and 83%, respectively.

From this study, we can conclude that there is a proper amount of deep defects inserted into the passivation layer, which are needed to get high-efficiency silicon solar cells with relatively thick PL at least of 15 A°. This is essential to improve the solar cell performance. Experimentally, the idea of adding deep defects to enhance the solar cell efficiency is a great challenge for high-efficiency solar cells and opens possibilities to combine good surface passivation with enhanced carrier transport. Tunneling layers thus could be made thicker, less prone to process uncertainties

and spatial inhomogeneities, and could be applied to other devices besides solar cells. In addition, the same idea could be applied to other passivation materials, other solar cell structures and may be applied to space solar cells.

In prospective studies, we can apply the idea of adding defects to the studied passivation materials Si_3N_4, Al_2O_3, TiO_2, and HfO_2 to show their effect on the solar cell performance. In addition, we envision investigating a similar study using the Al_2O_3 as passivating layer at the front of the solar cell.

References

1.   Aleskandrova, P., et al., Poole-Frenkel conduction in Al/ZrO 2/SiO 2/Si structures. The European Physical Journal B-Condensed Matter and Complex Systems, 2006. 52(4): p. 453-457.
2.   Smestad, G.P., Optoelectronics of solar cells. Vol. 115. 2002: SPIE press.
3.   Wilson, G.M., et al., The 2020 photovoltaic technologies roadmap. Journal of Physics D: Applied Physics, 2020. 53(49): p. 493001.
4.   https://www.waaree.com/. 29/05/2021

5.   Solar Photovoltaic Cell Basics. Available from: https://www.energy.gov/eere/solar/solar-photovoltaic-cell-basics:[
6.   Battaglia, C., A. Cuevas, and S. De Wolf, High-efficiency crystalline silicon solar cells: status and perspectives. Energy & Environmental Science, 2016. 9(5): p. 1552-1576.
7.   Blakers, A., et al., High efficiency silicon solar cells. Energy Procedia, 2013. 33: p. 1-10.
8.   Allen, T.G., et al., Passivating contacts for crystalline silicon solar cells. Nature Energy, 2019. 4(11): p. 914-928.
9.   Liu, Y., et al., Suppress carrier recombination by introducing defects: The case of Si solar cell. Applied Physics Letters, 2016. 108(2): p. 022101.
10.   Reinders, A., et al., Photovoltaic solar energy: from fundamentals to applications. 2017: John Wiley & Sons.
11.   Kitai, A., Principles of Solar Cells, LEDs and Diodes: The role of the PN junction. 2011: John Wiley & Sons.
12.   Luque, A. and S. Hegedus, Handbook of photovoltaic science and engineering. 2011: John Wiley & Sons.
13.   Tada, H., et al., Solar cell radiation handbook. 1982.
14.   Cuevas, A. and D. Yan, Misconceptions and misnomers in solar cells. IEEE Journal of Photovoltaics, 2013. 3(2): p. 916-923.
15.   Dadu, M., A. Kapoor, and K. Tripathi, Effect of operating current dependent series resistance on the fill factor of a solar cell. Solar energy materials and solar cells, 2002. 71(2): p. 213-218.
16.   Trupke, T., et al., Temperature dependence of the radiative recombination coefficient of intrinsic crystalline silicon. Journal of Applied Physics, 2003. 94(8): p. 4930-4937.
17.   Algora, C. and I. Rey-Stolle, Handbook of concentrator photovoltaic technology. 2016: John Wiley & Sons.
18.   Kasap, S., Springer handbook of electronic and photonic materials. 2006: Springer Science & Business Media.
19.   Würfel, P. and U. Würfel, Basic structure of solar cells, in Physics of Solar Cells—From Principles to New Concepts. 2005, Wiley-VCH. p. 109-136.
20.   Kerr, M.J., A. Cuevas, and R.A. Sinton, Generalized analysis of quasi-steady-state and transient decay open circuit voltage measurements. Journal of applied physics, 2002. 91(1): p. 399-404.

21. Shockley, W. and W. Read Jr, Statistics of the recombinations of holes and electrons. Physical review, 1952. 87(5): p. 835.

22. Kerr, M.J. and A. Cuevas, General parameterization of Auger recombination in crystalline silicon. Journal of Applied Physics, 2002. 91(4): p. 2473-2480.

23. Strauss, U., W. Rühle, and K. Köhler, Auger recombination in intrinsic GaAs. Applied Physics Letters, 1993. 62(1): p. 55-57.

24. Richter, A., M. Hermle, and S. Glunz, IEEE J. Photovolt. 3, 1184 (2013). 2013.

25. Richter, A., M. Hermle, and S.W. Glunz, Reassessment of the limiting efficiency for crystalline silicon solar cells. IEEE journal of photovoltaics, 2013. 3(4): p. 1184-1191.

26. Hall, R.N., Electron-hole recombination in germanium. Physical review, 1952. 87(2): p. 387.

27. Rein, S., Lifetime spectroscopy: a method of defect characterization in silicon for photovoltaic applications. Vol. 85. 2006: Springer Science & Business Media.

28. Aberle, A.G., Surface passivation of crystalline silicon solar cells: a review. Progress in Photovoltaics: Research and Applications, 2000. 8(5): p. 473-487.

29. Wörfel, P., Physics of Solar cells: from Principles to new Concepts. 2005, Wiley-VCH Verlag.

30. !!! INVALID CITATION !!!

31. Sugiura, T., S. Matsumoto, and N. Nakano, Numerical analysis of tunnel oxide passivated contact solar cell performances for dielectric thin film materials and bulk properties. Solar Energy, 2021. 214: p. 205-213.

32. Melskens, J., et al. Concepts and prospects of passivating contacts for crystalline silicon solar cells. in 2015 IEEE 42nd Photovoltaic Specialist Conference (PVSC). 2015. IEEE.

33. Feldmann, F., et al., Studying dopant diffusion from poly-Si passivating contacts. Solar Energy Materials and Solar Cells, 2019. 200: p. 109978.

34. Richter, A., et al., n-Type Si solar cells with passivating electron contact: Identifying sources for efficiency limitations by wafer thickness and resistivity variation. Solar Energy Materials and Solar Cells, 2017. 173: p. 96-105.

35. Haase, F., et al., Laser contact openings for local poly-Si-metal contacts enabling 26.1%-efficient POLO-IBC solar cells. Solar Energy Materials and Solar Cells, 2018. 186: p. 184-193.

36. Chen, Y., et al., Mass production of industrial tunnel oxide passivated contacts (i-TOPCon) silicon solar cells with average efficiency over 23% and modules over 345 W. Progress in Photovoltaics: Research and Applications, 2019. 27(10): p. 827-834.

37. Melskens, J., et al., Passivating contacts for crystalline silicon solar cells: From concepts and materials to prospects. IEEE Journal of Photovoltaics, 2018. 8(2): p. 373-388.

38. Brendel, R. and R. Peibst, Contact selectivity and efficiency in crystalline silicon photovoltaics. IEEE Journal of photovoltaics, 2016. 6(6): p. 1413-1420.

39. Hollemann, C., et al., 26.1%-efficient POLO-IBC cells: Quantification of electrical and optical loss mechanisms. Progress in Photovoltaics: Research and Applications, 2019. 27(11): p. 950-958.

40. Ingenito, A., et al., A passivating contact for silicon solar cells formed during a single firing thermal annealing. Nature Energy, 2018. 3(9): p. 800-808.

41. Reiter, S., et al., Parasitic absorption in polycrystalline Si-layers for carrier-selective front junctions. Energy Procedia, 2016. 92: p. 199-204.

42. Feldmann, F., et al., Passivated rear contacts for high-efficiency n-type Si solar cells providing high interface passivation quality and excellent transport characteristics. Solar energy materials and solar cells, 2014. 120: p. 270-274.

43. Moldovan, A., et al., Tunnel oxide passivated carrier-selective contacts based on ultra-thin SiO2 layers. Solar energy materials and solar cells, 2015. 142: p. 123-127.

44. Čampa, A., et al., Detailed analysis and understanding of the transport mechanism of poly-Si-based carrier selective junctions. IEEE Journal of Photovoltaics, 2019. 9(6): p. 1575-1582.

45. Yan, D., et al., Phosphorus-diffused polysilicon contacts for solar cells. Solar Energy Materials and Solar Cells, 2015. 142: p. 75-82.

46. Stodolny, M.K., et al., Material properties of LPCVD processed n-type polysilicon passivating contacts and its application in PERPoly industrial bifacial solar cells. Energy Procedia, 2017. 124: p. 635-642.

47. Tutsch, L., et al., Improved passivation of n-type poly-Si based passivating contacts by the application of hydrogen-rich transparent conductive oxides. IEEE Journal of Photovoltaics, 2020. 10(4): p. 986-991.

48. Polzin, J.-I., et al. Study on the interfacial oxide in passivating contacts. in AIP Conference Proceedings. 2019. AIP Publishing LLC.

49. Lindekugel, S., et al., Plasma hydrogen passivation for crystalline silicon thin-films. Proceedings of 23rd EU PVSEC, Valencia, 2008: p. 2232-2235.

50. Nogay, G., et al., Interplay of annealing temperature and doping in hole selective rear contacts based on silicon-rich silicon-carbide thin films. Solar Energy Materials and Solar Cells, 2017. 173: p. 18-24.

51. Nemeth, B., et al., Polycrystalline silicon passivated tunneling contacts for high efficiency silicon solar cells. Journal of Materials Research, 2016. 31(6): p. 671-681.

52. Schnabel, M., et al., Hydrogen passivation of poly-Si/SiOx contacts for Si solar cells using Al2O3 studied with deuterium. Applied Physics Letters, 2018. 112(20): p. 203901.

53. Yang, X., et al., High-performance TiO2-based electron-selective contacts for crystalline silicon solar cells. Advanced Materials, 2016. 28(28): p. 5891-5897.

54. Mozaffari, N., et al., Efficient Passivation and Low Resistivity for p+-Si/TiO2 Contact by Atomic Layer Deposition. ACS Applied Energy Materials, 2020. 3(7): p. 6291-6301.

55. Alajlani, Y., et al., Inorganic thin film materials for solar cell applications, in Reference Module in Materials Science and Materials Engineering. 2018, Elsevier BV.

56. "International Technology Roadmap for Photovoltaic Results 2017.". ITRPV, 2018.

57. Blakers, A.W., et al., 22.8% efficient silicon solar cell. Applied Physics Letters, 1989. 55(13): p. 1363-1365.

58. https://pv-manufacturing.org/wafer-sizes/.

59. Chen, Y., et al., From laboratory to production: learning models of efficiency and manufacturing cost of industrial crystalline silicon and thin-film photovoltaic technologies. IEEE Journal of photovoltaics, 2018. 8(6): p. 1531-1538.

60. Wang, Y., et al., Supply of low-cost and high-efficiency multi-GW mono wafers. Photovoltaics International, 2017. 36: p. 38-42.

61.   Gu, X., X. Yu, and D. Yang, Efficiency improvement of crystalline silicon solar cells with a back-surface field produced by boron and aluminum co-doping. Scripta Materialia, 2012. 66(6): p. 394-397.

62.   Prakoso, A.B., F. Ferdiansjah, and F. Faridah, Optimasi Pembentukan Lapisan Boron P+ pada Permukaan Belakang Sel Surya untuk Peningkatan Efisiensi Sel Surya berbasis Wafer Silikon Monokristal. Teknofisika, 2012. 1(1): p. 20-26.

63.   Meemongkolkiat, V., et al., Factors limiting the formation of uniform and thick aluminum–back-surface field and its potential. Journal of the Electrochemical Society, 2005. 153(1): p. G53.

64.   Green, M.A., The passivated emitter and rear cell (PERC): From conception to mass production. Solar Energy Materials and Solar Cells, 2015. 143: p. 190-197.

65.   Schmidt, J., et al., Surface passivation of high-efficiency silicon solar cells by atomic-layer-deposited Al2O3. Progress in photovoltaics: research and applications, 2008. 16(6): p. 461-466.

66.   Dingemans, G., et al., Influence of annealing and Al2O3 properties on the hydrogen-induced passivation of the Si/SiO2 interface. Journal of Applied Physics, 2012. 111(9): p. 093713.

67.   Kersten, F., et al., Role of annealing conditions on surface passivation properties of ALD Al2O3 films. Energy Procedia, 2013. 38: p. 843-848.

68.   Tong, J., et al., Solution-processed molybdenum oxide for hole-selective contacts on crystalline silicon solar cells. Applied surface science, 2017. 423: p. 139-146.

69.   Schmidt, J., M. Kerr, and A. Cuevas, Surface passivation of silicon solar cells using plasma-enhanced chemical-vapour-deposited SiN films and thin thermal SiO2/plasma SiN stacks. Semiconductor science and technology, 2001. 16(3): p. 164.

70.   Chen, R., et al., 23.83% efficient mono-PERC incorporating advanced hydrogenation. Progress in Photovoltaics: Research and Applications, 2020. 28(12): p. 1239-1247.

71.   Zhang, Y., et al., Pathway towards 24% efficiency for fully screen-printed passivated emitter and rear contact solar cells. Journal of Physics D: Applied Physics, 2021. 54(21): p. 214003.

72.   Min, B., et al., A roadmap toward 24% efficient PERC solar cells in industrial mass production. IEEE Journal of Photovoltaics, 2017. 7(6): p. 1541-1550.

73.   Taguchi, M., et al., 24.7% record efficiency HIT solar cell on thin silicon wafer. IEEE Journal of photovoltaics, 2013. 4(1): p. 96-99.

74.   De Wolf, S., et al., High-efficiency silicon heterojunction solar cells: A review. green, 2012. 2(1): p. 7-24.

75.   Fuhs, W., K. Niemann, and J. Stuke. Heterojunctions of amorphous silicon and silicon single crystals. in AIP Conference Proceedings. 1974. American Institute of Physics.

76.   Pankove, J. and M. Tarng, Amorphous silicon as a passivant for crystalline silicon. Applied Physics Letters, 1979. 34(2): p. 156-157.

77.   De Wolf, S., C. Ballif, and M. Kondo, Kinetics of a-Si: H bulk defect and a-Si: H/c-Si interface-state reduction. Physical Review B, 2012. 85(11): p. 113302.

78.   Long, W., et al., On the limiting efficiency for silicon heterojunction solar cells. Solar Energy Materials and Solar Cells, 2021. 231: p. 111291.

79. Herasimenka, S.Y., W.J. Dauksher, and S.G. Bowden, > 750 mV open circuit voltage measured on 50 μ m thick silicon heterojunction solar cell. Applied Physics Letters, 2013. 103(5): p. 053511.

80. Ru, X., et al., 25.11% efficiency silicon heterojunction solar cell with low deposition rate intrinsic amorphous silicon buffer layers. Solar energy materials and solar cells, 2020. 215: p. 110643.

81. Haschke, J., et al., Silicon heterojunction solar cells: Recent technological development and practical aspects-from lab to industry. Solar Energy Materials and Solar Cells, 2018. 187: p. 140-153.

82. Peter Seif, J., et al., Amorphous silicon oxide window layers for high-efficiency silicon heterojunction solar cells. Journal of Applied Physics, 2014. 115(2): p. 024502.

83. Ruan, T., et al., Effect of deposition temperature of a-Si: H layer on the performance of silicon heterojunction solar cell. Journal of Materials Science: Materials in Electronics, 2019. 30(14): p. 13330-13335.

84. Gogolin, R., et al., Silicon heterojunction solar cells: Influence of H2-dilution on cell performance. Solar energy materials and solar cells, 2012. 106: p. 47-50.

85. Mews, M., et al., Hydrogen plasma treatments for passivation of amorphous-crystalline silicon-heterojunctions on surfaces promoting epitaxy. Applied Physics Letters, 2013. 102(12): p. 122106.

86. Schüttauf, J., et al., Comparison of surface passivation of crystalline silicon by a-Si: H with and without atomic hydrogen treatment using hot-wire chemical vapor deposition. Thin Solid Films, 2011. 519(14): p. 4476-4478.

87. Sai, H., et al., Impact of intrinsic amorphous silicon bilayers in silicon heterojunction solar cells. Journal of Applied Physics, 2018. 124(10): p. 103102.

88. Ding, K., et al., Optimized amorphous silicon oxide buffer layers for silicon heterojunction solar cells with microcrystalline silicon oxide contact layers. Journal of Applied Physics, 2013. 113(13): p. 134501.

89. Boccard, M. and Z.C. Holman, Amorphous silicon carbide passivating layers for crystalline-silicon-based heterojunction solar cells. Journal of Applied Physics, 2015. 118(6): p. 065704.

90. Zhang, Y., et al., Significant improvement of passivation performance by two-step preparation of amorphous silicon passivation layers in silicon heterojunction solar cells. Chinese Physics Letters, 2017. 34(3): p. 038101.

91. Adachi, D., J.L. Hernández, and K. Yamamoto, Impact of carrier recombination on fill factor for large area heterojunction crystalline silicon solar cell with 25.1% efficiency. Applied Physics Letters, 2015. 107(23): p. 233506.

92. Yoshikawa, K., et al., Exceeding conversion efficiency of 26% by heterojunction interdigitated back contact solar cell with thin film Si technology. Solar Energy Materials and Solar Cells, 2017. 173: p. 37-42.

93. Yu, B., et al., Selective tunnel oxide passivated contact on the emitter of large-size n-type TOPCon bifacial solar cells. Journal of Alloys and Compounds, 2021. 870: p. 159679.

94. Feldmann, F., et al. A passivated rear contact for high-efficiency n-type silicon solar cells enabling high Vocs and FF> 82%. in 28th European PV solar energy conference and exhibition. 2013.

95. Attafi, D., et al., Effect of a Back-Surface Field and Passivation Layer on a Silicon Schottky Solar Cell. Transactions on Electrical and Electronic Materials, 2020: p. 1-6.

96. Steinkemper, H., et al., Numerical simulation of carrier-selective electron contacts featuring tunnel oxides. IEEE Journal of Photovoltaics, 2015. 5(5): p. 1348-1356.

97. Quan, C., et al., Computational analysis of a high-efficiency tunnel oxide passivated contact (TOPCon) solar cell with a low-work-function electron-selective-collection layer. Solar Energy, 2018. 170: p. 780-787.

98. Glunz, S.W. and F. Feldmann, SiO2 surface passivation layers–a key technology for silicon solar cells. Solar Energy Materials and Solar Cells, 2018. 185: p. 260-269.

99. Benick, J., et al., High efficiency n-type Si solar cells on Al 2 O 3-passivated boron emitters. Applied Physics Letters, 2008. 92(25): p. 253504.

100. Haase, F. and R. Peibst, 26.1% Record Efficiency for P-type Crystalline Si Solar Cells. ISFH, Emmerthal/Hannove, 2018.

101. Chen, D., et al., 24.58% total area efficiency of screen-printed, large area industrial silicon solar cells with the tunnel oxide passivated contacts (i-TOPCon) design. Solar Energy Materials and Solar Cells, 2020. 206: p. 110258.

102. Huang, Y.-Y., et al., Fully screen-printed bifacial large area 22.6% N-type Si solar cell with lightly doped ion-implanted boron emitter and tunnel oxide passivated rear contact. Solar Energy Materials and Solar Cells, 2020. 214: p. 110585.

103. Almrabet, M.M., Electrically active defects in novel Group IV semiconductors. 2006: Sheffield Hallam University (United Kingdom).

104. Hallam, B., et al., Eliminating light-induced degradation in commercial p-type Czochralski silicon solar cells. Applied Sciences, 2018. 8(1): p. 10.

105. Lannoo, M., Point defects in semiconductors I: theoretical aspects. Vol. 22. 2012: Springer Science & Business Media.

106. Hu, S., Diffusion in silicon and germanium, in Atomic Diffusion in Semiconductors. 1973, Springer. p. 217-350.

107. Watkins, G.D., Intrinsic defects in silicon. Materials science in semiconductor processing, 2000. 3(4): p. 227-235.

108. Tisza, M., Physical metallurgy for engineers. 2001: Asm International.

109. Mukherjee, S., Applied mineralogy: applications in industry and environment. 2012: Springer Science & Business Media.

110. De Groot, S. and C. Ten Seldam, On the energy levels of a model of the compressed hydrogen atom. Physica, 1946. 12(9-10): p. 669-682.

111. Sze, S.M., Y. Li, and K.K. Ng, Physics of semiconductor devices. 2021: John wiley & sons.

112. Stöckmann, F., On the classification of traps and recombination centres. physica status solidi (a), 1973. 20(1): p. 217-220.

113. Miller, M., G. Olsen, and M. Ettenberg, The effect of gas-phase stoichiometry on deep levels in vapor-grown GaAs. Applied Physics Letters, 1977. 31(8): p. 538-540.

114. Henry, C. and D.V. Lang, Nonradiative capture and recombination by multiphonon emission in GaAs and GaP. Physical Review B, 1977. 15(2): p. 989.

115. Andersen, O., Electrical properties of hydrogen-related defects in crystalline silicon. 2003.

116. https://repository.up.ac.za/bitstream/handle/2263/26574/02chapters3-4.pdf?sequence=3&isAllowed=y. https://repository.up.ac.za/bitstream/handle/2263/26574/02chapters3-4.pdf?sequence=3&isAllowed=y].

117. Green, M.A., Intrinsic concentration, effective densities of states, and effective mass in silicon. Journal of Applied Physics, 1990. 67(6): p. 2944-2954.

118. Kim, E.K., et al., Effects of leakage current on isothermal capacitance transient spectroscopy signals for midgap levels in GaAs. Journal of applied physics, 1990. 67(3): p. 1380-1383.

119. https://www.iue.tuwien.ac.at/phd/goes/dissse19.html, available in 04.01.2022.

120. Bakos, T., Defects in amorphous SiO2: reactions, dynamics and optical properties. 2003.

121. Ling, S.J., J. Sanny, and W. Moebs, The Quantum Tunneling of Particles through Potential Barriers. University Physics Volume 3, 2016.

122. Belete, M., Fabrication and Characterization of Tunneling Oxides on Graphene. 2013.

123. http://abyss.uoregon.edu/~js/glossary/quantum_tunneling.html, 13.12.2021.

124. (2013), A.U.s.M.D.S.S., Atlas User's Manual DEVICE SIMULATION SOFTWARE. (2013).

125. Gehring, A. and S. Selberherr, Modeling of tunneling current and gate dielectric reliability for nonvolatile memory devices. IEEE Transactions on Device and Materials Reliability, 2004. 4(3): p. 306-319.

126. Miranda, E. and F. Palumbo, Analytic expression for the Fowler–Nordheim V–I characteristic including the series resistance effect. Solid-state electronics, 2011. 61(1): p. 93-95.

127. Price, P.J. and J.M. Radcliffe, Esaki tunneling. IBM Journal of Research and Development, 1959. 3(4): p. 364-371.

128. Gehring, A. and S. Selberherr, Tunneling models for semiconductor device simulation. Handbook of theoretical and computational nanotechnology, 2006. 10: p. 469-543.

129. Fowler, R.H. and L. Nordheim, Electron emission in intense electric fields. Proceedings of the Royal Society of London. Series A, Containing Papers of a Mathematical and Physical Character, 1928. 119(781): p. 173-181.

130. Grado-Caffaro, M. and M. Grado-Caffaro, Fowler–Nordheim electron tunneling under very intense electric field. Optik, 2010. 121(21): p. 2001-2002.

131. Jeon, H., et al., Resistive switching of a TaOx/TaON double layer via ionic control of carrier tunneling. Applied Physics Letters, 2014. 104(15): p. 151603.

132. Pollack, S., Schottky field emission through insulating layers. Journal of Applied Physics, 1963. 34(4): p. 877-880.

133. Ricco, B., G. Gozzi, and M. Lanzoni, Modeling and simulation of stress-induced leakage current in ultrathin SiO/sub 2/films. IEEE Transactions on Electron Devices, 1998. 45(7): p. 1554-1560.

134. Hu, C. Stress-induced current in thin silicon dioxide films. in 1992 International Technical Digest on Electron Devices Meeting. 1992. IEEE.

135. Ganichev, S., et al., Distinction between the Poole-Frenkel and tunneling models of electric-field-stimulated carrier emission from deep levels in semiconductors. Physical Review B, 2000. 61(15): p. 10361.

136. Chiu, F.-C., A review on conduction mechanisms in dielectric films. Advances in Materials Science and Engineering, 2014. 2014.

137. Online resource, Q.M.T., " pp. 1–12. Access date: 2022-01-01, and l.h.w.i.t.a.a.p.e.n.h. 9:00PM.

138. Chou, A.I., et al., Modeling of stress-induced leakage current in ultrathin oxides with the trap-assisted tunneling mechanism. Applied physics letters, 1997. 70(25): p. 3407-3409.

139. Chang, W.J., M.P. Houng, and Y.H. Wang, Simulation of stress-induced leakage current in silicon dioxides: A modified trap-assisted tunneling model considering Gaussian-distributed traps and electron energy loss. Journal of Applied Physics, 2001. 89(11): p. 6285-6293.

140. Chang, W.-J., M.-P. Houng, and Y.-H. Wang, Electrical properties and modeling of ultrathin impurity-doped silicon dioxides. Journal of Applied Physics, 2001. 90(10): p. 5171-5179.

141. Ielmini, D., et al., Modeling of SILC based on electron and hole tunneling. I. Transient effects. IEEE Transactions on Electron Devices, 2000. 47(6): p. 1258-1265.

142. Ielmini, D., et al., Modeling of SILC based on electron and hole tunneling. II. Steady-state. IEEE Transactions on Electron Devices, 2000. 47(6): p. 1266-1272.

143. Schenk, A., Physical models for semiconductor device simulation, in Festkörperprobleme 36. 1997, Springer. p. 245-263.

144. Kløw, F., E.S. Marstein, and S.E. Foss, Tunneling contact passivation simulations using Silvaco Atlas. Energy Procedia, 2015. 77: p. 99-105.

145. Deckers, J., et al., Aluminum oxide-aluminum stacks for contact passivation in silicon solar cells. Energy Procedia, 2014. 55: p. 656-664.

146. Anand, N. and P. Kale, Optimization of TOPCon structured solar cell using AFORS-HET. Transactions on Electrical and Electronic Materials, 2021. 22(2): p. 160-166.

147. Maiti, C.K., Computer aided design of micro-and nanoelectronic devices. 2016: World Scientific.

148. Choe, K.S., Parametric simulation of the back-surface field effect in the silicon solar cell. Solid state sciences, 2014. 29: p. 48-51.

149. Hoex, B., et al., Excellent passivation of highly doped p-type Si surfaces by the negative-charge-dielectric Al 2 O 3. Applied Physics Letters, 2007. 91(11): p. 112107.

150. Richter, A., J. Benick, and M. Hermle, Boron emitter passivation with Al2O3 and Al2O3/SiNx stacks using ALD Al2O3. IEEE Journal of Photovoltaics, 2013. 3(1): p. 236-245.

151. Zielke, D., et al., Contact passivation in silicon solar cells using atomic-layer-deposited aluminum oxide layers. physica status solidi (RRL)–Rapid Research Letters, 2011. 5(8): p. 298-300.

152. Moldovan, A., et al. Tunnel oxide passivated carrier-selective contacts based on ultra-thin SiO2 layers grown by photo-oxidation or wet-chemical oxidation in ozonized water. in 2015 IEEE 42nd Photovoltaic Specialist Conference (PVSC). 2015. IEEE.

153. Zhang, Z., et al., Carrier transport through the ultrathin silicon-oxide layer in tunnel oxide passivated contact (TOPCon) c-Si solar cells. Solar Energy Materials and Solar Cells, 2018. 187: p. 113-122.

154.   Richter, A., et al., Design rules for high-efficiency both-sides-contacted silicon solar cells with balanced charge carrier transport and recombination losses. Nature Energy, 2021. 6(4): p. 429-438.

155.   Rohatgi, A., et al., Fabrication and modeling of high-efficiency front junction n-type silicon solar cells with tunnel oxide passivating back contact. IEEE Journal of Photovoltaics, 2017. 7(5): p. 1236-1243.

156.   Feldmann, F., et al., Efficient carrier-selective p-and n-contacts for Si solar cells. Solar Energy Materials and Solar Cells, 2014. 131: p. 100-104.

157.   Tao, Y., et al. Carrier selective tunnel oxide passivated contact enabling 21.4% efficient large-area N-type silicon solar cells. in 2016 IEEE 43rd Photovoltaic Specialists Conference (PVSC). 2016. IEEE.

158.   Höffler, H., J. Haunschild, and S. Rein, Influence of external contacting on electroluminescence and fill factor measurements. Solar Energy Materials and Solar Cells, 2016. 152: p. 180-186.

159.   Labed, M., et al., Modeling and analyzing temperature-dependent parameters of Ni/β-Ga2O3 Schottky barrier diode deposited by confined magnetic field-based sputtering. Semiconductor Science and Technology, 2021. 36(3): p. 035020.

160.   Bonilla, R.S., et al., Dielectric surface passivation for silicon solar cells: A review. physica status solidi (a), 2017. 214(7): p. 1700293.

161.   https://www.pveducation.org/pvcdrom/solar-cell-operation/open-circuit-voltage. 29.03.2022.

162.   Dueñas, S., et al. The role of defects in solar cells: Control and detection defects in solar cells. in 2013 Spanish Conference on Electron Devices. 2013. IEEE.

163.   Mahajan, S., Defects in semiconductors and their effects on devices. Acta materialia, 2000. 48(1): p. 137-149.

164.   Luque, A. and A. Martí, Increasing the efficiency of ideal solar cells by photon induced transitions at intermediate levels. Physical Review Letters, 1997. 78(26): p. 5014.

165.   Hu, S., et al., Amorphous TiO2 coatings stabilize Si, GaAs, and GaP photoanodes for efficient water oxidation. Science, 2014. 344(6187): p. 1005-1009.

166.   Green, M. and J. Shewchun, Current multiplication in metal-insulator-semiconductor (MIS) tunnel diodes. Solid-State Electronics, 1974. 17(4): p. 349-365.

167.   Shewchun, J., D. Burk, and M.B. Spitzer, MIS and SIS solar cells. IEEE Transactions on Electron Devices, 1980. 27(4): p. 705-716.

168.   Nemeth, B., et al. Low temperature Si/SiO x/pc-Si passivated contacts to n-type Si solar cells. in 2014 IEEE 40th Photovoltaic Specialist Conference (PVSC). 2014. IEEE.

169.   Römer, U., et al., Recombination behavior and contact resistance of n+ and p+ poly-crystalline Si/mono-crystalline Si junctions. Solar Energy Materials and Solar Cells, 2014. 131: p. 85-91.

170.   Rienäcker, M., et al., Junction resistivity of carrier-selective polysilicon on oxide junctions and its impact on solar cell performance. IEEE Journal of Photovoltaics, 2016. 7(1): p. 11-18.

171.   Gupta, H. and R. Van Overstraeten, Role of trap states in the insulator region for MIM characteristics. Journal of Applied Physics, 1975. 46(6): p. 2675-2682.

172. Houssa, M., et al., Trap-assisted tunneling in high permittivity gate dielectric stacks. Journal of Applied Physics, 2000. 87(12): p. 8615-8620.

173. Kar, S., High permittivity gate dielectric materials. Vol. 43. 2013: Springer.

174. Böer, K.W. and U.W. Pohl, Semiconductor physics. 2018: Springer.

175. Han, D., et al., Impurity doping in SiO 2: Formation energies and defect levels from first-principles calculations. Physical Review B, 2010. 82(15): p. 155132.

176. McCluskey, M.D. and E.E. Haller, Dopants and defects in semiconductors. 2018: CRC press.

177. Dannefaer, S., T. Bretagnon, and D. Kerr, Vacancy-type defects in crystalline and amorphous SiO2. Journal of applied physics, 1993. 74(2): p. 884-890.

178. Griscom, D.L., G. Pacchioni, and L. Skuja, Defects in SiO2 and related dielectrics: science and technology. 2000: Kluwer Academic Publishers.

179. Palma, A., F. Gámiz, and S. Selberherr, Modeling of retention time degradation due to inelastic trap-assisted tunneling in EEPROM devices A. Gehring", F. Jiménez-Molinos, H. Kosina. Microelectronics Reliability, 2003. 43: p. 1495-1500.

180. Palma, A., J. López-Villanueva, and J. Carceller, Electric field dependence of the electron capture cross section of neutral traps in SiO2. Journal of the Electrochemical Society, 1996. 143(8): p. 2687.

181. Denison, D., J. Barbour, and J. Burkhart, Low dielectric constant, fluorine-doped SiO2 for intermetal dielectric. Journal of Vacuum Science & Technology A: Vacuum, Surfaces, and Films, 1996. 14(3): p. 1124-1126.

182. Mordo, D., et al., Characterization of PECVD Deposited Fluorosilicate Glass (FSG) After CMP and Cleaning. MRS Online Proceedings Library Archive, 1996. 443.

183. Reichel, C., et al., Tunnel oxide passivated contacts formed by ion implantation for applications in silicon solar cells. Journal of Applied Physics, 2015. 118(20): p. 205701.

184. Miikkulainen, V., et al., Crystallinity of inorganic films grown by atomic layer deposition: Overview and general trends. Journal of Applied Physics, 2013. 113(2): p. 2.

Publications and conferences

D.Attafi, R. Boumaraf, A. Meftah, N.Sengouga. Effect of a Back-Surface Field and Passivation Layer on a Silicon Schottky Solar Cell. Transactions on Electrical and Electronic Materials. 2020. doi.org/10.1007/s42341-020-00246-4

D.Attafi, A. Meftah, R. Boumaraf, M. Labed, N.Sengouga. Enhancement of silicon solar cell performance by introducing selected defects in the SiO_2 passivation layer. Optik. 2021. doi.org/10.1016/j.ijleo.2020.166206

- 'Effect of passivation layer on silicon solar cell performance', the first international conference on Materials, Energy and Environment (MEE'2020).
- 'Optimization of Topcon Structured Solar Cell Using SILVACO TCAD'. 1st International Conference on Sustainable Energy and Advanced Materials IC-SEAM'21 April 21-22, 2021.
- 'Enhancement of silicon solar cell performance by introducing selected defects in the SiO_2 passivation layer', 8th international conference on materials science and nanotechnology for next generation held in Elazig, Turkey. 2021.

REGULAR PAPER

Effect of a Back-Surface Field and Passivation Layer on a Silicon Schottky Solar Cell

Djemaa Attafi[1] · Rami Boumaraf[1] · Amjad Meftah[1] · Nouredine Sengouga[1]

Abstract

In this work, a numerical simulation of a silicon based solar cell (SC) is carried out using Silvaco-Atlas software. The back contact and the back surface field (BSF) combined with a passivation layer (PL) realized by using SiO_2 tunneling layer, is addressed in this paper. It is demonstrated that a proper choice of the BSF and PL can enhance a Schottky back contact based solar cell compared to its ohmic counterpart. BSF has to be properly doped to reduce the barrier of the Schottky contact. The tunnel oxide is a vital part in this solar cell. It is required to achieve excellent interface passivation and has to have an optimum thickness and below this thickness, the SC performance is enhanced by a tunneling effect, while it is deteriorated by the fill factor reduction above this optimum thickness.

Keywords Passivation · Back surface field · Tunneling effect · Numerical simulation

1 Introduction

There are number of different semiconductor materials that are suitable for the conversion of photons energy into electrical energy; each of them has advantages and drawbacks. Among all materials, silicon is the most commonly used in solar cells manufacturing because it is very abundant on earth, nontoxic and it has an almost ideal band gap for photovoltaic solar energy conversion. For silicon-based solar cells, the theoretical limit conversion efficiency is $\approx 30\%$, in laboratory it is close to 25% while the commercial cells do not exceed 20% [1, 2]. n-type silicon based solar devices tend to have an excellent long-term stability of power conversion compared to their p-type counter parts [3, 4] because of better minority carrier lifetime [5]. Furthermore; these n-type Si solar are more tolerant to common transition metal doping impurities [6] and free of light induced degradation (LID) [7]. Recently, the passivation of solar cells surfaces became an additional step to improve their efficiency [8–10]. It used in photovoltaic cells in order to limit the defects created at the different stages of the cell manufacturing process, and to obtain high conversion efficiencies [11, 12]. In addition

to passivation contact, polysilicon is used as a rear contact in solar cells, which provide a back field effect passivation with the chemical passivation of Si by SiO_x, and eliminates the interface states on the tunneling layer/polysilicon interfaces that also may be accessible by tunneling recombination through the tunneling oxide [13, 14]. On the other hand, the use of Schottky barrier solar cells proves to be cost-effective and industrially scalable [15] and its efficiencies can approach that of conventional p–n junction solar cells. This paper addresses a detailed numerical simulation of a silicon solar cell to understand the back contact type, BSF and PL influences on the n-type Si solar cell performance. The study is carried out by numerical simulation using SIL-VACO-ATLAS software as a powerful tool to study many electronic devises [16]. It will be seen that a right choice of the back-surface field and the passivation layers based solar cell can exceed that of the traditional p–n junction.

2 Materials and Methods

2.1 Device Structure

The simulated solar cell structure in this work is illustrated in Fig. 1. It is two-dimensional p–n simple junction device. The emitter is made of p-type monocrystalline (mc) silicon while the base a phosphorous-doped monocrystalline silicon, and

---

✉ Nouredine Sengouga
  n.sengouga@univ-biskra.dz

[1] LMSM, Mohammed Khider University, 07000 Biskra, Algeria

 Springer

127

Enhancement of silicon solar cell performance by introducing selected defects in the SiO_2 passivation layer

Djemaa Attafi, Amjad Meftah, Rami Boumaraf, Madani Labed,
Nouredine Sengouga *

LMSM, Mohammed Khider University, 07000, Biskra, Algeria

ABSTRACT

Deep level defects usually have harmful effect on solar cells. In this work it is shown; however, that correct incorporation of selected defects in the silicon oxide region of a silicon solar cell improves its efficiency. This is demonstrated by numerical simulation of n-type silicon-based solar cell including deep level defects in the silicon dioxide (SiO_2) passivation layer. The defect density was varied to study its effect on the solar cell performance. The selected defects assist the majority carrier's transport through their energy levels that are echoing with the band edge state, and repulse the minority carrier, therefore reducing recombination. It was found that well-defined deep defect density and a minimum thickness of the SiO_2 passivation layer are required for high efficiency Si-based solar cells. The defects must be of a high density ($\sim 10^{17} cm^{-3}$), and energetically situated above the conduction band minimum (CBM) of the adjacent Si layer. With these considerations, the conversion efficiency attained 26 %. Furthermore, in the case of very thin passivation layer, the current through defects did not have any effect on the solar cell performance since the tunneling current goes directly through this tin layer.

1. Introduction

The performance of commercial solar cells is strongly dominated by defects and impurities. Defects create deep energy levels in the semiconductor band gap and usually have undesired effects such as degrading the carrier lifetime and quantum efficiency of solar cells [1,2]. Although shallow level defects are often used to introduce charge carriers into semiconductors by doping, deep level defects are frequently found to be harmful in optoelectronic devices, such as solar cells, mainly because they could recombine charge carriers and then diminishing the device efficiency [3].

Defects on the front and back surface of silicon (Si)–based solar cell can be passivated by depositing an additional layer of silicon oxide (SiO_x) or silicon nitride (SiN$_x$) [4,5]. Therefore, tunneling contact passivation using Al_2O_3 [6,7] and SiO_2 [8] is considered as one of the best solutions to give high efficiencies of Si-based solar cells [9–11]. Thus, it was shown that the tunnel oxide is a vital element of this contact [12], where it reduces minority carriers' recombination and simultaneously not hamper majority carriers' flow [4,13]. This process occurs since a potential barrier is formed in the valence and conduction bands of the Si semiconductor. This barrier prevents the passage of minority carriers while majority carriers pass through the tunneling effect. Thus, it increases the majority carrier concentration near the contact, and decreases minority concentration, therefore decreases the recombination rate [14].

---

* Corresponding author.
E-mail address: n.sengouga@univ-biskra.dz (N. Sengouga).

128

People's Democratic Republic of Algeria

Ministry of Higher Education and Scientific Research

University of Echahid Hamma Lakhdar, El-Oued

Faculty of Exact Sciences

The First International Conference on Materials, Energy & Environment (MEE'2020)

CERTIFICATE OF PARTICIPATION

This Certifies That

Attafi Djemaa

Presented a poster communication at the first international conference on Materials, Energy & Environment (MEE'2020), organized from January 20-21, 2020 at the University of Echahid Hamma Lakhdar, El-Oued, entitled:

"Effect of passivation layer on the silicon solar cell performance"

Co-author (s): Amjad Meftah, Rami Boumaraf, Noureddine Sengouga

Chairman of MEE'2020

Dr. Mohammed El-Hadi ATTIA

MSNG-2021
MATERIALS SCIENCE AND NANOTECHNOLOGY
FOR NEXT GENERATION

CERTIFICATE
OF ATTENDANCE

This is to certify that

Djemaa ATTAFİ

Has attended
8th international conference on materials science and nanotechnology
for next generation held in Elazığ, Turkey.
14-16 July 2021

Prof. Dr. Fahrettin YAKUPHANOĞLU

****

N° : TAM408/2021   **1st International Conference on Sustainable Energy and Advanced Materials**
IC-SEAM'21 April 21-22, 2021, Ouargla, ALGERIA (Virtual conference)

****

CERTIFICATE OF PARTICIPATION

The organizing committee of the first International Conference on Sustainable Energy and Advanced Materials
IC-SEAM'21 April 21-22, 2021, Ouargla, ALGERIA, certifies that:

Djemaa attafi

presented an Oral communication entitled:

Optimization of TOPCon Structured Solar Cell Using SILVACO TCAD

Co-author (s):   Amjad meftah

Dean of the Faculty   Coordinator of IC-SEAM'21   Chairman of the IC-SEAM'21
Pr. Djamel BECHKI   Dr. Eazhar BENMEBROUK   Dr. Eazhar MOHAMMEDI

131